PAVEMENT SAFETY EVALUATION WITH 1MM 3D LASER TEXTURE DATA

By

LIN LI

Bachelor of Science in Transportation Engineering
China Agriculture University (CAU)
Beijing, China
2006

Master of Science in Logistics Engineering
University of Science and Technology Beijing (USTB)
Beijing, China
2009

Submitted to the Faculty of the
Oklahoma State University
Graduate College of the
in partial fulfillment of
the requirements for
the Degree of
DOCTOR OF PHILOSOPHY
July, 2015

PAVEMENT SAFETY EVALUATION WITH 1MM 3D LASER TEXTURE DATA

Dissertation Approved:

Dissertation Advisor: Dr. Kelvin C. P. Wang

Committee member: Dr. Stephen Alan Cross

Committee member: Dr. Qiang Li

Outside Committee member: Dr. Guoliang Fan

ACKNOWLEDGEMENTS

I am very grateful to Dr. Kelvin C. P. Wang, my advisor, for his valuable advice and guidance in helping me complete this dissertation. Dr. Wang's rigorous and precise academic attitude sets a great model for the author to follow. In addition, I would like to express my deep gratitude to Dr Wang for his patience and assistance during my tough times. Without his generosity, I would not have accomplished this degree. The author would also like to thank Dr. Wang's wife, Lily Liu, for her assistance and advice on our daily lives.

Special thanks go to Dr. Stephen A. Cross, who is one of my academic committee members, for his wonderful teaching in the classroom and constructive advice on my dissertation. The author expresses his deep gratitude and respect to Dr. Guoliang Fan, not only for his valuable comments on my dissertation but also for his assistance during difficult times in Stillwater, OK. The author would like to give his sincere appreciation to Dr. Qiang Li as well for his kindness and academic guidance.

Many thanks also go to Dr. Cheng Chen, Dr. Vu Nguyen, Mrs. Wenting Luo, Mr. Justin Thweatt, Mr Guangwei Yang, Mr. Aonan Zhang, Mr. Yang Liu, Mr. Yue Fei, and Mrs. Ran Ji for their sincere assistance and wonderful collaboration. The valuable friendships were developed in the past years in the same research group under Dr. Wang.

Special thanks are also given to the author's parents and parents-in-law, Conghua Li, Min Guo, Jinxiang Luo, and Yougen Peng for their selfless dedication to me and my family. During the degree-seeking years, they took turns to serve or care for our family. I am so grateful that I also learned a lot on how to be a farther from my farther and farther-in-law.

Last but not least, the author thanks his wife Wenting Luo for her willingness to hold my hand along the years, to share joy and tears on the way, to support the family both morally and materially, and to give births to two adorable kids. The author is very proud of having such a helpful, understandable, and obedient daughter Jessie Li. The author also would like to give thanks to the Lord and give us a healthy and lovely son Ethan Li.

Name: LIN LI

Date of Degree: JULY, 2015

Title of Study: PAVEMENT SAFETY EVALUATION WITH 1MM 3D LASER TEXTURE DATA

Major Field: CIVIL ENGINEERING

ABSTRACT:
Pavement safety is highly associated with surface texture characteristics. Measurements of surface texture can be conducted in either stationary or high-speed way. Texture data collected from the existing systems are restricted on either a small portion on pavement surface or one line-of-sight profile, which are unsuitable for network-level pavement survey and incapable of representing the property of entire pavement surface. With the emerging 3D laser imaging technology, Digital Highway Data Vehicle (DHDV) with PaveVision3D Ultra has been evolved into the sophisticated system to conduct full lane data collection on roadways at highway speed up to 60mph (about 100 km/h) at true 1mm resolution.

Several texture indicators have been used to characterize pavement texture such as Mean Profile Depth (MPD). However, some limitations exist on the texture indicators since they only reveal partial aspects of texture property, and are incapable of reflecting other texture properties such as predominant texture direction. In this study a series of texture indicators would be employed to characterize surface texture. Results indicate pavement safety can be estimated with the amplitude, spacing, and functional parameters.

Past studies indicate that pavement friction is not only related to surface texture, but also associated with tire properties and their interactions. However, developing a reliable model for pavement friction prediction is still a challenge for researches. This paper uses Heinrich/Klüppel model to estimate rubber friction on AC pavements. Findings indicate that rubber friction theory is a promising alternative for traditional friction measurement methods.

Pavement grooving is broadly used to reduce skid resistance-related crashes on wet pavements. Past studies indicate groove dimensions can be measured with the profiling data; however, most of the existing profiling instruments only collect one line-of-sight profile, resulting in different groove measurement results when profiles are measured at different lateral locations. In this paper the proposed filters and algorithms are dedicated to identify roadway grooves using 3D texture data. Results indicate the new methodology is robust in automated groove measurement and evaluation.

In summary, this study covers the analysis of 3D pavement data at 1mm resolution with full-lane coverage for data pre-processing and preparation, pavement friction prediction using either texture indicators or rubber friction theory, and automated groove dimension measurement and evaluation.

TABLE OF CONTENTS

Chapter Page

LIST OF TABLES

Table Page

LIST OF FIGURES

Figure Page

CHAPTER 1. INTRODUCTION

1.1 Pavement Texture and Friction

1.1.1 Study Background

The primary concern of pavement engineers is to produce safe, comfortable, and quiet pavements for driving public. However, pavement surface texture would be deteriorated over time due to effects of traffic loading, temperature, and other environmental factors (Ergun, 2005), which causes a series of safety and roughness issues. To ensure pavement surface texture performance to meet the minimum safety and roughness requirement, a prompt and accurate measurement and evaluation of pavement surface texture properties is necessary. Existing texture measurement methods rely on spot laser based systems which only produce line-of-sight data on pavements, and therefore in this study a new texture measurement system would be presented to collect the entire pavement surface data at 1mm resolution at highway speed and in 3D.

Digital Highway Data Vehicle (DHDV), developed by the WayLink Systems Corporation with collaborations from the University of Arkansas and the Oklahoma State University, has been evolved into the sophisticated system to conduct full lane data collection on roadways at highway speed up to 60mph (about 100 km/h). With the latest PaveVision3D Ultra (3D Ultra in short), the resolution of surface texture data in vertical direction is about 0.3 mm and in the longitudinal direction is approximately 1 mm at 60MPH data collection speed. Figure 1.1a shows the exterior appearance of the DHDV equipped with the 3D Ultra technology. The camera and laser working principle is shown in Figure 1.1b.

Figure 1.1 (a) DHDV exterior appearance; (b) Pavevision3D working principle

The 1mm 3D texture data collected from 3D Ultra has versatile applications in pavement engineering, such as cracking recognition, rutting measurement, longitudinal and transverse profiling, faulting measurement, roughness analysis, safety analysis, virtual pavement surface reconstruction, and many others. In this dissertation the application of surface texture on pavement safety evaluation is investigated from the following three aspects: estimation of pavement safety with calculated surface texture

indicators, predication of pavement friction with rubber friction theory on AC pavements, and evaluation of groove performance on rigid pavements.

1.1.2 Surface Texture

Pavement surface texture is defined as the deviation of the pavement surface from a true planar surface or an ideal shape (ASTM E867). These deviations occur at several distinct levels of scale, each defined by wavelength (λ) and peak to peak amplitude (A) of its components. Per the texture definition from Permanent International Association of Road Congresses (PIARC), pavement surface texture can be divided into four categories (ISO 1998; Hall et al, 2009).

- ✓ Micro-texture (λ < 0.02 in [0.5 mm], A = 0.04 to 20 mils [1 to 500 μm]) — Surface roughness quality defined at the microscopic level. It depends on surface properties of the aggregate particles contained in the asphalt or concrete paving material.
- ✓ Macro-texture (λ = 0.02 to 2 in [0.5 to 50 mm], A = 0.005 to 0.8 in [0.1 to 20 mm]) — Surface roughness quality defined by the mixture properties for AC (shape, size, and gradation of aggregate) and the finishing/texturing techniques for PCC (dragging, tinning, grooving; depth, width, spacing and orientation of channels/grooves).
- ✓ Mega-texture (λ = 2 to 20 in [50 to 500 mm], A = 0.005 to 2 in [0.1 to 50 mm]) — Texture wavelengths ranged from 50 mm to 500 mm.
- ✓ Roughness or unevenness (λ>20 in (500 mm)) — Wavelengths longer than the upper limit of mega-texture are defined as roughness or unevenness.

It is widely recognized that pavement surface texture affects many different pavement–tire interactions (PIARC, 1987; Sandberg, 1998). Figure 1.2 shows the impacts

of different texture types on vehicle–road interactions, in which wet pavement friction, interior and exterior noise, splash and spray are mainly dependent on macro-texture properties, while dry pavement friction and tire wear are highly associated with micro-texture characteristics. Other tire-pavement interactions e.g. rolling resistance and ride quality are affected by the mega-texture and roughness.

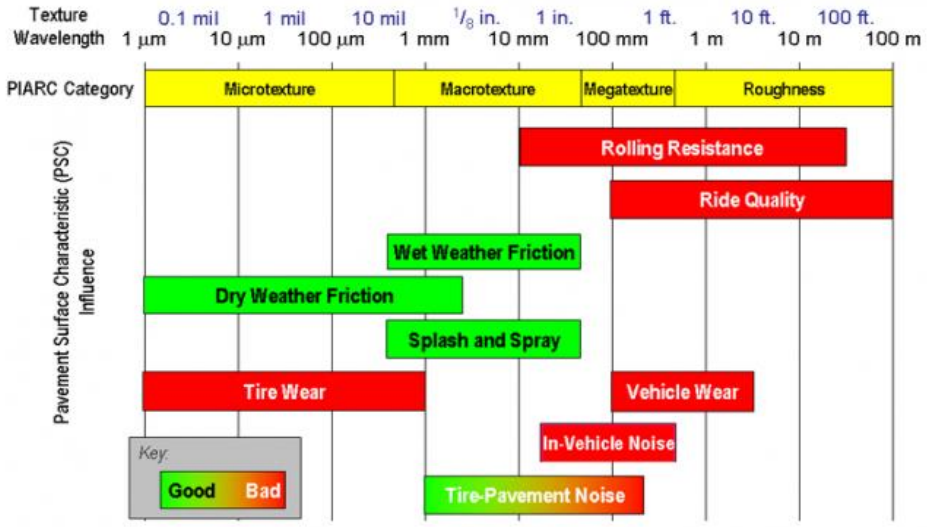

Figure 1.2 The influence of texture wavelength on pavement–tire interactions (PIARC, 1987; Sandberg, 1998)

Therefore the study on macro-texture property places a vital role in interpreting pavement safety performance. Texture indicators characterized from pavement surface can be used to estimate pavement safety property; texture roughness descriptors derived from fractal analysis can be served as basis to predict friction on AC pavements; groove dimensions calculated with the new methodology can be used to evaluate the frictional properties on grooving pavements.

1.1.3 Pavement Friction or Skid Resistance

Pavement friction is a measure of the force generated when a tire slides on a pavement surface, and is dependent on a large number of factors including road types, vehicle tires, vehicle suspension system, traveling speed, ambient temperature, and the presence of contaminants such as oil and water (Hall et al, 2009). Skid resistance is the contribution of roadway surface texture to form or develop this friction, and its value is determined by the interaction between pavement surface and vehicle tires.

The measurement of skid resistance is critical for monitoring pavement safety performance and preventing accidents on wet roadways. Generally different data collection devices produce different frictional indices. For instance, pavement friction measured from skid trailer is recorded as a friction number (FN) or skid number (SN) (ASTM E 274; Kuennen, 2003; Henry, 2000; Janoo et al, 1999); pavement friction measured from British Pendulum Tester (BPT) is recorded as BPN (ASTM E 303). Generally speaking, frictional measurement devices are relatively complex and costly, which are unsuitable for network level pavement friction measurement, so the estimation of skid resistance is becoming increasingly important.

Pioneering efforts have been made to predict pavement friction from texture measurements using experimental methods (Leu et al, 1978; Do et al, 2004; Ergu et al, 2005; Kebrle et al, 2007) with limited successes. Therefore developing a more reliable model for pavement friction prediction is an unsolved issue for researchers. Typically the development of predicative models depends on many factors such as tire inflation

pressure, temperature, rubber wear or aging, sliding velocity, vertical load, pavement texture property, and even road evenness and curviness.

1.1.4 Groove Configuration

Since the early 1960s, grooved pavements have been increasingly used on airfield pavements to increase runway frictional properties during wet weather (FAA, 1997; Horne et al, 1969; Wong, 1990; Ong et al, 2008). The principal purpose of runway grooves is to eliminate the potential hydroplaning risks by providing a path for water to evacuate from under the tire of an airplane as rapidly as possible (Patterson, 2012). Studies indicate the groove configuration dimensions are highly associated with the airplane landing and take-off safety (Ong et al, 2006a; Ong et al, 2006b; Ong et al, 2006c; Wong, 1990). However, it has been proven that groove dimensions deteriorate over time from the repeated interaction with the traffic loading. Accordingly the periodic measurement and assessment of pavement groove dimension such as groove width, depth, and spacing becomes an indispensable tool for pavement safety study.

1.2 Problem Statements

Currently surface texture data acquisition methodologies can be grouped into two categories: static and dynamic approaches. The static methods mainly contain Sand Patch Method (SPM), Outflow Time Method (OFT), and Circular Track Meter (CTM), and other newly developed apparatus i.e. LS 40 Surface Analyzer. As a rule of thumb, texture indicators measured from these instruments can be used as the ground truth or reference values. However, the static measurement methods are time consuming, labor intensive,

and present potential safety hazard to operators and traveling public; therefore they are not commonly used for project- and network-level pavement surveys.

With the advancement of laser and computer techniques, systems to acquire surface macro-texture data at traveling speeds have been developed, such as inertial high speed profiler (McGhee et al, 2003). However, the majority of high-speed measurements are only able to collect one line-of-sight profile along the traveled direction, which cannot represent actual texture properties of the entire lane, especially for irregular pavement surface. In this study the newly developed data collection system (3D Ultra) is applied to conduct full lane data collection on roadways at highway speeds up to 60 mph.

During data collection with 3D Ultra, unexpected noises may be produced due to the presence of non-uniformity of laser intensity, lens distortion, physical installation locations of cameras, vehicle suspension system, traveling speed, as well as pavement surface debris. Therefore signal or image processing methods are used to suppress the impacts of these noises on the subsequent application of 3D texture data.

For currently used texture indicators, MPD is broadly used. MTD can be measured using SPM, and also enables to be converted from the MPD based on the standardized equation from ASTM E 1845. Power Spectral Density (PSD) is only restricted to theoretical research since few researches relate PSD with pavement safety and roughness (Gendy et al, 2007). Root Mean Square (RMS) is used as an indicator to represent the amplitude distribution of profile elevations (McGhee et al, 2003; Prowell et al, 2005). In summary, the existing texture indicators (primarily MPD and MTD) are still inadequate to reveal overall texture properties of pavement surface since there are still other texture

features not used for pavements, such as predominant texture direction and functional parameters associated with pavement drainage and wearing. In this study several parameters would be first used in the pavement engineering field to characterize pavement texture properties in such a way that they correlate with surface topography geometry and functional behaviors, based on which the pavement friction can be estimated.

In addition, several mathematical models have been established to relate surface texture properties with pavement friction. Although they were developed under the different scenarios using the different texture indicators (i.e. MPD) as the inputs of the models and different frictional indices (i.e. DFT and SN) as the outputs of the models, they all indicate pavement friction can be estimated using appropriate texture indicators. However, the pavement friction is not only related to surface texture properties, but also associated with tire properties and their interactions. In this study one rubber friction theory by Heinrich/Klüppel is applied for pavement friction estimation.

Pavement grooving techniques are increasingly used to improve surface skid resistance performance during wet weather. Traditionally point laser range based profiling equipment is used to measure pavement grooving dimensions over time. However, these laser profiling instruments only collect one line-of-sight profile, which cannot reflect the entire lane groove properties due to the limited quantity of profiles that can be analyzed. In addition, the point laser based profiling system is incapable of measuring pavement longitudinal grooves. Past studies also indicated the lack of robust

algorithms to automatically recognize grooves from line-of-sight profile data. In this study, a new methodology would be proposed to overcome these limitations.

1.3 Objectives

The primary objectives of this dissertation include: 1) to preprocess the collected 3D texture with signal or image processing techniques; 2) to use a collection of parameters to characterize surface texture so that surface safety property can be estimated by these texture indicators; 3) to predict pavement frictional properties based on rubber friction theory by Heinrich/Klüppel model; and 4) to automatically identify grooves, calculate groove dimensions and evaluate groove performance. The detailed tasks of this dissertation are elaborated as follow:

- ✓ Extract pixel data from 3D raw images, and calibrate elevation data to ensure there is a smooth transition for the data transversely and longitudinally.
- ✓ Repair the invalid readings and remove outliers using matrix- based data repair approaches. In addition, the repeatability of PaveVision3D Ultra system is validated as well.
- ✓ Sample the calibrated data to any size (e.g. length, width, and spacing), and subsequently take each sample as the basic element for the data processing and analyses.
- ✓ Eliminate the unwanted wavelengths and noises of texture data via filtering techniques, including spatial filters (i.e. mask filter), frequency filters (i.e. Butterworth band filter), and statistical approach (i.e. linear regression).

- ✓ Utilize a series of surface texture indictors to reveal various texture properties, such as spatial parameters, spacing parameters, functional parameters, and hybrid parameters. The correlations among different texture indicators are investigated. As a result, one mathematical model is developed to estimate pavement friction based on amplitude, spacing, and functional parameters.
- ✓ Use rubber friction theory by Heinrich/Klüppel to predict pavement friction on AC pavements based on the 3D texture data, and the comparisons between predicted and measured friction values are made.
- ✓ Automatically identify groove locations, measure groove dimension, separate out the joints from grooves, and assess their performance. In this study three filters and three detection algorithms are proposed to identify grooves. In addition, groove volume based evaluation approach is also proposed to assess groove frictional performance.

CHAPTER 2. LITERATURE REVIEW

This chapter primarily summarizes past studies on pavement texture and friction, the relationships between pavement texture and friction, rubber friction theory, as well as groove dimension measurement and evaluation.

2.1 Pavement Surface Texture

This section mainly involves in texture measurement systems, factors influencing surface texture, existing pavement texture characterization techniques, and the relationships between different texture indicators.

2.1.1 Texture Measurement Systems

The accurate and rapid measurement of pavement texture properties has been of the primary concern for pavement engineers in the past decades and until now (Hall et al, 2009). Various instruments have been developed and used to measure texture property,

and their difference (in terms of the working principle, the repeatability and accuracy levels, data resolution, data acquisition rate, and the way measurement data are processed and reported) can be significant (ASTM E965; ASTM E2157; ASTM E2380; Flintsch et al 2003; McGhee et al 2003; Hall et al; 2009). Generally methods for pavement surface texture measurement can be grouped into two categories: static test method and high-speed test method.

The static measuring method requires lane closures. The commonly used instruments include Sand Patch Method (SPM) (ASTM E 965), Outflow Meter (OFM) (ASTM E 2380), and Circular Texture Meter (CTM) (ASTM E 2157).

- The SPM is a volumetric-based test method that assesses pavement surface macro-texture through spreading a known volume of glass beads in a circle onto a cleaned surface and measuring the diameter of the resulting circle. The volume divided by the area of the circle is reported as the MTD.
- The OFM is a volumetric test method that measures the water drainage rate through surface texture and interior voids. It indicates the hydroplaning potential of a surface by relating to the escape time of water beneath a moving tire. The measurement parameter, outflow time (OFT), defines the macro-texture; high OFTs indicating smooth macro-texture and low OFTs rough macro-texture.
- The CTM is a non-contact laser device that measures surface profile along an 11.25-in (286-mm) diameter circular path of pavement surface at intervals of 0.034 in (0.868 mm). Two different macro-texture indices can be computed from these profiles: MPD and RMS.

High-speed test methods are typically based on non-contact surface profiling techniques as described in ASTM E1845. An automated measurement system provides a large quantity of valuable and inexpensive texture data, while greatly reduces the safety and traffic control problems inherent in the manually performed volumetric methods.

2.1.2 Factors Affecting Surface Texture

Surface texture properties are dependent on various factors, summarized in Table 2.1 (Hall et al, 2009; Williams, 2008).

Table 2.1 Factors Affecting Micro-texture and Macro-texture

Surface Type	**Factor**	**Factor Properties**	**Micro texture**	**Macro texture**
Asphalt	Max. Aggregate Dimension	The size of the largest aggregates; related to the dominant macro texture wavelength		×
	Coarse Aggregate	The control of the stone material, its angularity, its shape, and its durability	×	×
	Fine Aggregate	The angularity and the durability		×
	Bind viscosity and Content	Easy to cause bleeding; bleeding results in the loss of pavement micro and macro texture		×
	Mix Gradation	Gradation of mix		×
	Mix Air Voids	Increased air content improve friction by increasing water drainage		×
Concrete	Coarse Aggregate	See above	×	×
	Fine Aggregate	See above	×	
	Mix Gradation	See above		×
	Texture dimension and orientation	The depth, width, and spacing; texturing direction relative to traffic direction		×
	Texture Skew	Positive Skew results from the majority of peaks of the profile; Negative skew results from the majority of valleys of the profile		×

Note that factors affecting AC surface texture mainly contain the aggregate, binder, and mix properties of the surface material, while factors affecting PCC also contain any texturing techniques done to the material after placement in addition to the aggregate and mix properties. Generally the desired pavement surface property can be designed and constructed by optimizing these affecting factors.

2.1.3 Surface Texture Indicators

Texture indicator is defined as an index or parameter to represent attributes of pavement surface texture, such as the MPD is used to reveal amplitude information of surface texture. Different pavement texture properties have different influences on road-vehicle interactions. For instance, surface transverse groove is constructed to reduce the skid resistance-related traffic crashes; surface longitudinal grooves is used to reduce road-tire noise levels and enhance the lateral stability of vehicles. Therefore, the study on surface texture characterization plays a vital role in interpreting pavement safety.

Currently several texture indicators have been used to characterize pavement surface texture. The MPD is the commonly used one, and can be measured by both the circular track meter (ASTM E 2157) and the other laser based measuring systems (ASTM E 1845). The other standardized index is MTD which is measured using SPM (ASTM E 965). It should be noted that MPD and MTD are two standardized indices for pavement texture characterization.

RMS is measured by several data collection systems, and it can be used as an indicator to represent the amplitude distribution of profile elevations (McGhee et al, 2003; Prowell et al, 2005). In addition, some other texture indicators such as Hessian

Model (Alvarez et al, 1994), Power Spectral Density (PSD) (Gendy et al, 2007), and Fractal Dimension (FD) (Kokkalis et al, 1998) are also explored to characterize pavement surface texture. These parameters only disclose partial aspects of surface texture properties. For instance, PSD is used to describe the energy distribution along wave numbers or wavelengths, and FD is used to describe the complexity of profile or surface texture from distinct observation scale levels.

2.1.4 Relationships among Different Texture Indicators

The study on the relationships between different texture indicators can be grouped into two categories based on texture measurement systems. The first category covers the relationships of texture indicators from static measurement systems; and the second category summarizes the relationships of texture indicators from both static and dynamic measurement systems.

2.1.4.1 Relationships from Stationary Test Systems

Much work has been done to investigate the relationships between MPD and MTD in past researches. Findings indicated that there exist excellent correlations between MPD (collected using CTM) and MTD (collected using SPM) for major pavement surface types except the Open-graded Friction Courses (OGFC) (Abe et al, 2001; Flintsch et al, 2003; Flintsch et al, 2005; Prowell et al, 2005).

In Abe's study, various surface types were chosen to examine the relationships between MPD (collected using CTM) and MTD (collected by SMP). Results indicated there was a good linear relationship between MPD and MTD, as described by the Equation (2.1):

$$MTD = 1.03 \times MPD + 0.15 \qquad R^2 = 0.88 \qquad (2.1)$$

where MTD and MPD are in millimeters

Prowell's study was conducted on 46 different flexible pavement sections at the National Center for Asphalt Technology (NCAT) in Auburn, Alabama (Prowell et al, 2005). These test sites have different nominal aggregate sizes, gradations, and wearing levels. The correlation result with an R-squared value of 0.95, excluding outliers caused by OGFC, was observed. Findings indicated a strong relationship between the MPD and the MTD exists.

2.1.4.2 Relationships from Stationary and Dynamic Test Systems

In McGhee's (2005) study, two high-speed systems were used to investigate the relations of texture indicators on various airfields (Wallops) and highway (Smart Road) surfaces. One was the International Cybernetics Corporation (ICC) system which uses a short-range laser range finder, an accelerometer and a distance measuring transducer to measure and compute the roadway profile on the Virginia Transportation Research Council's (VTRC) inertial profiling vehicle. The other was the MGPS system which also uses a laser, an accelerometer, and distance-measuring equipment to collect a very detailed data, the commercial outgrowth of the FHWA's Road surface analyzer project.

Two different high-speed systems were used to measure MPD, and two static systems were used to measure MPD or MTD on the same test sections. In his study the MPD or MTD from static devices can be considered as reference values. For the ICC system, the correlation coefficients at Wallops and the Smart Road were 0.7309 and 0.9208 respectively. For MGPS system, there was a good correlation (R^2 = 0.9227)

between MPDs from MGPS system and CTM. The similar observation results can be found from other studies (Flintsch et al, 2003; Flintsch et al, 2005).

Generally texture indicators measured from static methods are much more repetitive and reproducible than those from high-speed methods since the static methods can exactly use the same pavement surface to conduct multiple measurements, while the high-speed test methods are susceptible to influences of the traffic wandering during data collection. However, the static method is labor intensive, tedious, time-consuming, and is not suitable for large-scale pavement surveys, while the high-speed method can overcome these weaknesses and produce acceptable measurement results.

2.2 Pavement Friction or Skid Resistance

Pavement friction is becoming increasingly important as it is a critical property to prevent accidents on wet roadways (Smith et al, 2006). Substantial studies indicate pavement friction is significantly influenced by a number of factors.

2.2.1 Factors Affecting Pavement Friction

Factors affecting pavement friction encompass roadway geometry, environment, tire properties and pavement surface characteristics, as described in Table 2.2.

Table 2.2 Factors Affecting Pavement Friction

Pavement Surface Characteristics	Road Geometry	Tire Properties	Environment
➢ Micro texture ➢ Macro texture ➢ Mega texture ➢ Material properties	➢ Turing radius ➢ Super elevation ➢ Cross slope ➢ Longitudinal grade	➢ Foot print ➢ Thread pattern ➢ Tire pressure ➢ Load	➢ Wind ➢ Temperature ➢ Water ➢ Snow and ice ➢ Contaminants

Geometric features of the roadway such as turning radius, design speed, cross slope and super-elevation affect the ability of the driver to maneuver safely (Hall et al, 2009). Tire tread design including type, pattern and depth has a significant influence on draining water that accumulates on the pavement surface (Henry, 1983). The environmental features affect driver safety in that water and high temperatures decrease skid resistance (DMRB, 2004). Surface characteristics of the roadway are obviously most important among these four factors since the friction that provides resistance to skidding occurs at the contact areas between the vehicle tire and pavement surface (Williams, 2008).

In light of influences of surface texture on pavement friction, both micro- and macro-texture are highly associated with skid resistance, and their contributions rely on vehicle velocity (Mansour et al, 2005). Micro-texture is the fine scale texture on the surfaces of individual aggregate particles (McDaniel et al 2003), while macro-texture is mainly dependent on aggregate size and gradation for asphalt pavement (Kennedy et al, 1990) and surface texturing for PCC pavement (Hoerner et al, 2003).

At low speed, pavement surfaces with increased micro-texture have higher wet skid resistance because the micro-texture can break the films that coat the individual aggregate particles and increase contact areas between the tires and road surfaces (Mansour et al, 2005). However, the contact time between the tires and micro-texture is shorter and the function of the micro-texture will decrease as the driving speed increases. During rainy weather there is less time for water films to be broken and to escape from the vehicle/surface contact area (Kulakowski et al, 1990). Therefore, micro-texture alone may not provide adequate skid resistance at high speeds on wet pavement surface.

At higher speed, pavement surface macro-texture becomes increasingly important (McDaniel et al, 2003). The macro-texture facilitates to drain off the rainwater on pavements as rapidly as possible so that the roadway/tire interaction are not interrupted by water and hydroplaning risks can be avoided (Mansour et al, 2005; Owen et al, 2005). For these reasons, an increase in macro-texture has been shown to decrease the frequency of fatal accidents in both wet and dry conditions (Henry, 2000).

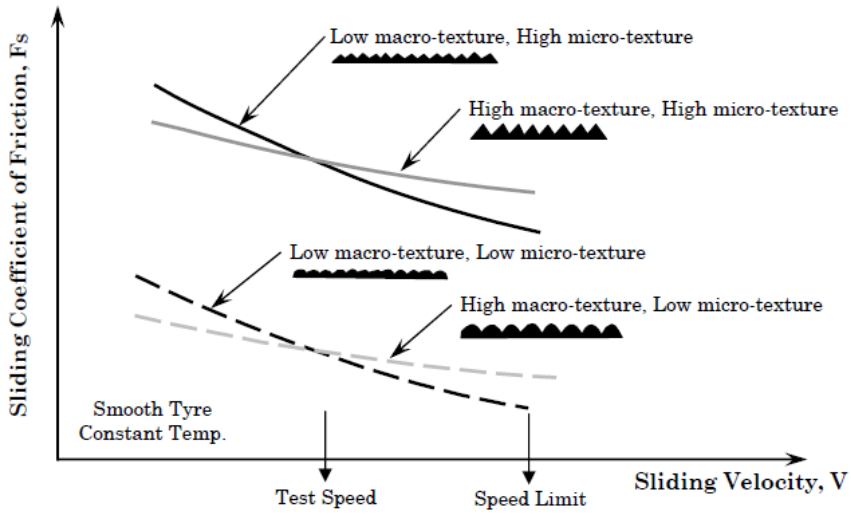

Figure 2.1 Effects of micro-texture and macro-texture on pavement-tire friction at different sliding speeds (Flintch et al, 2003)

As illustrated in Figure 2.1, pavements having good micro-texture and macro-texture maintain a high level of skid resistance regardless of speeds. Pavements having good micro-texture and poor macro-texture may have an equivalent amount of skid resistance at low speeds, but skid resistance decreases as the speed increases. Pavements having poor micro-texture and good macro-texture start with a less amount of skid resistance, but maintain that level of skid resistance as the speed increases. Pavements having poor

micro-texture and poor macro-texture would have a less resistance to skidding at lower speeds, and would present a reduction in skid resistance as the speed increases.

In summary, the micro-texture plays an important role in supplying pavement friction at lower speed, regardless of weather conditions. At higher speeds, the macro-texture would governs the supplies of wet pavement friction. As a result, both micro-texture and macro-texture are necessary to provide adequate skid resistance for the pavements.

2.2.2 Existing Friction Indices

Friction indices have been in use for a long time. In 1965, ASTM started the use of the Skid Number (SN) (ASTM E 274) as an alternative to the coefficient of friction. In later years, AASHTO adopted the ASTM E 274 test method and changed the terminology from Skid Number to Friction Number (FN) (Hall et al, 2009). In the early 1990s, PIARC developed the International Friction Index (IFI), based on the PIARC international harmonization experiment to compare and harmonize texture and skid resistance measurement, conducted in Belgium and Spain in the fall of 1992. Although IFI have been developed three decades ago, but currently the FN is still widely used for network-level pavement surveys in the United States.

2.3 Relationships between Texture and Friction of Pavements

2.3.1 Intrinsic Mechanism

Generally pavement friction is the result of a complex interplay between two principal frictional force components—adhesion and hysteresis (Choubane et al, 2003). Adhesion

force developed at the pavement–tire interface is most responsive to the micro-level asperities of the aggregate particles contained in the pavement surface; whereas the hysteresis force developed within the tire is most responsive to the macro-level asperities formed in the surface via mix design and/or construction techniques, as illustrated in Figure 2.2. As a result of this phenomenon, adhesion governs the overall friction on smooth-textured and dry pavements, whilst hysteresis is the dominant component on wet and rough-textured pavements (Hall et al, 2009).

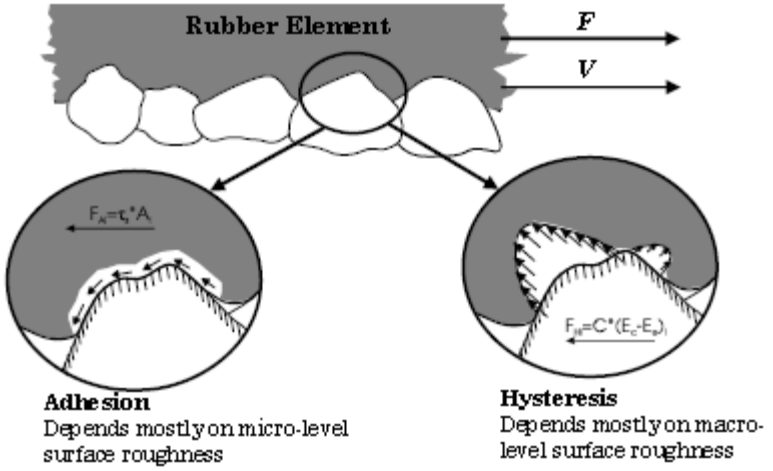

Figure 2.2 Key mechanisms of pavement-tire friction (Hall et al, 2009)

Williams (2009) & Fintch et al (2003) present that micro-texture and macro-texture are both necessary for the enhancement of skid resistance, thus any available measures should be taken to increase both. Increases in micro-texture may be achieved by reducing the aggregate particle size as well as the distance between particles, yet both of these adjustments to a mixture would create a decrease in macro-texture. Increases in macro-texture are beneficial to overall skid resistance at high speeds, and texture depth may be increased by coarsening the aggregate structure and extending the separation between

particles. Greater macro-texture generated larger void spaces at the pavement surface, which reduces the effective contact area of the vehicle tire with the roadway, causing a reduction in micro-texture. Therefore, maximizing both components of skid resistance is not advisable; a tradeoff approach is preferred.

2.3.2 Relationships between Surface Texture and Skid Resistance

Over the years, many studies have been performed to investigate the relationships between texture indicators and frictional indices, some of which attempt to establish acceptable mathematical models to correlate skid resistance with texture characteristics (Rado, 1994; Ergun et al, 2005; Ahammed et al, 2008). Based on pavement surface types, the relations between texture indicators and friction indices can be grouped into three categories, as elaborated as follows:

2.3.2.1 AC Test Sites

The effects of asphalt pavement aggregate spacing on the tire-pavement contact areas and skid resistance were investigated (Fwa et al, 2003). Analysis indicated that the choice of aggregate grading i.e. the asphalt mix design directly influenced the skid resistance of an asphalt pavement surface. The other study also indicated the aggregate gradation and characteristic can be used to predict the asphalt skid resistance (Reazei et al, 2009). In Hall's (2009) study, a total of 13 mixtures were prepared and tested. Two models that correlates skid resistance with aggregate characteristics and gradation were developed, as shown in Equations (2.2) and (2.3):

$$\mathrm{IFI} = 0.081 + 0.732\ \mathrm{DFT}_{20}\exp^{\left(\frac{-40}{S_p}\right)} \qquad (2.2)$$

$$S_p = 14.2 + 89.7\text{MPD} \quad (2.3)$$

where Sp is a parameter related to macro-texture that is measured by the CTM, and DF20 is a measure of frictional resistance at a speed of 20 km/h measured by DFT.

The friction prediction model was also established based on data from nine surface types at two sites (Ahammed et al, 2008). The relations of texture indicators (the MTD from SPM and the MPD from Laser based Profiler) and friction indices (BPN and SN from skid trailer) were analyzed. The results showed the skid resistance increased with the increase of MTD, but decreased with the increase of the traveling speeds.

2.3.2.2 PCC Test Sites

In Mahone's (1977) study, the relations between skid resistance and transverse tines were examined on the PCC pavement surface which have a SN_{40} of 47 for the bald tires after four years of traffic exposure. On test sections the transverse tine has a size of 19 mm spaced, 3.2 mm in width, and 3.2 mm in depth. However, a similar longitudinally tined and an exposed aggregate surfaces were shown to have a SN_{40} of 33 for bald tires. The reason for such large difference in SN between the longitudinally and transversely tined surfaces was presumably associated with the predominant texture orientation.

Grady et al (1981) found that grooved PCC surfaces with MTD of 1.70 mm (0.067 in.) and 0.41 mm (0.016 in.) provide ribbed tires with SN_{40} of 62 and 35, respectively. For the same pavement, the SN was shown to vary by 9 to 22 points for a difference in MTD of 0.10 mm (0.004 in.) to 0.23 mm (0.009 in.). Overall, a mean groove depth (MGD) of 1.27 mm (0.05 in.) was found to be necessary for a minimum acceptable ribbed tire SN40 of 32.

Yager et al (1982) found no correlations between the BPN and macro-texture, whereas Olek et al. (2004) found a linear relationship between the BPN and macro-texture on PCC surfaces, and Ahammed et al (2008) found a quadratic relationship between MTD and BPN for PCC surfaces. The PCC specimens with 16 texture types were soaked in water for 24 hours prior to friction testing, afterwards MTD was measured using SPM while the friction (BPN) was measured using British Pendulum Tester. The Figure 2.3 showed the result of comparisons of BPN and MTD for PCC surfaces.

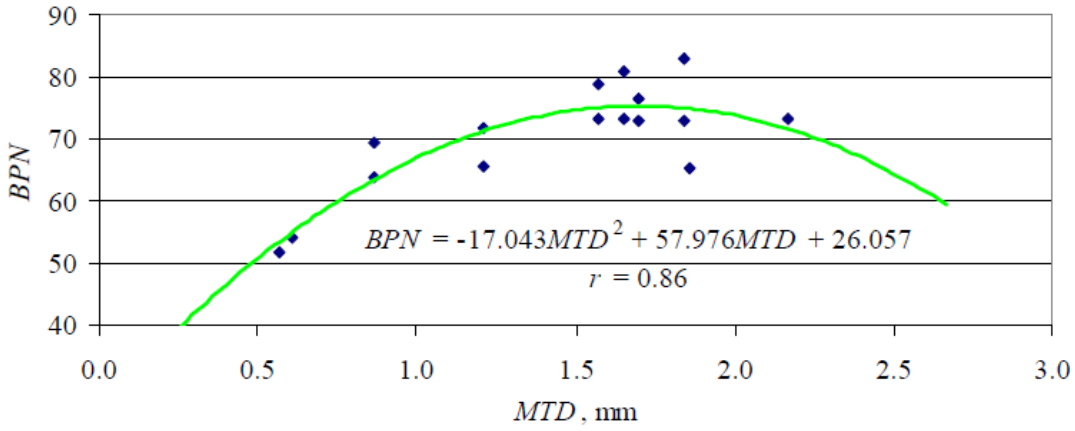

Figure 2.3 Relationship between BPN and MTD (Ahammed et al, 2008)

As shown in Figure 2.3, the BPN varies with the change of MTD, and the skid resistance increases to the maximum value at a MTD of about 1.8mm and decreases thereafter as the MTD further increases. And the skid resistance prediction model with a good correlation ($R^2 = 0.86$) was developed.

2.3.2.3 AC and PCC Test Sites

Based on test results from 18 various surface types including PCC and AC pavements, Ergun et al. (2005) proposed a friction coefficient prediction model with macro- texture and micro-texture parameters, as described in Equation (2.4). In Ergun's study the average wavelength was taken into account as an important parameter. A good correlation with the value of 0.896 can be obtained by comparing the measured values and predicted values. However, this model is involved several parameters such as La_{mic}, which cannot be accurately obtained in the fields.

$$F(S) = \left(0.37 + \frac{0.11}{MPD_{mac}} + \frac{0.15}{La_{mic}}\right) \times e^{-(S/(149+81Log(MPD_{mac})+80Log(Rq_{mic}))} \qquad (2.4)$$

where $F(S)$ – friction coefficient at slip speed S; MPD_{mac} - mean profile depth related to macro-texture; La_{mic} - average wavelength of surface profiler related to micro-texture; S - slip speed; Rq_{mic} - root-mean-square deviation of surface profile related to micro-texture.

Another study was conducted by PIARC, attempting to propose a new index which allow for the harmonizing of friction measurements taken with different equipment and/or at different slip speeds to a common calibrated index (Hall et al, 2009). ASTM E1960 provides International Friction Index (IFI) to harmonize frictions reported from various devices. IFI includes measurements of both macro texture and friction on wet pavements: a speed constant or number derived from the macro texture measurement that indicates the speed-dependence of the friction and a friction number corresponding to a slip speed of 60 km/h (40mph).

The IFI is based on the assumption that the friction is a function of speed and macro texture and that the value of friction is reduced as the speed increases for a specific

pavement surface macro texture. The mathematical relationships are shown in Equations (2.5)-(2.7):

$$S_p = a + b \times TX \tag{2.5}$$

Where: SP = IFI speed number; a, b = Calibration constants dependent on the method used to measure macro-texture. For MPD (ASTM E 1845), a = 14.2 and b = 89.7; For MTD (ASTM E 965), a = –11.6 and b = 113.6; TX = Macro-texture (MPD or MTD) measurement, mm.

$$FR(60) = FR(S) \times e^{(\frac{S-60}{S_P})} \tag{2.6}$$

where: FR (60) = Adjusted value of friction measurement FR(S) at a slip speed of S to a slip speed of 60 km/hr with a ribbed (R) tire; FR(S) = Friction value at selected slip speed S with a ribbed(R) tire; S = Selected slip speed, km/hr.

$$F(60) = A + B \times FR(60) + C \times TX \tag{2.7}$$

Where: F (60) = IFI friction number obtained from the correlation of equation 8; A, B = Calibration constants dependent on friction measuring device; C = Calibration constant required for measurements using ribbed tire.

Upon obtaining the speed number S_p and IFI friction number F (60), the fiction number at any speed can be estimated using the Equation (2.8):

$$FN(S) = F(60) \times e^{-(\frac{S-60}{S_P})} \tag{2.8}$$

Note that the F (60) is calculated from the FR(S) which is measured using locked wheel trailer. However in practical applications, two alternatives can be used in lieu of the locked wheel method, namely BPN and MTD based IFI friction prediction (ASTM E303), and DFT20 and MTD based IFI Friction Prediction (ASTM E 1911).

In spite of the substantial studies on the relationships between texture and skid resistance gained over past decades, the above-mentioned models solely consider effects of surface texture on skid resistance, regardless of rubber tire properties, tire pressure, and temperature which are important factors affecting pavement friction.

2.4 Rubber Friction on AC Pavements

In addition to the texture-related parameters, pavement friction can also be predicted based on contact mechanics and rubber friction theory (Hui et al, 2000, Klüppel et al, 2000; Persson et al, 2001). A smooth rubber surface and a rigid pavement surface are assumed in this theory. The smooth rubber surface can be described with different models such as Kelvin-Voigt Slider and Zener Slider (Klüppel et al, 2000). The rigid pavement is assumed to be a self-affine surface that is described by the power spectral and height correlation difference function (Torbrueggeet al, 2015; Ueckermann et al, 2015). The elastic contact and penetration depth between rubber and pavement surfaces can be described with various models such as Greenwood and Williamson Theory (Greenwood et al, 1966).

Rubber friction is dependent on several components namely hysteresis, adhesion, cohesion, and viscosity (Ueckermann, et al 2005). When rubber tire blocks slide on a rough surface, the asperities exert oscillating forces on the rubber resulting in energy dissipation due to internal damping of the rubber. The energy dissipation to be coupled with characteristic length scales of the surface texture. The adhesion component is derived from attractive binding forces between the rubber surface and pavement surface. It is important only for clean, dry pavement surfaces under low sliding velocities. The

cohesion component of rubber friction represents the energy required to produce new surfaces, and is associated with grooving of the rubber and abrasive wear. The viscous friction component arises from shearing of a viscous layer between tire and road surface, only occurred on wet roads. The shearing generates a hydrodynamic pressure that lifts the tire from the pavement leading to an increased hydroplaning risk depending on the speed and water film thickness. Pioneering studies indicated rubber friction was most contributed by hysteresis and adhesion components (Choubane et al, 2003, Hall et al, 2009; Ueckermann, et al, 2005).

Recently much work has been done on mathematical models that allow to quantitatively estimate the friction coefficient of rubber sliding on a hard, rough surface (Klüppel et al, 2000; Persson et al, 2001). These theories mainly deal with the hysteresis component which is considered as the major contribution to rubber friction. In this study two widely used predictive models developed by Persson and Heinrich/ Klüppel are summarized.

Both Persson's model and the Heinrich/ Klüppel have a physical foundation and need input information about the complex modulus of the rubber, the statistical roughness of the substrate, the contact pressure, sliding speed and temperature. The general approach is quite similar. However, the contact model used in Heinrich/ Klüppel model is based on the Greenwood-Williamson Theory (Greenwood et al, 1966), while Persson develops a new three-dimensional contact mechanics theory (Persson, 2006). Both models consider the surface roughness on multiple length scales and thus need the viscoelastic properties of the elastomer to be known over a wide frequency range. Heinrich/Klüppel calculates

the hysteresis friction coefficient based on a two-dimensional approach while Persson's model is fully 3D and based on three-dimensional data (i.e. the pavement surface). The predictive capabilities of both models have been investigated by comparing the predictive results with experiments, and a good agreement was found (Westermann et al, 2004).

2.5 Groove Performance Evaluation on PCC Pavements

Pavement grooving, a particular surface characterization technique, has been broadly used on airfield pavements and roadways to improve pavement skid resistance and reduce the occurrence of potential hydroplaning (Horne et al, 1962; Beaton et al, 1969; Mosher 1969).

Field studies and research efforts have proven effectiveness of grooves in reducing skid resistance-related accidents on both roadways and runways (Yager, 1969, Horne et al, 1969; McCarty, 1971; Martinez, 1977; Harwood et al, 1978; Wong 1990, Chambers, 2003; Toan, 2004; and Lee et al, 2009). In addition, hydroplaning speed prediction models have been developed to investigate the relationships between skid resistance and groove dimensions (depth, width, and spacing) (Ong et al, 2006a; Ong et al, 2006b). Results indicate larger groove depth and width, and tighter groove spacing would result in better frictional properties. Particularly, in Ong's studies changes in groove depth are found to have the most significant effect on hydroplaning.

Groove performance deteriorates over time due to effects of repetitive traffic loading on groove dimensions. However, field evaluation of runway grooves is not commonly performed due to the limitations of data collection technology and to a certain level, data analysis software. Currently three categories of groove identification techniques have

been utilized to automatically measure groove dimensions (Lee et al, 2009; Rapol et al, 2010; Wang et al, 2013a; Wang et al, 2013b). However, all the three types of methods have limitations. The cluster based technique is unsuitable for the measurements of abrasive or worn grooves since the identification of grooves is based on the cluster analysis results of profile slopes (Lee et al, 2009). In addition, this method requires subjective threshold to distinguish outside-groove points and inside-groove points. The low-pass based technique (Rapol et al, 2010; Wang et al, 2013b) cannot efficiently eliminate the influences of narrow dips. As a result, this method is prone to miss the identification of shallow grooves. The gradient based method produces a pair of dip and spike based on the gradient of each groove. Subsequently forward and backward traversal techniques are used to determine the starting and ending points of each groove (Wang et al, 2013a). One drawback of this method is that an appropriate threshold is needed to be applied to determine groove locations.

In addition, there are three types of approaches on groove performance evaluation. The first is to estimate hydroplaning speed based on simulation models. The higher the hydroplaning speed is, the better the groove performance is (Ong et al, 2006a; Ong et al 2006b; Luo et al, 2014). The second approach is to measure runway skid resistance in the field (FAA, 1997; Lee et al, 2009). The higher the friction number is, the better the groove performance is. The last technique is to evaluate groove performance by comparing the measured groove dimension with the standard groove configuration (FAA, 1997; Lee et al, 2009; Rapol et al 2010; Wang et al; 2013a).

2.6 Summary

This chapter summarizes the pioneering studies on texture measurement, texture characterization techniques, the relationships between pavement texture and friction, rubber friction theory, and groove identification, measurement, and evaluation. Based on the extensive knowledge, several limitations can be found and given as follows:

- ✓ For texture data collection, although there are various profile and texture acquisition systems, the collected data cannot cover the entire lane. In addition, most data collection systems are designed and operated at low speeds and not suitable for the network level pavement surveys.
- ✓ For texture characterization, the existing texture indicators mainly involve in MPD, MTD, and RMS, which solely reveals partial texture properties and inadequate to reflect overall features of pavements.
- ✓ For rubber friction prediction on AC pavements, most efforts are restricted to the theory study phase. The predictive models have not been applied for project- or network- level pavement safety evaluation.
- ✓ For grooving measurement and evaluation, there are three drawbacks in terms of current data collection systems and groove identification algorithms: 1) being incapable to obtain entire lane texture data and measure longitudinal groove dimensions; 2) being lack of robust filters and algorithms to identify grooves or joints; 3) being short of the efficient index to reveal the groove drainage capability.

In this paper 1mm 3D texture data would be continuously collected using the DHDV with the latest PaveVision3D Ultra. The collected texture data covers the full lane, with

the width up to 4 m, based on which pavement safety evaluation can be conducted from the following aspects: 1) to characterize pavement surface texture properties with a series of texture indicators and pavement friction can be predicted based on the texture indicators; 2) to use Heinrich/Klüppel model to predict the sliding friction coefficients on AC pavements; 3) to automatically identify and measure grooves, and compare the calculated groove dimension or volume with the design values or the given evaluation guideline.

CHAPTER 3. DATE PREPARATION AND PREPROCESSING

3.1 Digital Highway Data Vehicle (DHDV) with Pavevision3D Ultra

DHDV, developed by the WayLink Systems Corporation with collaborations from the University of Arkansas and the Oklahoma State University, has been evolved into the sophisticated system to conduct full lane data collection on roadways at highway speed up to 60mph (about 100 km/h).

The latest Pavevision3D Ultra is multi-functional and includes four sub-systems: 2D/3D pavement surface imaging, Right-of-Way (ROW) imaging, road profiling, and road geometry measurement. Some auxiliary systems are incorporated in this system as well, including Global Positioning System (GPS) receiver, power supply equipment, system control board, the computer workstations inside of the van, the Distance Measurement Instrument (DMI) connected to the wheel, and newly integrated Ames high-speed profiling system.

In this system the signal to acquire image and profile data are controlled and triggered by DMI. The signal to capture the IMU data is controlled and triggered by GPS receiver. The overall architecture of the PaveVision3D Ultra system can be schematically described in Figure 3.1.

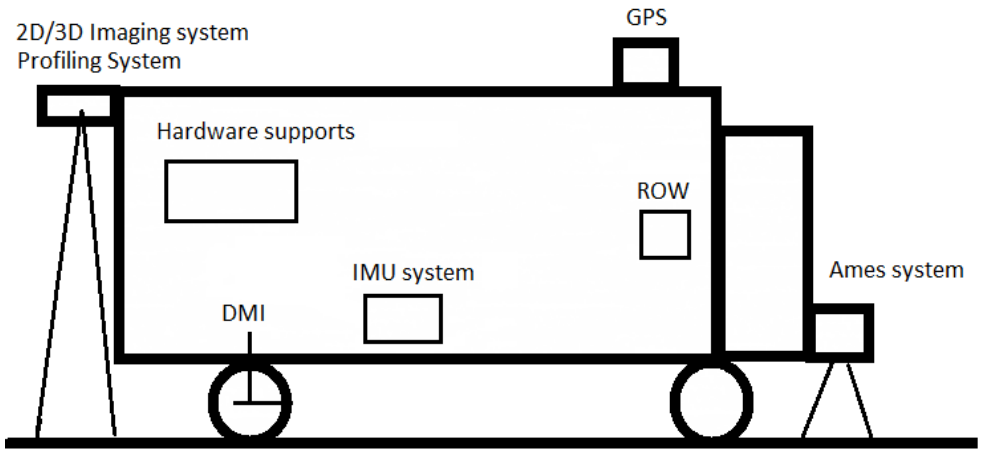

Figure 3.1 The schematic of overall architecture of 3D Ultra

With the high power line laser projection system and custom optic filters, DHDV can work at highway speeds during daytime and nighttime and maintain image quality and consistency. 3D Ultra is the latest imaging sensor technology that is able to acquire both 2D and 3D laser imaging data from pavement surface through two separate left and right sensors. Each sensor in the rear of the vehicle consists of two lasers and five special-function cameras. For the two lasers, one is for providing 2D visual illumination and the other one is for providing the 3D data illumination. For the five cameras, four cameras are for capturing 3D laser illumination and the other one is for capturing 2D laser illumination.

The resolution of surface texture data in vertical direction is about 0.3 mm and in the longitudinal direction is approximately 1 mm at 60MPH data collection speed. An example of 2D and 3D pavement surface image is illustrated in Figure 3.2. Figure 3.2 (a) shows the 2D pavement surface with the marked manholes: Figure 3.2 (b) shows the 3D visualization of the corresponding manholes; and Figure 3.2 (c) represents the close-up manholes.

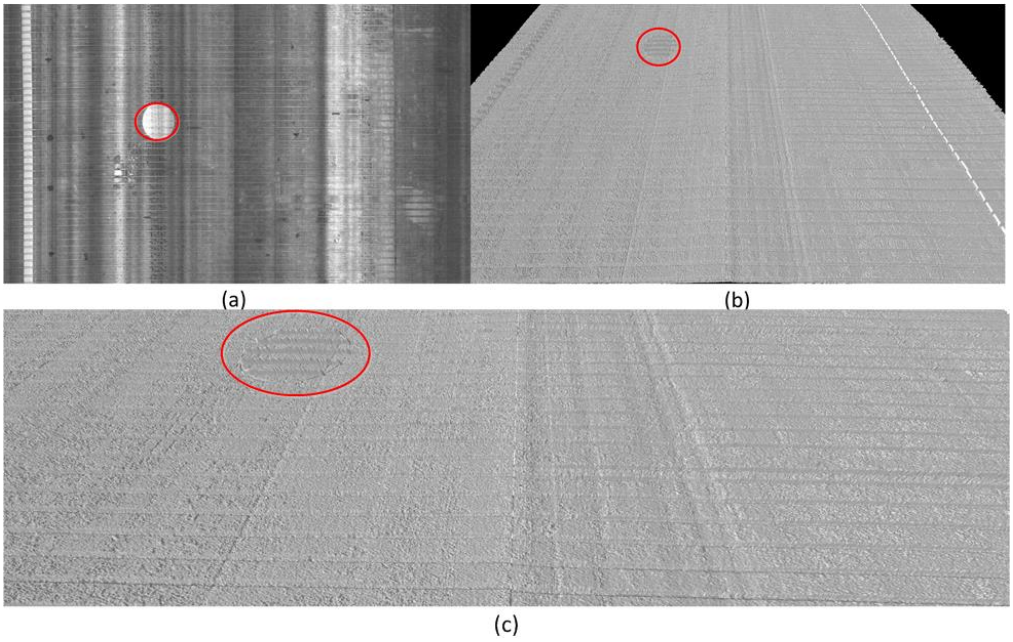

Figure 3.2 2D and 3D visualization (a) 2D image, (b) 3D image, and (c) zoomed-in 3D image

Aside from the 2D/3D, ROW, and IMU data, DHDV can also collect texture data with Ames high-speed profiling system. Each data set alone or in combination have various applications in pavement engineering, as illustrated in Figure 3.3. Recently two 3D high resolution digital accelerometers have been installed on the DHDV, which

allows DHDV to be capable of reporting various roughness indices such as International Roughness Index (IRI), and Boeing Bump Index (BBI).

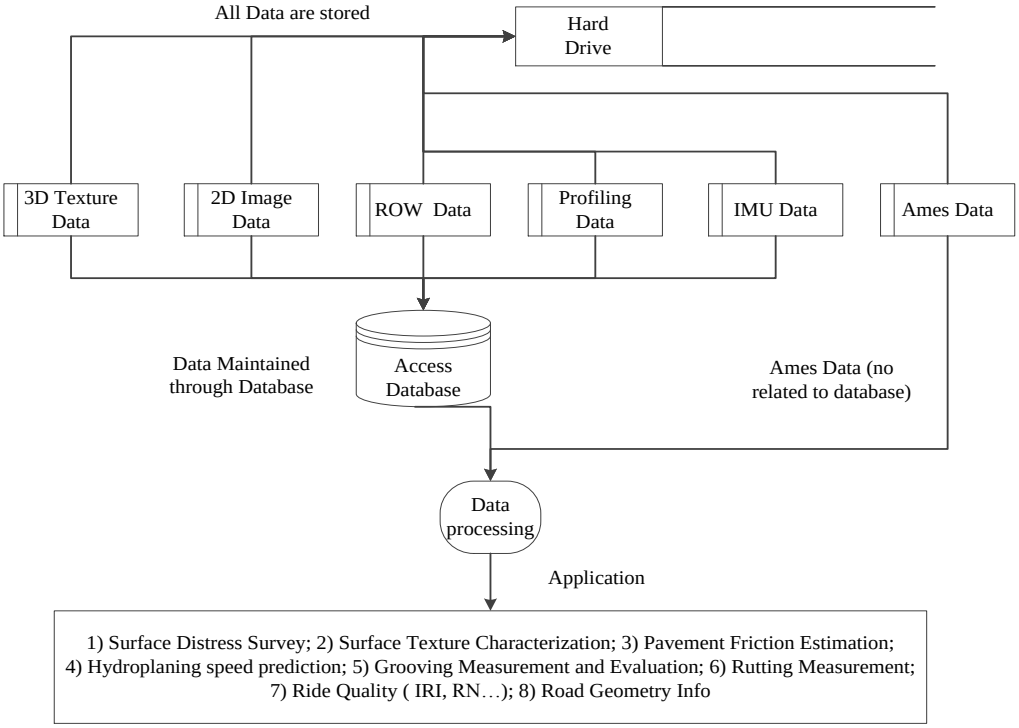

Figure 3.3 Applications of various data in pavement engineering

3.2 Elevation Difference Reduction

It should be noted that, during data collection, unexpected errors might be produced due to the presence of non-uniformity of laser intensity, lens distortion, physical installation locations of cameras, vehicle suspension system, the traveling speed, as well as pavement surface debris, which would cause a large difference in elevation for both sides of an image or two adjacent images. Therefore ensuring the elevation data that has the smooth transition in transverse and longitudinal directions places a significant role in the subsequent data processing analysis.

3.2.1 Introduction

In this study the large elevation difference between two sides of an image is named as the transverse alignment problem; while the large elevation difference between two adjacent images is named as the longitudinal alignment problem. An example to illustrate the two types of alignment issues is given in Figure 3.4.

In Figure 3.4(a), the grayscale image is 2D visualization of the 3D elevation data. Generally the larger the elevation values are, the brighter the grayscale image would be. If there are no transverse alignment issues, a smooth transition from the left side to right side would be observed. However, in this case the transverse alignment issue is pretty apparent because there is a sharp change in elevation at the stitching area between left and right sides of the image. The similar issue can be observed in Figure 3.4 (b), which is caused by the large elevation difference in two adjacent images.

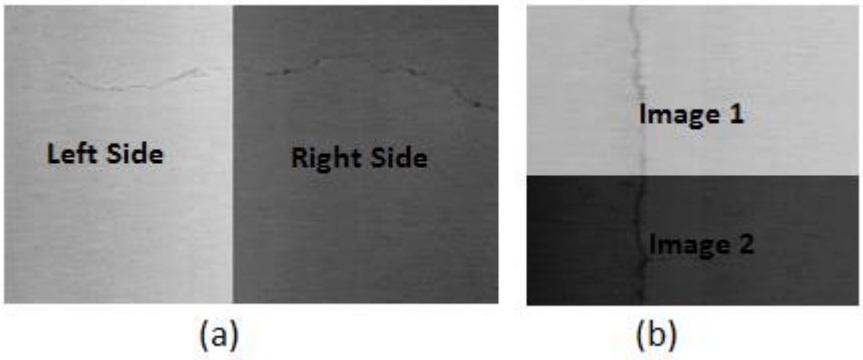

Figure 3.4 Screenshots of (a) transverse alignment issue; (b) longitudinal alignment issue

In this study one elevation difference reduction approach is proposed to eliminate these errors. This approach is targeted at ensuring there is a smooth transition in elevation between left and right sides of each image or between two adjacent images.

3.2.2 Zero Reference Plane based Approach

The zero reference plane based method is based on the idea that all the stitching edges between the two adjacent images or two sides of an image should be smooth in elevation. The basic principle of this approach is to locate each subarea and assure the average value of data within each subarea equals to zero (Figure 3.5). Subsequently, a constant value (e.g. 100) is added to each data element within each subarea and guarantee all the data element are non-negative. Accordingly the newly aligned data elevations are obtained, and the results indicate the method is reliable in addressing the transverse or longitudinal alignment problems.

Figure 3.5 Division of four subareas of a sample

An example is given to illustrate the implementation of this elevation difference reduction approach. Assume the data within the four subareas (each shading color represents one subarea) have a large difference in elevation, as described in first half part of Table 3.1.

Table 3.1 Elevation Comparison before and after Alignment Reduction

	Raw Elevation Data				Elevation Data After Alignment Reduction			
	Left Side		Right Side		Left Side		Right Side	
IMG 1	120	124	65	63	98	102	102	100
	122	122	62	62	100	100	99	99
IMG 2	165	169	214	214	98	102	100	100
	167	167	216	212	100	100	102	98

To utilize this method to realign the elevation data within the four subareas, a formula is developed and mathematically expressed in Equation (3.1).

$$f_{ne}(m, n, i, j) = C + f_{oe}(m, n, i, j) - Ave_{sub}(m, n) \quad m, n \in [1,2] \tag{3.1}$$

where $f_{ne}(m, n, i, j)$: the newly aligned elevation at point (i, j) for subarea (m, n); C: the constant value; $f_{oe}(m, n, i, j)$: the original elevation at point (i, j) for subarea (m, n); $Ave_{sub}(m, n)$: the average elevation value of subarea (m, n).

Equation (3.1) is applied to each original data to calculate the newly aligned elevations. The new elevation (shaded by orange color) are described in the second half part in Table 3.1. It can be observed that there is a relatively smooth transitions between the stitching areas between adjacent subareas.

3.2.3 Comparisons of Before- and After- Alignment Reduction

Figure 3.6 shows the 2D visualization of two adjacent 3D images. Note that elevations at both sides of these two images are different, so the artificially synthesized 2D image has different brightness or intensities at these four subareas. Apparently this phenomenon is caused by the transverse and longitudinal alignment problems.

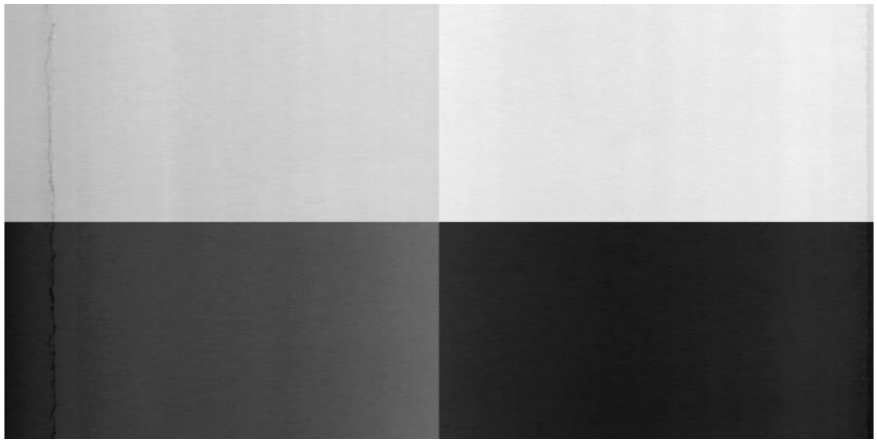

Figure 3.6 2D visualization of 3D images by stitching two adjacent images

To tune up the unevenness of brightness across the grayscale image, the zero reference plane based approach is used, and the result after elevation difference reduction is illustrated in Figure 3.7. Note that data elevation differences across the entire sample can be efficiently suppressed.

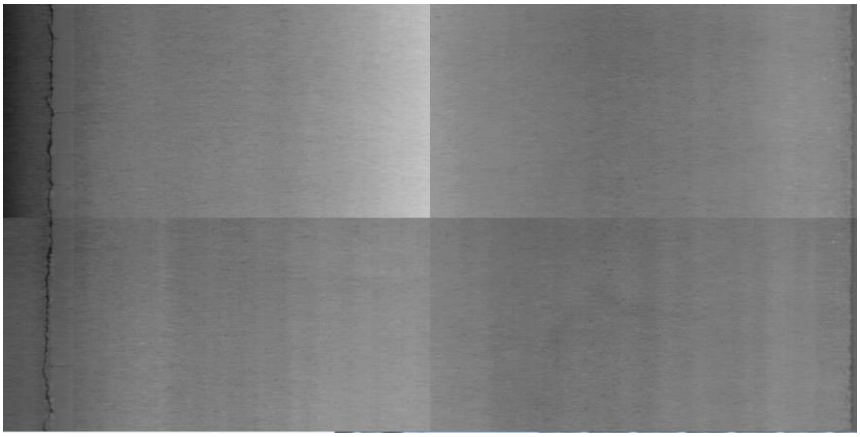

Figure 3.7 Grayscale image of two adjacent images after elevation difference reduction

3.3 Invalid Data Repair

Due to illumination unevenness in laser optics or limit of Area of Interest (AOI) of 3D cameras, there are small percentages of 3D data points that have unusually high values or

zero values. These invalid pixels or readings are not actual representations of the pavement surface texture, so techniques should be employed to repair these invalid readings (Wang et al, 2012).

In terms of invalid data detection and identification, two primary principles are generalized: (1) the "zero" values in the image should be eliminated and replaced; (2) some values are unusually higher than their surroundings, and actions should be taken to repair the data. In the study neighborhood average based method is presented to repair invalid data.

This method is to replace the invalid reading with the average values of nonzero neighborhood points centered at the current point. The two points based average method is to use average values of the previous and next points of the invalid data to replace the invalid data, which is performed on one longitudinal profile; 3x3 matrix based average method uses the eight adjacent points of the invalid data as basis of computation. Based on experiments conducted in the research, the 3x3 matrix method is more effective in repairing the in valid values, which is used as the basis for the subsequent data repair.

The method can be implemented by convolving the predefined weight mask with the neighborhood centered at the invalid reading. Figure 3.8 illustrates the mechanics of the linear data repair method using a 3 x 3 neighborhood. At any invalid point, $f(x, y)$, the neighborhood averaging response, $g(x, y)$, is the sum of products of the mask coefficients, $w(s, t)$, and their corresponding neighborhood image pixels, $f(x + s, y + t)$, divided by the sum of the mask coefficients, N, as shown in Equation (3.2). Table 3.2 and Table 3.3 show the invalid data and the repaired data, respectively.

$$g(x,y) = \frac{1}{N} \times \sum_{s=-1}^{1} \sum_{t=-1}^{1} w(s,t) * f(x+s, y+t) \qquad (3.2)$$

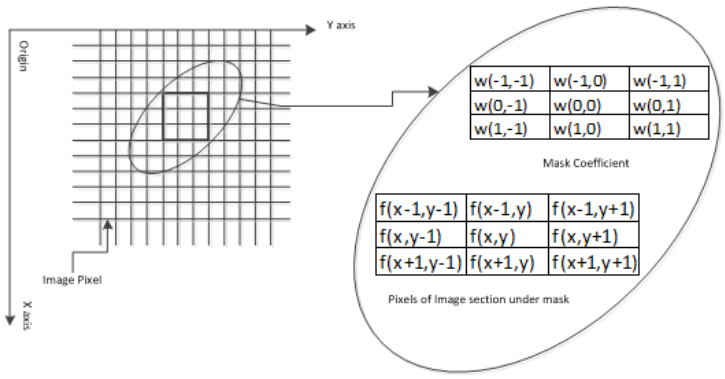

Figure 3.8 Mechanics of data repair method using 3x3 mask

Table 3.2 Eaxmple of Invalid Height Data

Pixel Values in Longitudinal Profile (Unit: mm)											
574	580	560	0	567	567	568	567	561	567	580	575
582	**592**	568	560	560	567	567	560	567	567	575	567
583	575	567	567	560	568	568	0	567	567	0	567
574	567	561	574	567	567	0	0	560	567	560	567
567	567	574	573	580	560	0	0	560	560	560	567
574	574	583	567	568	567	0	0	567	560	575	567

Table 3.3 Example after Invalid Data Reduction

Pixel Values in Longitudinal Profile (Unit: mm)											
574	580	560	563	567	567	568	567	561	567	580	575
582	**574**	568	560	560	567	567	560	567	567	575	567
583	575	567	567	560	568	568	566	567	567	567	567
574	567	561	574	567	567	566	565	560	567	560	567
567	567	574	573	580	560	565	564	560	560	560	567
574	574	583	567	568	567	567	567	567	560	575	567

3.4 Digital Filtering Techniques

Data filtering techniques are usually employed to suppress unwanted information in signal or image processing, and can be implemented in spatial or frequency domain. The

spatial domain refers to the image plane itself so that filtering operation is based on the direct manipulation of pixels in an image. The frequency domain means the analysis of data or signals with respect to frequency rather than time.

Spatial filtering can be implemented using convolution operator, while frequency filtering needs to be implemented through Fourier transform, filtering, and inverse Fourier transform. Frequency filtering has one prominent advantage over spatial filtering, that is, the waveband or frequency of interest can be well preserved since its operation is based on the frequency. Therefore, in this study the frequency filtering techniques are used to characterize pavement surface macro-texture properties.

3.4.1 Wave Number Determination

The selection of wavelengths of interest is the key component in frequency filtering, and also plays a significant role in surface characterization. For filtering techniques, the low pass filter is used to remove data information with short wavelengths, and the high pass filter is used to eliminate data information with long wavelengths. Band pass filter is employed to pass frequencies or wave numbers within a range and to reject frequencies or wave numbers outside that range. In this study the determination of wavelength of concern is dependepent on three factors: the ASTM standard, the macrotexture definition, and the 3D data resolution.

ASTM standard specifies the surface profile must be filtered by one of the two following methods before MPD is calcualted (ASTM E1845):

1) Applying a high-pass filter to remove wavelengths no less than 100 mm, followed by is using a low-pass filter to remove wavelenghts no greater than or 2.5mm; or

2) Applying a low pass filter to remove wavelenghts no greater than 2.5 mm, followed by is suppressing profile slope by substracting a regression line from the profile.

Accordingly the band pass ranged from 10 to 400 cycle/m should be utilized to compute the MPD. However, according to the definition of pavement macro-texture, the wavelengths of interest for macrotexure is ranged from 0.5 to 50mm, so its corresponding wave numbers are ranged from 20 to 2000 cycle/m. According to the "Nyquist sampling theorem" (Sayers et al, 1998), it is necessary to set the sample interval to be no larger than a half of the wavelenght of the sinusoild in order to capture a sinusold in sampled road profile,which indicate that the cycle for the minimum wavelength is supposed to occupy at least two sampled elevation points, that is, no less than 2mm for the raw images with 1mm resolution. Therefore, the range of wave number of interest mainly concentrates between 20 and 500 cycle/m in this study.

3.4.2 Filtering Methods in Frequqncy Domain

Once the wavelengths of concerns are detemined, the subsequent task is to choose the proper filter to cut off the unwanted wavelenthts. There are two band filters availabe, including ideal band pass filter and Butterworth band pass filter (Gonzalez, 2009). The ideal band pass filter with frequency range $[D_L \ldots D_H]$ is defined in Equation (3.3):

$$H(u,v) = \begin{cases} 1 & \text{if } D_L \le D(u,v) \le D_H \\ 0 & \text{otherwise} \end{cases} \qquad (3.3)$$

Where D_L represents cut-off frequency for low pass filter, D_H represents the cut-off frequency for high pass filter, $D(u,v)$ is the distance between a point (u,v) and the origin (the center point of frequency rectangle), as Equation (3.4) shows.

$$D(u,v) = [\left(u - \frac{N}{2}\right)^2 + \left(v - \frac{M}{2}\right)^2]^{1/2} \quad (3.4)$$

Where, N and M are the image size.

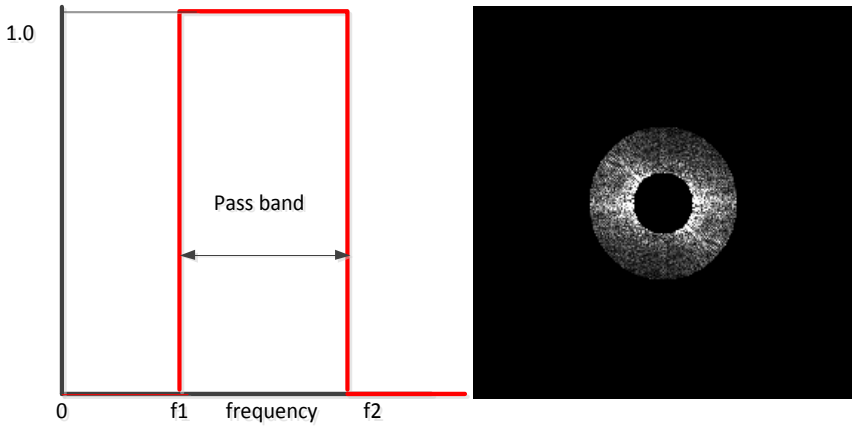

Figure 3.9 Schematic for Ideal band pass filter

The ideal band pass filter is described by Figure 3.9. The filter is used to keep wave numbers ranged [f1, f2] unchanged, and assign zeroes to other amplitudes outside the band ranges in Fourier image. Different with the ideal band pass filter, Butterworth band pass filter does not have a sharp discontinuity that gives a clear cutoff between passed and rejected frequencies. Butterworth band pass filter with frequency range [$D_L \ldots D_H$] can be mathematically depicted as the Equation (3.5):

$$H(u,v) = \frac{1}{1 + \left[1 + \frac{2(D(u,v) - D_H)}{D_H - D_L}\right]^{2n}} \quad (3.5)$$

Where D_L is cut-off frequency for low pass filter, D_H represents the cut-off frequency for high pass filter; D (u, v) is the distance between a point (u, v) and the origin (the center point of frequency rectangle), n is the orders of this transfer function.

Similarly, Butterworth band pass filter can be described by Figure 3.10. The band filter is to make wave numbers [f1, f2] unchanged, but there is a gradual discontinuity between passed and rejected frequencies or wave number. Unlike the ideal band filter, some subtle weight values are assigned to other pixels outside the band ranges in Fourier image.

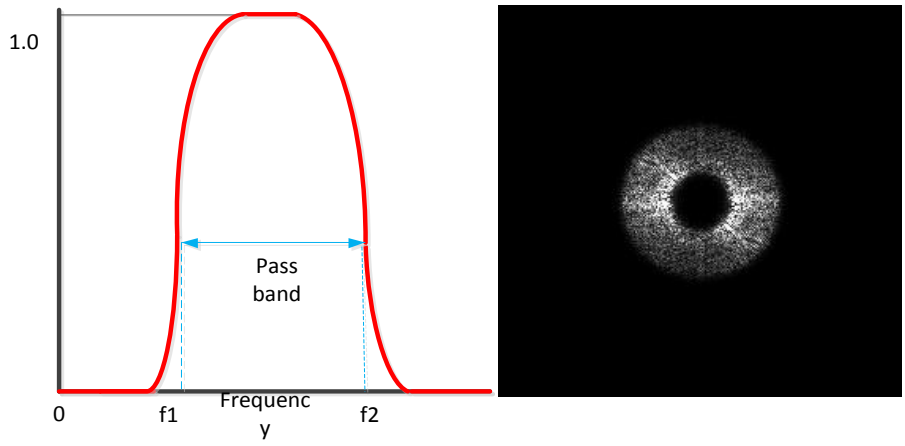

Figure 3.10 Schematic for Butterworth band pass filter

In summary, these two filtering operations are conducted in Fourier domain. Subsequently the inverse Fourier transform needs to be implemented to transform the 3D data back into the space domain for the further processing. The newly produced data is termed as the filtered data, which can be directly used to conduct pavement surface texture characterization.

3.5 Data Sampling Principle

The 1mm 3D texture data collected using DHDV is stored on computer Solid State Drive (SSD) in the form of raw images. Each raw image has a size of 4096 pixel wide by 2048 pixel long, and is served as the basic element to constitute a sample. The entire pavement

section can be virtually constructed by sequentially stitching each individual raw images. Samples with any size can be specified based on the virtual pavement section, as shown in Figure 3.11.

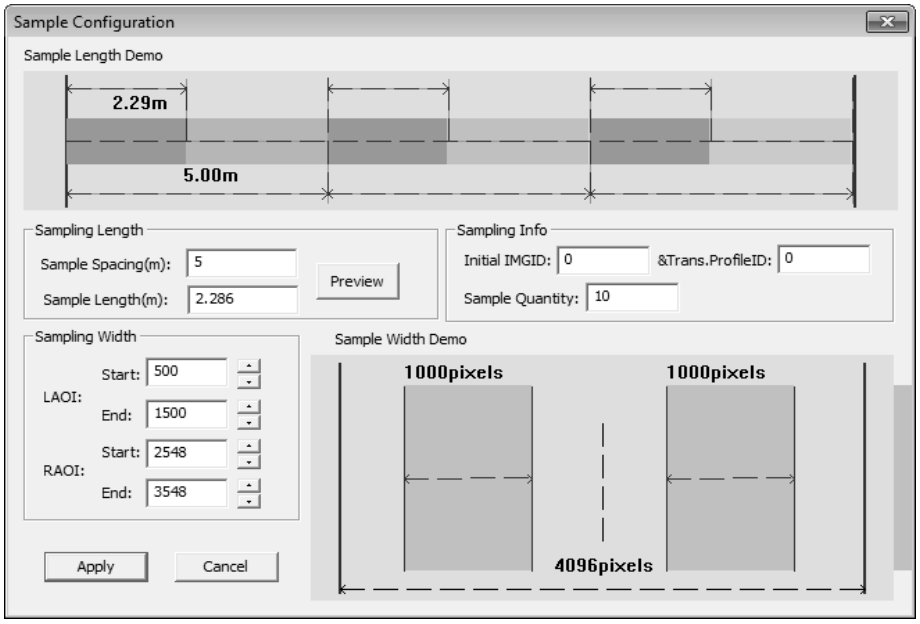

Figure 3.11 Data sampling operation interface

In Figure 3.11, sample spacing is defined as the distance between two adjacent samples. Sampling length and width are defined as the size of data of interest for data processing and analysis, which can be specified through the interactive interface in Figure 3.11. As the demo shows, the sample spacing is 5m, which means one result would be reported every 5m; the sample length is 2.29m and sample width is 1000 pixels. In addition, the starting image and sample quantity of concern can be set in this interface as well.

3.6 Data Repeatability Test

Due to impacts of traffic wandering and vehicle vibrations on data collection, the collected 3D data might be different for each measurement or pass. In this study one or multiple longitudinal profiles are extracted from 3D surface texture data for repeatability test. The cross correlation method would be used to describe how two test profiles agree with each other. The low correlation coefficient would be obtained if the two longitudinal profiles do not agree well, in contrast, the high correlation coefficient (e.g. 1) would be obtained if two longitudinal profiles agree perfectly.

3.6.1 Cross Correlation

Cross correlation function is a statistical measure of the dependence of one variable on another (Karamihas, 2005). The cross correlation function of repetitive measurements of road profiles provides a way to synchronize them and rate their agreement. For two measures of road profile, the cross-correlation function is defined as (3.6):

$$CC(\nabla) = \lim_{L\to\infty} \frac{1}{L} \int_0^L f_1(x)\, f_2(x+\nabla) dx \tag{3.6}$$

Where f_1 and f_2 are each measurements of road profile as a function of distance x with length L. The correlation function exists as a continuous function of the offset distance ∇ between the profiles. Since actual measures of road profiles are finite in length and sampled as discrete intervals, the integral is replaced with summation. A correlation coefficient also exists and is defined as the correlation function normalized by the standard deviations of σ_{f_1} and σ_{f_2}. The mathematical description is given in Equation (3.7):

$$N_{cc}(\nabla) = \frac{1}{\sigma_{f_1}\sigma_{f_2}} \sum_{i=1}^{N} f_1(x_i) f_2(x_i + \nabla) \tag{3.7}$$

Where N is the number of points common to both profiles at an offset distance ∇ (equal to an integer multiple of the sample interval), and σ represents standard deviation of each profile. If the profiles are in exact agreement, the cross correlation will have a value of 1. If they are exactly opposite, cross correlation will be -1. If they are uncorrelated, N_{cc} is zero.

3.6.2 Field Test Results

In this study the repeatability test is conducted on a transversely tined concrete pavement which is located on the 12th St, Stillwater OK, with a segment length of 1125ft. The Profile Viewing and Analysis (ProVAL in short), an engineering software application used to view and analyze pavement profiles, is used to measure the agreements of the profiles collected in 12 passes.

Among 12 passes, the starting locations might not exactly match for each pass. To overcome this limit, the ProVAL profile synchronization module is used to determine the proper offset of the comparison profile(s) by matching with the starting point of the basis profile. Since any two measured profiles are not exact copies of each other, the software must be utilized to determine the optimum offset. In addition, Butterworth band pass filter ranged at [5ft, 100ft] is applied on the raw profiles to remove unwanted information.

In this case the profile labeled as LRdetph_4Cam_150a_01_LElev is considered as the basis profile, and the other 11 profiles are termed as the comparison profiles. In

Figure 3.12, the maximum cross correlation coefficients are obtained by synchronizing the comparison profiles with the basis profile. Note that the comparison profile having the best agreement with the basis profile is the LRdetph_4Cam_150a_01_LElev, with a correlation coefficient of 96.74%. The profile of LRdetph_4Cam_150a_012_LElev has the lowest correlation coefficient, with a value of 87.57%.

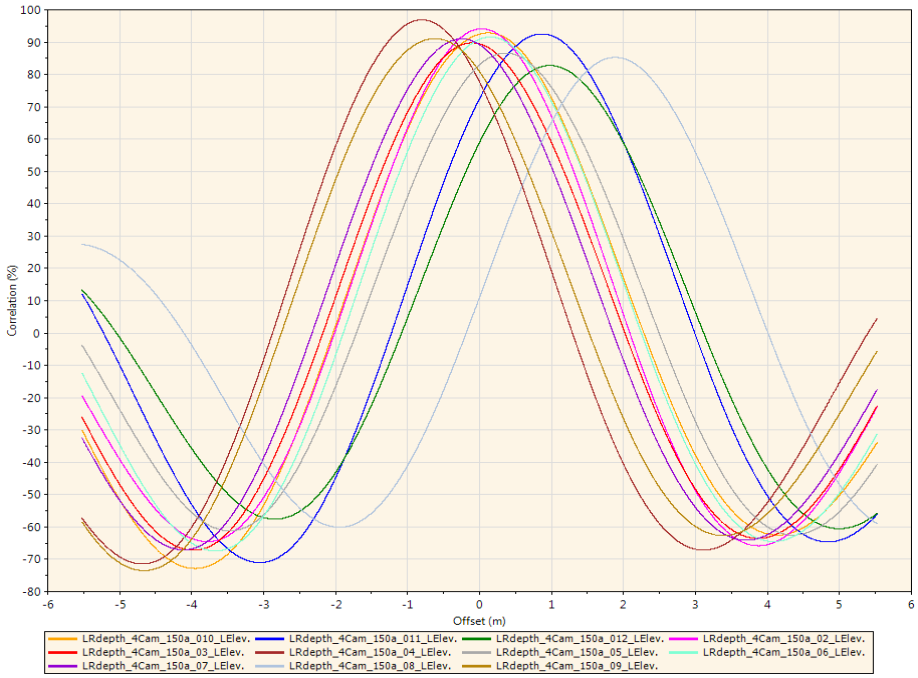

Figure 3.12 The cross correlation results after synchronization

The repeatability test assessment depends on the mean cross correlation coefficient. The test data acquisition system is considered as" certified data collection system" if the mean correlation coefficient is no less than 92%. If the mean correlation coefficient is less than 92%, the test data acquisition system is considered as “unqualified data collection system", from which the collected data are unreliable and unsuitable for the further data processing and analysis.

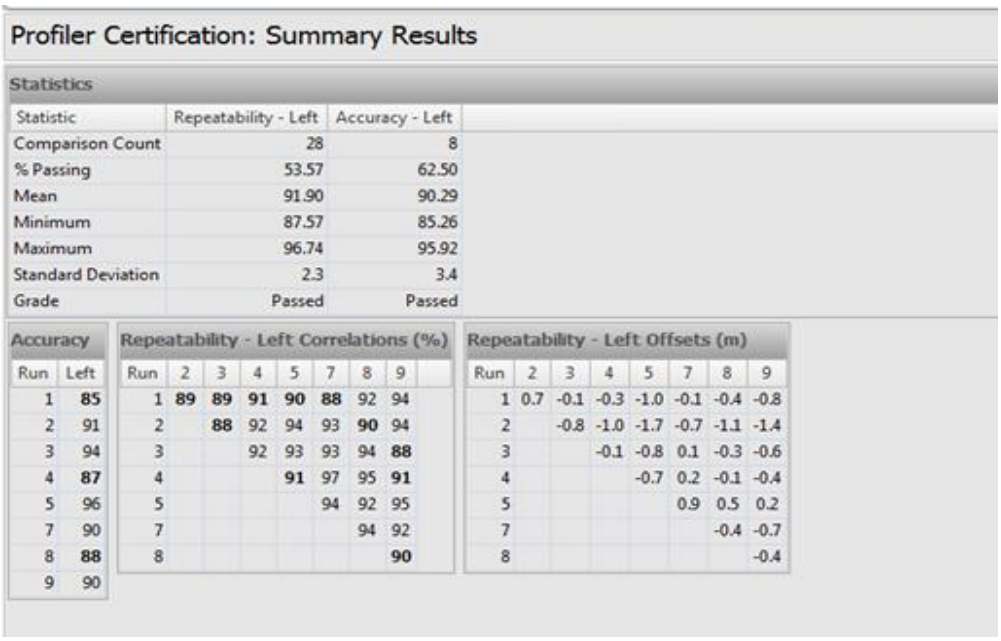

Profiler Certification: Summary Results

Statistics

Statistic	Repeatability - Left	Accuracy - Left
Comparison Count	28	8
% Passing	53.57	62.50
Mean	91.90	90.29
Minimum	87.57	85.26
Maximum	96.74	95.92
Standard Deviation	2.3	3.4
Grade	Passed	Passed

Accuracy

Run	Left
1	**85**
2	91
3	94
4	**87**
5	96
7	90
8	**88**
9	90

Repeatability - Left Correlations (%)

Run	2	3	4	5	7	8	9
1	**89**	**89**	**91**	**90**	**88**	92	94
2		**88**	92	94	93	**90**	94
3			92	93	93	94	**88**
4				**91**	97	95	**91**
5					94	92	95
7						94	92
8							**90**

Repeatability - Left Offsets (m)

Run	2	3	4	5	7	8	9
1	0.7	-0.1	-0.3	-1.0	-0.1	-0.4	-0.8
2		-0.8	-1.0	-1.7	-0.7	-1.1	-1.4
3			-0.1	-0.8	0.1	-0.3	-0.6
4				-0.7	0.2	-0.1	-0.4
5					0.9	0.5	0.2
7						-0.4	-0.7
8							-0.4

Figure 3.13 Summary of repeatability test results

Based on the 3D texture data collected from DHDV system, the data repeatability is investigated and the correlation results are summarized in Figure 3.13. Note that there are 28 groups of comparison results among the basis profiles and comparison profiles. The mean correlation coefficient is 92%, and the repeatability test result is graded as "PASSED", which means the 3D texture data collected from DHDV system are reliable and repeatable, and suitable for the subsequent data processing and analysis.

3.7 Summary

This chapter presents a reliable, repeatable, and comprehensive 3D data acquisition system, DHDV, consisting of several sub-systems and auxiliary systems. The collected data are capable of covering the entire lane (up to 4m wide), and have a variety of potential applications in pavement engineering, including surface distress survey,

transverse and longitudinal profiling, macro-texture measurement, roadway geometry survey, and pavement safety evaluation.

Even though unexpected errors might be produced during data collection, they can be resolved by a series of digital image processing techniques. The zero reference plane based method is proposed to calibrate the elevation difference between two adjacent images and the two sides of an image, and the neighborhood average base method is put forward to repair the invalid readings. Two filters namely ideal band pass filter and Butterworth band pass filter are introduced to eliminate the unwanted information of 3D image data. In addition, the wave number of concern in this study is also determined based on ASTM standard, 3D texture data resolution, and Nyquist sampling theory.

To analyze data of interest, one sampling principle is proposed in this study. Moreover, the repeatability test is also conducted on a chosen pavement section, and results indicate the 1mm 3D texture data acquired from DHDV system are reliable and repeatable.

CHAPTER 4. PAVEMENT FRICTION PREDICTION BASED ON SURFACE TEXTURE INDICATORS

The purpose of pavement texture characterization is to use a series of parameters or indices to describe surface properties so that the surface properties can be quantitatively represented with the proposed parameters. From a pavement engineering point of view, using the proposed parameters to interpret pavement safety properties is more important because the purpose of developing these texture-related parameters is to reveal pavement safety properties (Stout et al, 1993; Schmähling et al, 1996).

4.1 Introduction

In past decades several surface characterization techniques have been proposed for various application purposes, and are generally grouped into two categories: scale-dependent and scale-independent, as shown in Figure 4.1. The scale-independent parameters mean texture characterization results are independent of the measurement scales (data resolution), in which fractal analysis is widely used. The scale-dependent

parameters mean texture characterization results are dependent on the measurement scales, that is, the analysis results might be quite different when different measurement scales are used. The scale-dependent parameters used in this dissertation would be grouped into five categories: amplitude parameters, functional parameters, spectral analysis, spacing parameters, and hybrid parameters (Stout et al, 1993; ASME, 2009).

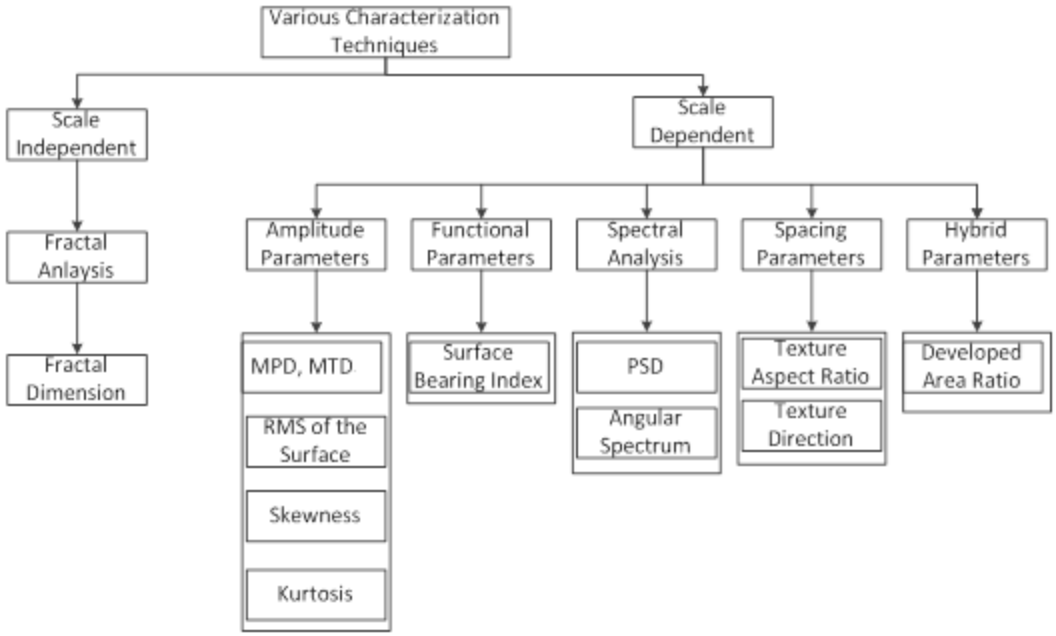

Figure 4.1 Schematic diagram of pavement surface characterization techniques

This chapter mainly presents four scale-dependent parameters namely amplitude parameters, functional parameters, spacing parameters, and hybrid parameters, and their applications to reveal pavement texture properties. To avoid the use of the two highly correlated texture indicators, the relations among these texture indicators are investigated as well. Finally pavement safety property can be evaluated through a mathematical model developed from the proposed texture indicators.

In addition, fractal analysis and spectral analysis would be elaborated in Chapter 5 for the friction prediction based on rubber friction theory.

4.2 Test Specimens

To demonstrate how these texture indicators disclose pavement surface properties, two groups of samples are chosen. The first sample group includes six test specimens, and each specimen is constructed with the different texturing techniques. Figure 4.2a represents rigid pavement with turf dragged texture, followed by are the rigid pavements with randomly transversely tined texture (Figure 4.2b), with longitudinally tined texture (Figure 4.2c), with longitudinally grooved texture (Figure 4.2d), with transversely grooved texture (Figure 4.2e), and with Next Generation Concrete Surface (NGCS) (Figure 4.2f).

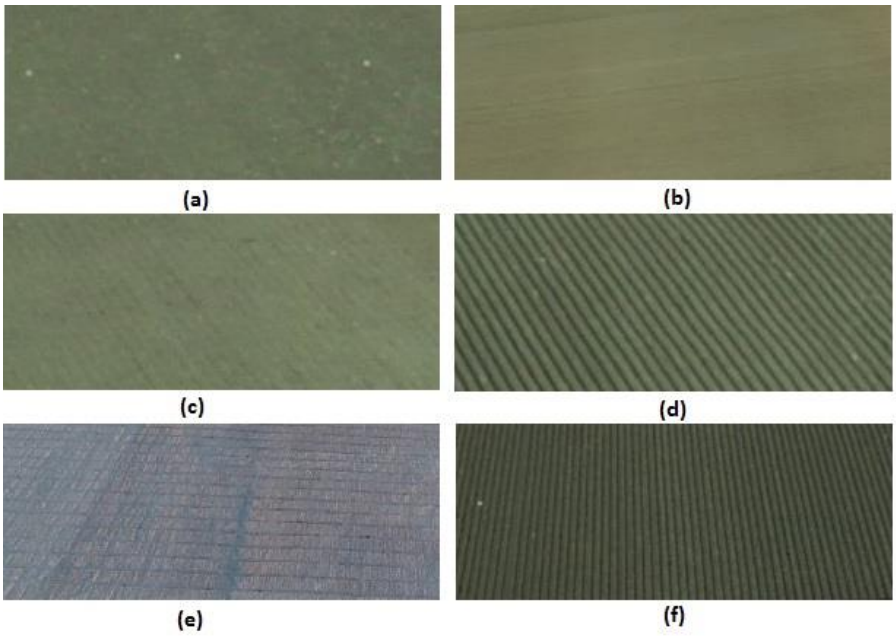

Figure 4.2 Grayscale images of test specimens (a) PCC_DT; (b) PCC_TT ;(c) PCC_LT; (d) PCC_LG; (e) PCC_TG; (f) PCC_NG;

The second sample group contains three test specimens, and each sample is designed with different texture properties. Figure 4.3a represents AC pavement characterized with dense graded surface, followed by are AC pavements that are characterized with exposed aggregate surface (Figure 4.3b), and with high friction treated surface (Figure 4.3c).

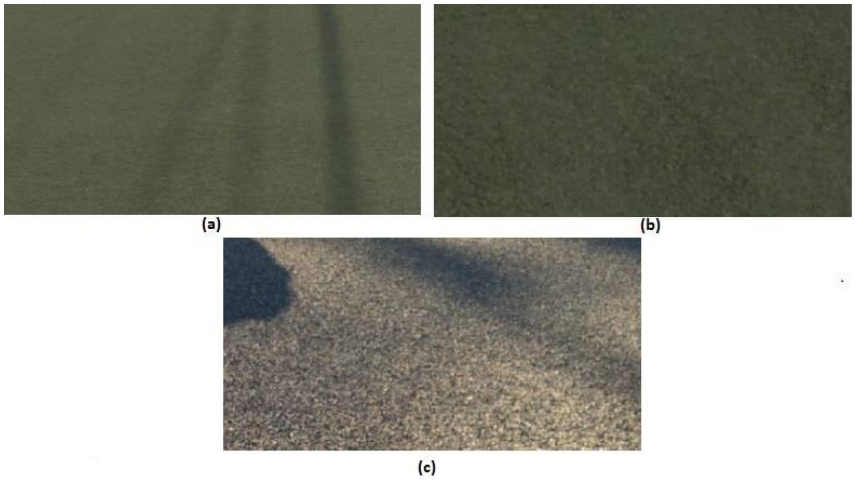

Figure 4.3 Grayscale images of test specimens (a) AC_DG; (b) AC_EA ;(c) AC_HF;

Table 4.1 Description of Surface Texture Properties of Test Specimens

Specimen name	Specimen description
PCC_DT	Turf dragged texture, in good condition, Figure 4.2(a)
PCC_TT	Random transverse tinning, in good condition, Figure 4.2(b)
PCC_LT	Uniform longitudinal tinning, in good condition, Figure 4.2(c)
PCC_LG	Longitudinal groove, in good condition, Figure 4.2(d)
PCC_TG	Transverse groove, newly constructed airport runway, Figure 4.2(e)
PCC_NG	Next Generation Concrete Surface, in good condition, Figure 4.2(f)
AC_DG	Dense graded surface, in good condition, Figure 4.3(a)
AC_EA	Exposed Aggregate surface, in good condition, Figure 4.3(b)
AC_HF	High friction surface, newly constructed, Figure 4.3(c)

The detailed description of these test specimens are given in Table 4.1, in which the notation PCC_DT represents the rigid pavement featured with turf dragged texture. The PCC_TT, PCC_LT, PCC_LG, PCC_TG, and PCC_NG represent PCC pavements characterized with transverse tine, longitudinal tine, longitudinal groove, transverse groove, next generation concrete surface, respectively. The AC_DG represents dense graded pavement surface; the AC_EA represents the exposed aggregate surface; the AC_HF represents the high friction treated surface. For the two data set, each sample has a size of 4096-pixel wide by 2048-pixel high, with a vertical resolution of approximately 0.33 mm. In this study 3D rendering of these two groups of test specimens are provided as well, as shown in Figure 4.4 and Figure 4.5, respectively.

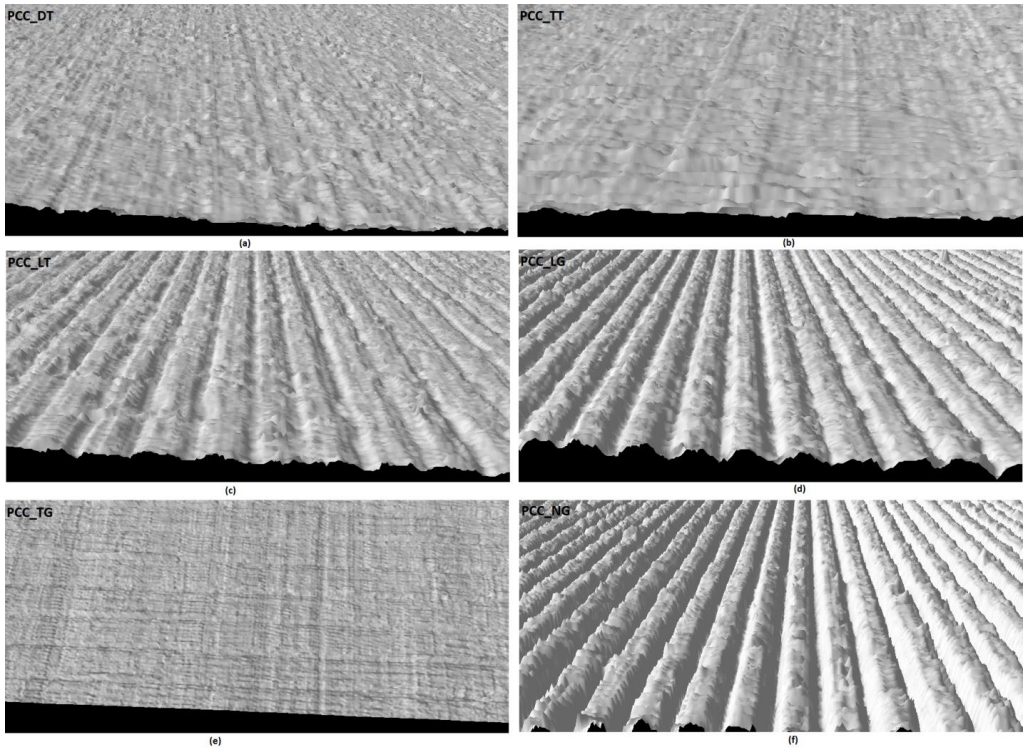

Figure 4.4 3D Rendering of test specimens (a) PCC_DT; (b) PCC_TT;(c) PCC_LT; (d) PCC_LG; (e) PCC_TG; (f) PCC_NG;

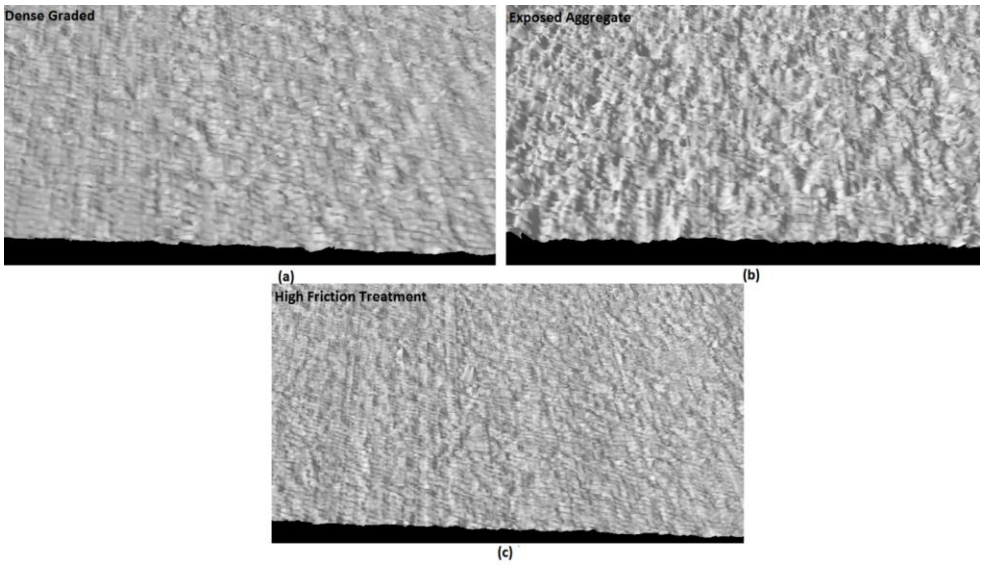

Figure 4.5 3D rendering of test specimens (a) AC_DG; (b) AC_EA ;(c) AC_HF;

Once two groups of test specimens are chosen, the four types of scale-dependent texture characterization techniques can be applied on these specimens. Each category would be elaborated in the following subsections.

4.3 Amplitude or Height Parameters

Amplitude parameter mainly considers the height or elevation information of surface texture such as the average value within a segment or area, the maximum value within a short segment or area, and data elevation distribution. Amplitude parameters ignore impacts of data spacing on texture properties. For amplitude-related parameters, five texture indicators namely MPD, MTD, RMS, Skewness, and Kurtosis are presented. (ASME, 2009; Stout et al, 1993).

4.3.1 Mean Profile Depth (MPD)

MPD is a widely accepted and used texture indicator. It is defined as the average of all mean segment depths of all segments of the profile. According to the MPD computation practice from ASTM E1845 and ISO 13473, the calculation of MPD can be described as follows: the measured profile is divided into different segments which have a length of 100±2 mm, then the segment is divided in two equal halves and the height of the highest peak in each half segment is determined. The average of these two peak heights minus the average of all heights is the mean segment depth. The average value of the mean segment depths for all segments making up the measured profile is reported as the MPD, as illustrated in Figure 4.6.

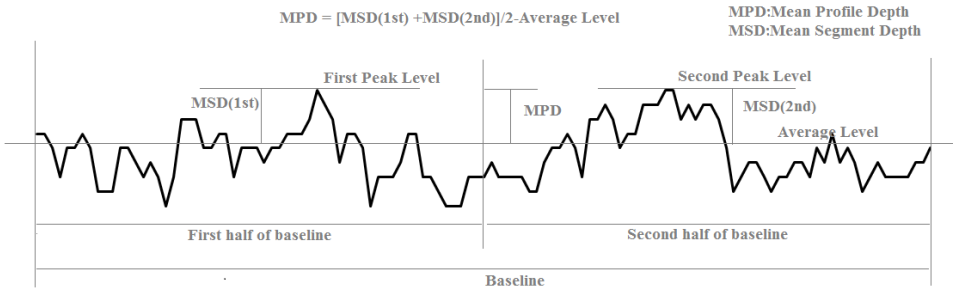

Figure 4.6 A general procedure for MPD calculation

Generally the larger the MPD is; the rougher pavement surface texture is. This parameter is also highly associated with pavement frictional properties. Typically the lager the MPD is, the better the friction performance is. The MPDs at six test specimens in the first group are given in Figure 4.7, from which the fact how the MPD reveals or represents surface texture characteristics is demonstrated.

Note that the turf-dragged concrete surface (PCC_DT) has the lowest MPD, followed by are test sites with the tined concrete surface (PCC_TT and PCC_LT) and grooved concrete surface (PCC_LG, PCC_TG, and PCC_NG). As expected, the next generation concrete surface has the largest MPD since the longitudinal groove has a depth of 11/32 in (8.73mm).

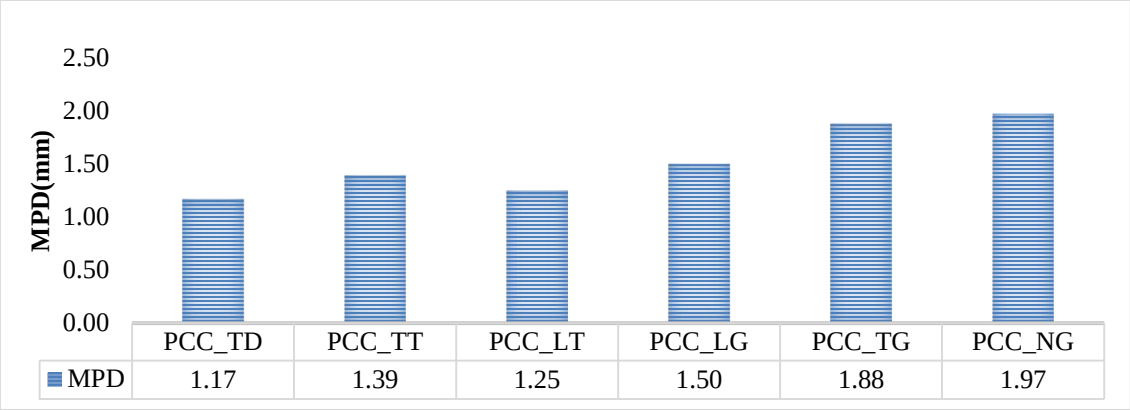

Figure 4.7 Calculated MPDs at these six test sites

The texturing techniques used in these six test specimens are grouped into three categories. The dragged texturing technique produces the narrowest and shallowest surface drainage ditch, resulting in the lowest MPD. The tinning technique produces a wider and deeper surface drainage ditch than these from dragged texturing techniques, resulting in the larger MPDs. The grooving technique produces the widest and deepest surface drainage ditch when compared with the other two texturing techniques, so the largest MPD is produced from the grooving techniques, as shown in Figure 4.7. As a result, the last three test sites may have the better frictional properties than the first three tests sites based on the measured MPDs.

4.3.2 Simulated Mean Texture Depth (SMTD)

MTD can be viewed as a 3D surface characteristic because it is obtained using volumetric measuring technique (ASTM E965). The measured result can be reported as the ground truth. Generally speaking, MTD can be either measured in the field or transformed from MPD. However, in this paper the MTD would be calculated with image techniques in the 3D domain.

A 3D digital image is composed of many discrete height data which is stored in computer as 2D matrix. Assume the sampled data of pavement surface can be divided into several areas; each area has a size of N x M mm, and the SMTD computation can be expressed using Equation (4.1):

$$\mathrm{SMTD} = \frac{\iint_0^{\mathrm{D}} [\mathrm{F}_0 - \mathrm{F}(\mathrm{x},\mathrm{y})]\mathrm{dxdy}}{\mathrm{D}} = \frac{\sum_{x=1}^{N}\sum_{y=1}^{M}[F_0 - F(x,y)]}{\mathrm{D}} \tag{4.1}$$

Where: $\mathrm{F}(\mathrm{x},\mathrm{y})$- the height information at point (x, y), D - the integral area which equals to the M x N pixels, F_0- the height value being equivalent to the maximum peak in each area D (M x N pixels)

The SMTD has the similar texture property with MPD, and is also used to describe pavement friction-related texture properties. The calculated SMTDs at these six test sites are given in Figure 4.8.

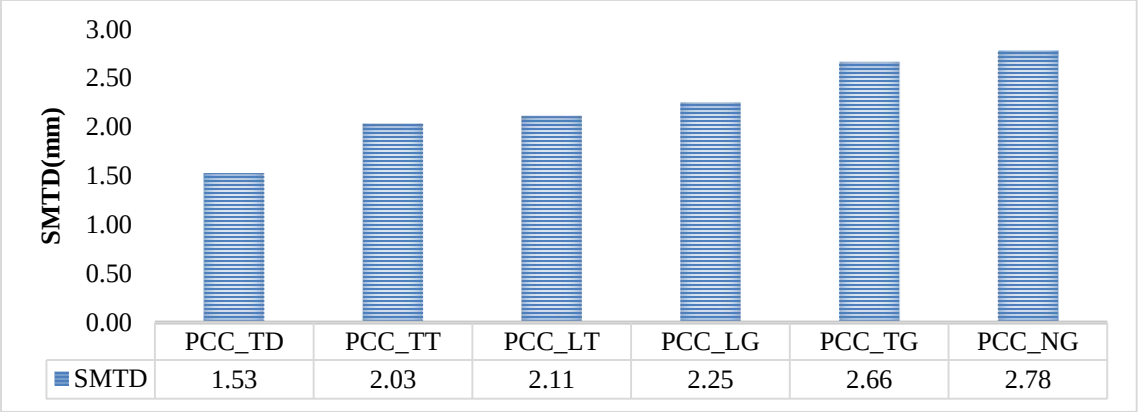

Figure 4.8 Calculated SMTDs at six test sites

As expected, turf-dragged concrete surface (PCC_DT) has the lowest SMTD, followed by are test sites with the tined concrete surface (PCC_TT and PCC_LT) and grooved concrete surface (PCC_LG, PCC_TG, and PCC_NG). The results indicate the last three test sites have the better frictional properties than the first three tests sites based on the calculated SMTDs.

4.3.3 Root Mean Square (RMS) of Surface

RMS is a general measurement of surface texture deviation property, and is affected by texture amplitude within the test sample. If a larger RMS is measured on pavement surface, it indicates there is a significant deviations in surface texture characteristics. Similarly, there is a minor deviations in surface texture characteristics if a less RMS is measured on pavement surface. This parameter can help interpret contact areas between vehicle tires and pavement surface, and is also highly associated with surface bearing capability. The calculation of this parameter can be mathematically described in Equation (4.2):

$$S_q = \sqrt{\iint_0^D [z(x,y)]dxdy} = \frac{\sum_{x=1}^{N}\sum_{y=1}^{M} z(x,y)^2}{M \times N} \quad (4.2)$$

Where: M - the number of points per profile, N - the number of profiles, $z(x,y)$- the deviation value from point (x,y) to average level, S_q - the root mean square of the sample.

The RMSs at PCC test specimens are given in Figure 4.9, from which one can observe that PCC_TG has the largest RMS, indicating the transverse groove may produce the largest pavement friction since the more contact areas between vehicle tires and surface texture are developed. In contrast, the PCC_TD has the least RMS, indicating the dragged texture produce the least pavement friction when compared with the other five test specimens.

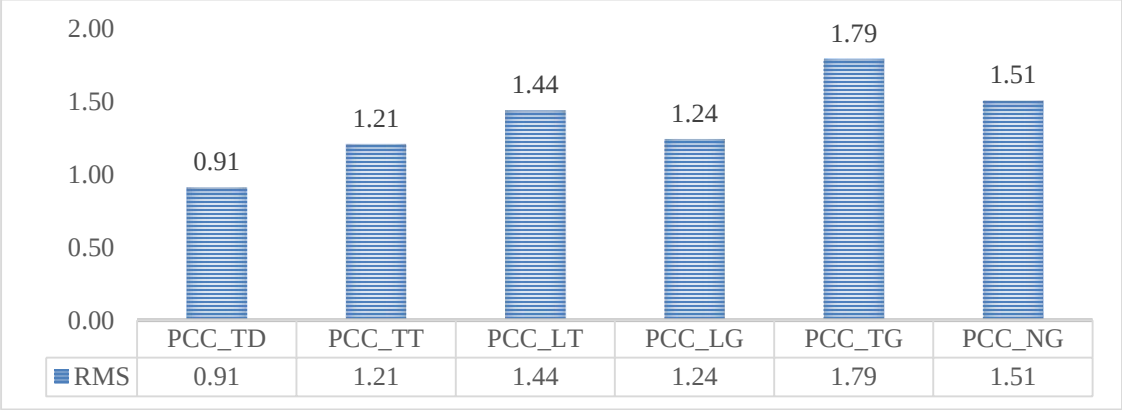

Figure 4.9 Calculated RMS at test specimens

4.3.4 Skewness (Ssk) and Kurtosis (Sku)

Skewness and Kurtosis are used to represent 3D surface texture height distribution properties. Figuratively, a histogram of the heights of all measured points is computed

and the symmetry and deviation from an ideal Normal Distribution is represented by Ssk and Sku, and their mathematical descriptions are given as Equations (4.3) through (4.4):

$$\mathrm{Ssk} = \frac{\iint_0^{\mathrm{D}} [\mathrm{z(x,y)}^3] \mathrm{dxdy}}{\mathrm{S_q^3}} = \frac{\sum_{x=1}^{N} \sum_{y=1}^{M} [z(x,y)^3]}{\mathrm{M} \times \mathrm{N} \times \mathrm{S_q^3}} \tag{4.3}$$

$$\mathrm{Sku} = \frac{\iint_0^{\mathrm{D}} [\mathrm{z(x,y)}^4] \mathrm{dxdy}}{\mathrm{S_q^4}} = \frac{\sum_{x=1}^{N} \sum_{y=1}^{M} [z(x,y)^4]}{\mathrm{M} \times \mathrm{N} \times \mathrm{S_q^4}} \tag{4.4}$$

Where: M - the number of points per profile, N - the number of profiles, $\mathrm{z(x,y)}$ - the deviation value from point $\mathrm{(x,y)}$ to average level, $\mathrm{S_q}$ - root mean square of the surface.

Ssk represents the degree of symmetry surface heights about the mean plane. The sign of Ssk indicates the predominance of peaks (Ssk > 0) or valley structures (Ssk < 0) comprising the surface. Sku indicates the presence of the inordinately high peaks/deep valleys (Sku >3.00) making up the texture. If the surface heights are normally distributed, then Ssk is 0.00 and Sku is 3.00. Similarly, the surface heights are positively skewed if Ssk is larger than 0 and Sku is larger than 3; the surface heights are negatively skewed if Ssk is less than 0 and Sku is larger than 3. Surface height distributions can be considered as the slow varying if the Sku is less than 3, the less the Sku is, the smaller the variation is. In contrast, the surface height distributions can be considered as the extreme peaks or valleys if the Sku is larger than 3, the larger the Sku is, the larger the height variation is, as shown in Figure 4.10.

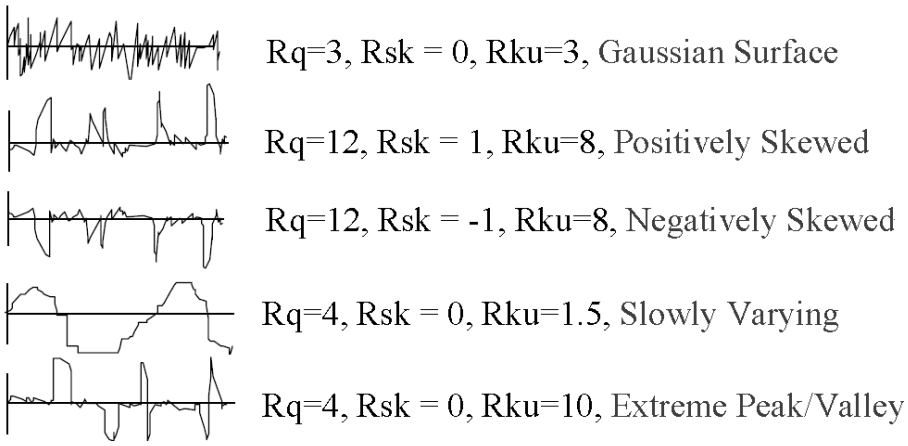

Figure 4.10 Five pavement surface with different Skewness and Kurtosis (ASME, 2009)

Ssk is useful for describing the height distribution of pavement surface topography and monitoring surface wear condition. Sku is useful in measuring the sharpness of the surface height distribution, indicating the presence of peak or valley defects which may occur on the pavement surface.

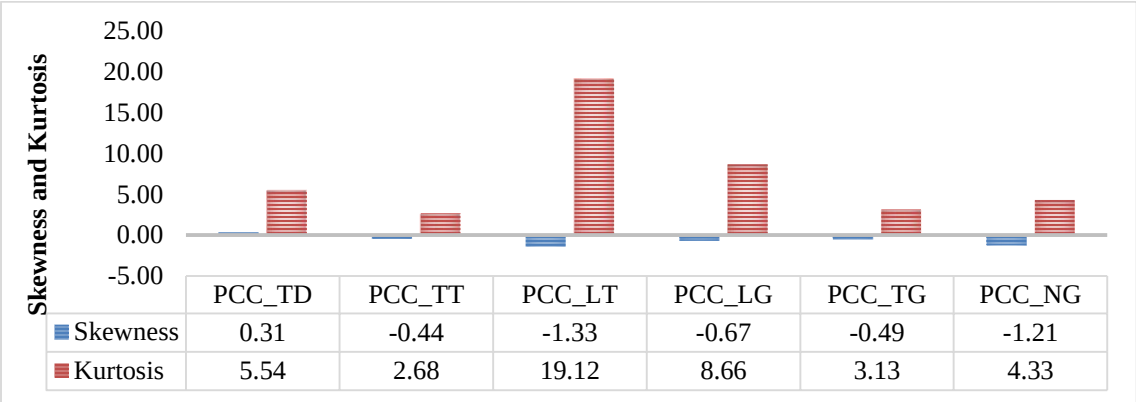

	PCC_TD	PCC_TT	PCC_LT	PCC_LG	PCC_TG	PCC_NG
Skewness	0.31	-0.44	-1.33	-0.67	-0.49	-1.21
Kurtosis	5.54	2.68	19.12	8.66	3.13	4.33

Figure 4.11 Calculated Skewness and Kurtosis at six test sites

Skewness and kurtosis calculated from the group#1 are shown in Figure 4.11. The last five test specimens produce the negative Ssk, entailing surface texture at these test sites are negatively skewed; while the first test specimen produces a positive value, indicating the surface texture at this test site is positively skewed. Kurtosis is used to

disclose the presence of extreme peaks or valleys. In this case the first site has the kurtosis with a value of 5.54, indicating this site has the inordinate peaks, while the third test site has the largest kurtosis, indicating this site has the exceptional valleys.

4.4 Spacing or Spatial Parameters

Amplitude parameters only consider height properties of points within one sample, regardless of the spatial structure properties, so they cannot well describe spatial properties. As a result, spatial or spacing parameters are introduced to reveal the spatial structure properties of pavement surface. Two parameters are included (ASME, 2009).

4.4.1 Texture Aspect Ratio (TAR)

The texture pattern i.e. anisotropic or isotropic texture aspects, can be estimated by the Autocorrelation Function (ACF) which is the most effective and robust approach for texture pattern recognition.

The ACF of the anisotropic pavement surface has the fastest decay along the direction perpendicular to the predominant texture direction and the slowest decay along the texture direction, as shown in Figure 4.12a. In this case the length of fastest decay is dependent on the groove spacing, whist the length of the slowest decay is determined by the sample size.

The ACF of isotropic pavement surface has the similar texture aspects in all direction decays, as shown in Figure 4.12b, in which it is difficult to determine the fastest and slowest decay since it is impossible to normalize the ACF of the fastest and slowest decay to 0.2 which is a threshold to determine the fastest and slowest decay of the test

sample. In this case the lengths of both fastest and slowest decays are assumed as sample lengths or widths.

Figure 4.12 Photographs of (a) highly directional pavement surface (NGCS); (b) highly isotropic pavement surface (HFS)

Texture Aspect Ratio (TAR) is defined to represent the ratio of the length of fastest decay to the length of the slowest decay, and it can be mathematically expressed using Equation (4.5):

$$0 < \mathrm{TAR} = \frac{\text{The distance that the nomalised ACF has the fastest decay to 0.2 in any possible direction}}{\text{The distance that the nomalised ACF has the slowest decay to 0.2 in any possible directiona}} \leq 1 \tag{4.5}$$

In principle, the texture aspect ratio has a value between 0 and 1. Larger values, say TAR>0.5, indicate stronger isotropic or uniform texture aspect in all directions, whereas the smaller values, say TAR <0.3, indicate the stronger periodic texture properties. Since the size of the sampling area is finite, it is possible that the slowest decay of the ACFs of some anisotropic surfaces or the fastest and the slowest decay of the ACFs of isotropic surfaces never reaches 0.2 within the sample area. If this phenomena occurs, the longest distance of the ACF along the slowest decay direction can be used instead. Empirically it does not have a significant influence on the representation of the periodic surface.

The TAR calculation results from these two data groups#1 and #2 are plotted in Figure 4.13. It can be observed that the isotropic features for PCC_DT and AC test specimens are apparent since TAR are greater than 0.5, whereas the other five test specimens in group#1 have the directional texture property since the lower TAR. Note that TAR only determine the isotropic or anisotropic property of surface, and cannot reveal the predominant texture direction. Accordingly the predominant texture direction needs to be further investigated.

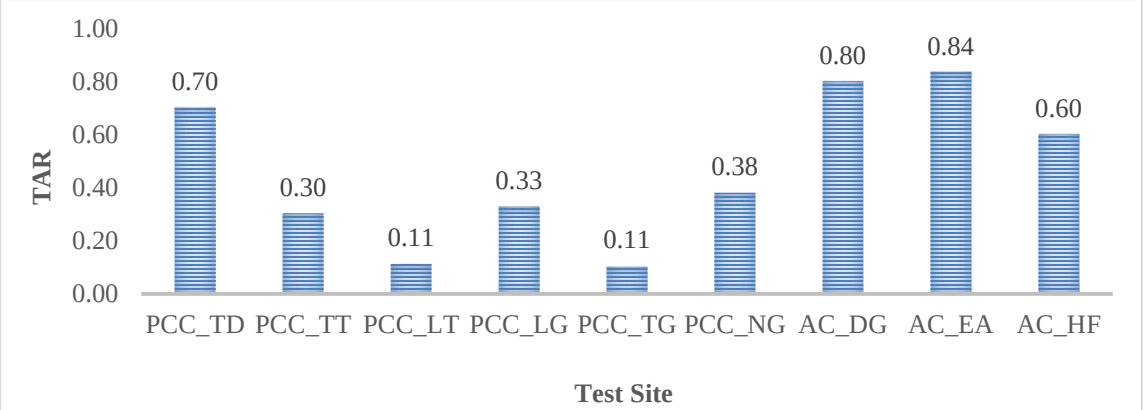

Figure 4.13 TAR at PCC and AC Test Sites

4.4.2 Texture Direction (TD)

This parameter is used to determine the predominant surface texture direction with respect to the y axis, i.e. it gives the lay direction of the surface. Generally this parameter is meaningful only if the TAR is less than 0.5. If the TAR is larger than 0.5, it indicates the surface texture has the isotropic features and has no pronounced texture direction.

The Angular Power Spectral Density (APSD) is used to determine the predominant texture direction. The calculation of APSD needs to consider power spectrum that is conducted in Fourier domain. In Fourier domain, surface texture is represented by a

series of sine waves in all directions with different spatial frequencies and amplitudes, then the power spectrum can be calculated and is a measure of the amplitude of each sine wave for a particular spatial frequency, along a given direction.

For a 3D surface (Figure 4.14a), the power spectrum would be displayed as a "3D" function in which the X and Y axes represent the various spatial frequencies for a given direction. The amplitude of the power spectrum (displayed on the Z axis) represents the amplitude of the sine wave at a particular spatial frequency direction, as shown in Figure 4.14(b). The bright regions of the power spectrum for the transverse surface correspond to higher amplitude sine waves at a given combination of spatial frequencies along the X / Y directions. The single dominant bright lines are thus along a direction perpendicular to the groove patterns of the surface.

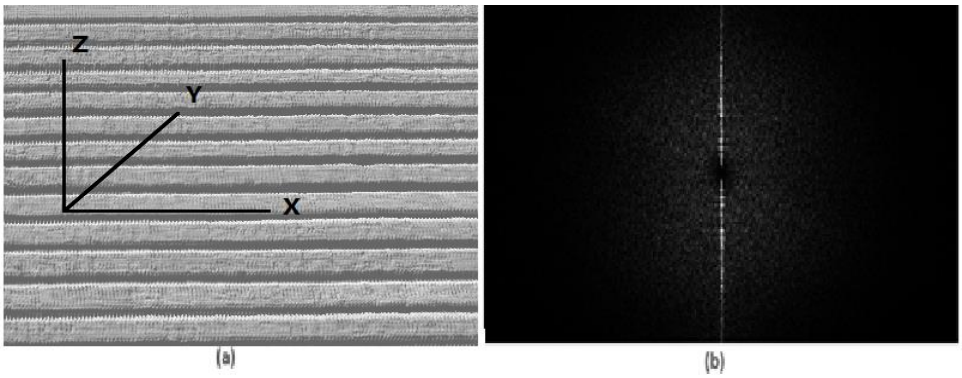

Figure 4.14 Photos of (a) pavement surface with transverse grooves; (b) power spectrum in Fourier domain

The angular power spectrum is found by integrating the amplitudes of each component sine wave as a function of angle, as illustrated in Figure 4.15. The longest hand in the polar spectrum corresponds to the large sine wave amplitudes found along directions perpendicular to the grooves of the surface.

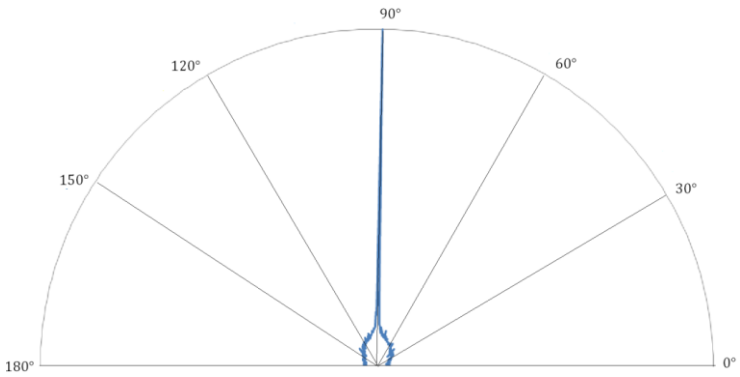

Figure 4.15 Representation of polar spectrum

It is emphasized that the TD itself is meaningfulness except it is used along with TAR. If the TAR is larger than 0.5, the surface texture direction is considered as the isotropic texture properties and the predominant texture direction does not exist. However, if the TAR is less than 0.5, surface texture can be considered as the directional texture property, and the predominant texture direction can be determined with the calculated texture direction.

Table 4.2 Determination of Predominant Texture Direction

Site No	PCC_TD	PCC_TT	PCC_LT	PCC_LG	PCC_TG	PCC_NG	AC_DG	AC_EA	AC_HF
TAR	0.7	0.3	0.11	0.33	0.11	0.38	0.95	0.71	0.58
Isotropic texture	YES						YES	YES	YES
TD		0	89	89	0	89			

In Table 4.2, PCC_TD and the three AC test specimen are characterized with isotropic texture, and thus there is no predominant texture direction. The predominant texture direction for PCC_TT and PCC_TG are is perpendicular to the traveling direction. The PCC_LT, PCC_LG, and PCC_GN have the texture direction parallel to the

traveling direction. In summary, the predominant texture direction can be estimated by the interpretation of these two parameters TAR and TD.

4.5 Hybrid and Functional Parameters

Hybrid parameters are used to overcome some weaknesses of amplitude and spatial parameters. Its calculation depends on both the height and spacing information, and thus any changes that occur in either amplitude or spacing may have an effect on the hybrid property. The functional parameters are highly related to their functions i.e. wearing or friction. In this section one hybrid parameter (surface areal ratio) and one functional parameter (surface bearing index) are presented (ASME, 2009).

4.5.1 Surface Areal Ratio (SAR)

This parameter is computed as: the ratio of the interfacial area of a surface over the sampling area. The areal element can be expressed using the smallest sampling quadrilateral ABCD, as shown in Figure 4.16.

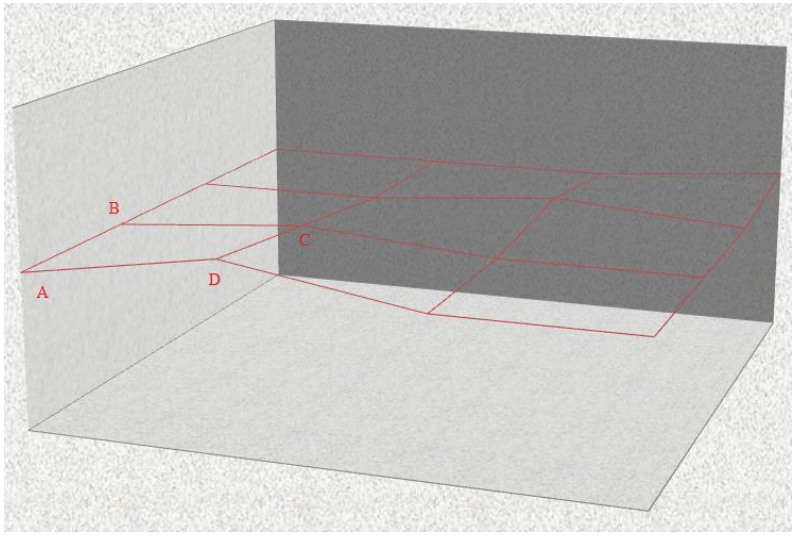

Figure 4.16 Schematic diagram of the interfacial area

Since the four corners of the quadrilateral may not be on the same plane, the interfacial area of the pile-up element may be considered to consist of two triangles, either ABC &ACD or ABD &BCD. The interfacial area of the quadrilateral is defined as an average of two sets of triangle areas (ABC &ACD and ABD&BCD) and its computation principle is given by Equation (4.6):

$$\begin{aligned} A_{ij} = \frac{1}{4}\left(|\overrightarrow{AB}| + |\overrightarrow{CD}|\right)\left(|\overrightarrow{AD}| + |\overrightarrow{BC}|\right) \\ = \frac{1}{4}\left\{\left(\left[\Delta y^2 + \left(f(x_i, y_j) - f(x_i, y_{j+1})\right)^2\right]^{\frac{1}{2}}\right. \\ + \left[\Delta y^2 + \left(f(x_{i+1}, y_{j+1}) - f(x_{i+1}, y_{j+1})\right)^2\right]^{\frac{1}{2}} \\ + \left[\Delta x^2 + \left(f(x_i, y_j) - f(x_{i+1}, y_j)\right)^2\right]^{\frac{1}{2}} \\ \left. + \left[\Delta x^2 + \left(f(x_i, y_{j+1}) - f(x_{i+1}, y_{j+1})\right)^2\right]^{\frac{1}{2}}\right)\Bigg\} \end{aligned} \tag{4.6}$$

The total interfacial area on the surface can be computed using Equation (4.7):

$$A = \sum_{j=1}^{N-1}\sum_{i=1}^{M-1} A_{ij} \tag{4.7}$$

Then the calculation of surface areal ratio is given as Equation (4.8):

$$SAR = \frac{(A - (M-1)(N-1) \times \Delta x \times \Delta y)}{(M-1)(N-1) \times \Delta x \times \Delta y} \tag{4.8}$$

The developed interfacial area ratio reveals the hybrid property of surfaces. A large value indicates the significance of either the amplitude or the spacing or both. As shown in Figure 4.17, the PCC _TD has the smallest SAR, followed by is the AC_DG, which indicate the data amplitude or spacing are less significant compared to other test specimens. It also can be considered that texture properties at these two sections are not

as complex as other test sections, indicating the lower pavement friction may exist at these two sections.

Results also indicate PCC_TG has the largest SAR, followed by is the AC_HF, which indicate the texture properties at these two test specimens are more complex than other test specimens. However, these parameters are invalid to disclose the texture properties for longitudinal groove or tines (e.g. PCC_LT, PCC_LG, and PCC_NG) due to the limit of algorithm itself.

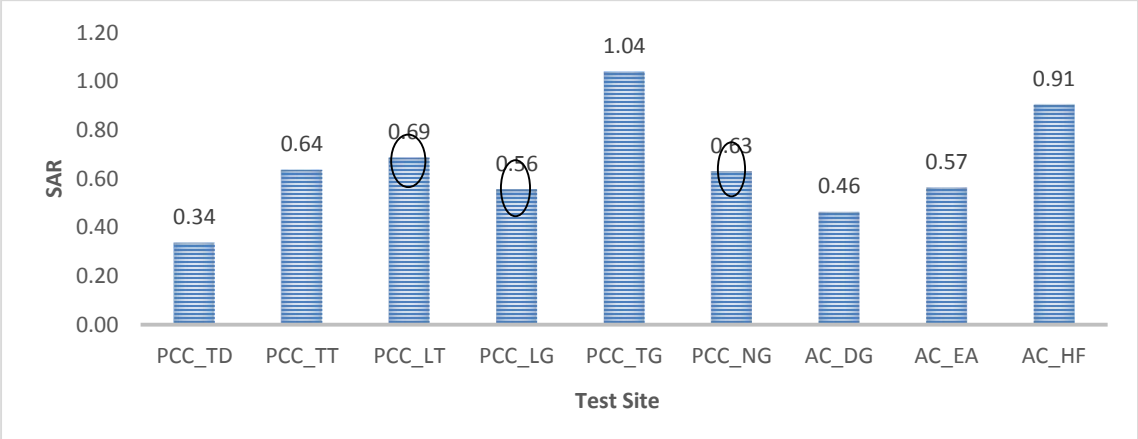

Figure 4.17 SAR at PCC and AC test sites

4.5.2 Surface Bearing Index (SBI)

This parameter may have a very close relation with the wearing functional properties of the surface, and is the ratio of the root mean square to the surface height at 5% bearing area, as given in Equation (4.9).

$$SBI = \frac{\sqrt{\iint_0^D [z(x,y)]dxdy}}{H_{5\%}} = \sqrt{\frac{\sum_{x=1}^{N}\sum_{y=1}^{M} z(x,y)^2}{M \times N}} / H_{5\%} \quad (4.9)$$

Where M - the number of points per profile, N - the number of profiles, $z(x, y)$ - the deviation value from point (x, y) to average level; $H_{5\%}$ - the surface height at 5% bearing area.

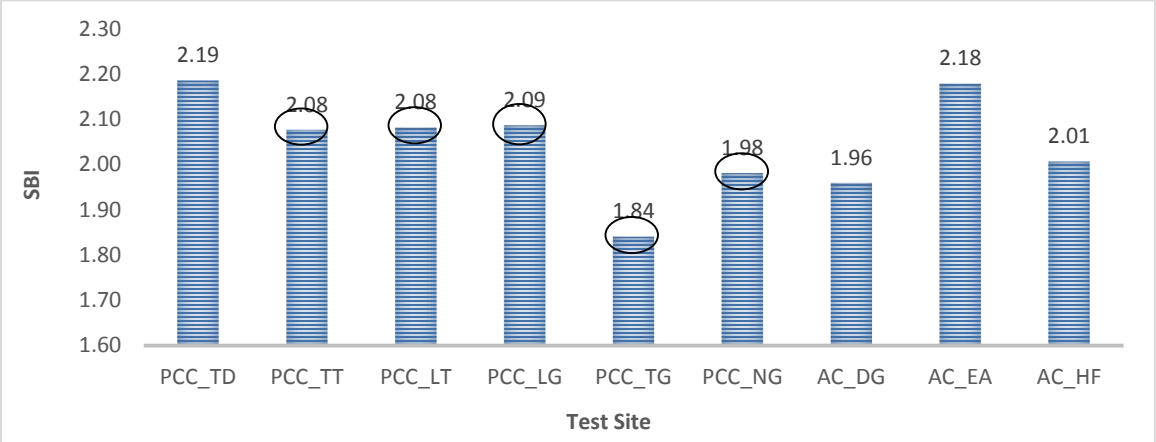

Figure 4.18 SBI at PCC and AC test sites

A large surface bearing index indicates a good bearing property. For AC specimens, the AC_EA has the largest bearing capacity, followed by is the AC_HF and AC_DG, as shown in Figure 4.18. In addition, the index is invalid for PCC pavements with grooving or tinning texture due to the limit of algorithm itself. These invalid readings are marked by a circle.

4.6 Correlations among Texture Indicators

Firstly MPD is considered as the basis texture indicator since it is widely accepted and used in pavement surveys. The relationships between MPD and other texture indicators (comparison texture indicators) are investigated based on the nine test samples (6 PCC test samples and 3 AC samples). Secondly RMS is taken as a basis texture indicator to correlate with the remaining texture indicators exclusive of MPD and those that have

good correlations with MPD. Thirdly correlations between Skewness and Kurtosis, between Skewness and SAR are investigated. Finally the relations between Kurtosis and SAR are examined.

If the two texture indicators have a good correlation (R-squared ≥ 0.8), one of them can be ignored since they reveals the similar texture properties. That is, there is no need to keep two texture indicators that have the good correlations since they only reflect one aspect of pavement surface properties. However, for two texture indicators that have the poor correlation (R-squared ≤ 0.6), they can be considered to reveal two different texture properties, so the two texture indicators should be kept for different application purposes.

4.6.1 MPD versus Comparison Texture Indicators

Figure 4.19 shows there are no good correlations between MPD and the comparison texture indicators, with one exception of the correlation of MPD and SMTD. The texture properties revealed by SMTD can also be represented by MTD, and thus only one of them needs be retained to represent surface texture properties. In this study the MPD is used.

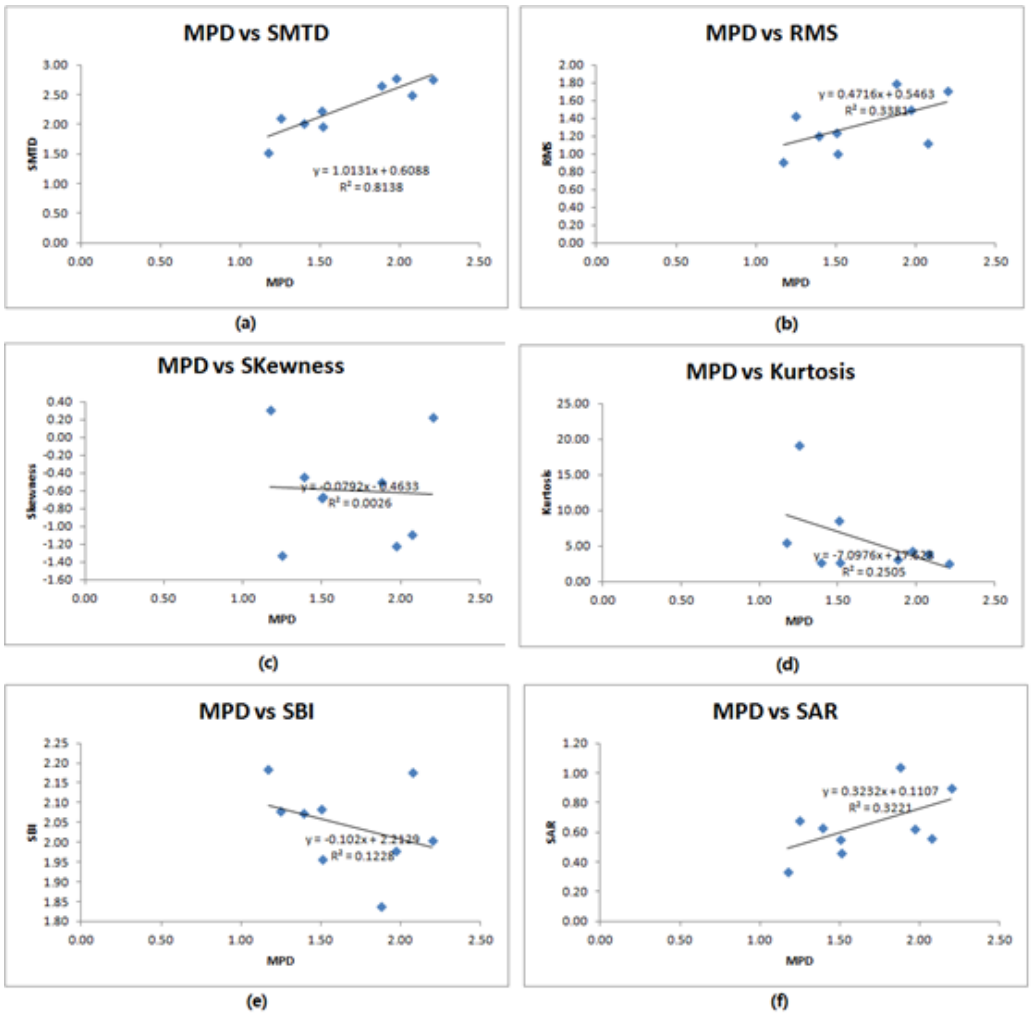

Figure 4.19 Correlation results (a) MPD Vs SMTD; (b) MPD Vs MRS; (c) MPD Vs Skewness; (d) MPD Vs Kurtosis; (e) MPD Vs SBI; (f) MPD Vs SAR

4.6.2 RMS versus Remaining Texture Indicators

RMS is considered as the basis texture indicator to correlate with the remaining texture indicators including Skewness, Kurtosis, SBI, and SAR. As Figure 4.20 shows, a good correlation is observed between RMS and SAR, with an R-squared value of 0.9, indicating one of them should be kept to disclose surface texture properties. However, coefficients of correlations between RMS and other texture indicators are not high

enough to establish a model to predict each other. In this case SAR is kept to describe the hybrid property of surface texture. In addition, the potential contact areas between tires and surface texture can also be interpreted with the value of SAR.

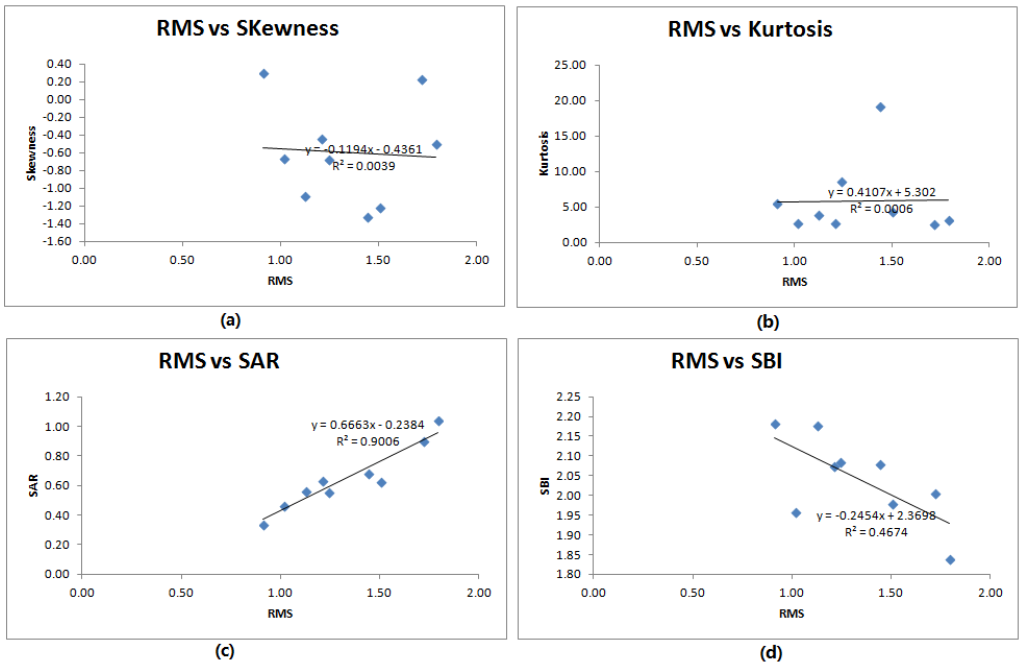

Figure 4.20 Correlations results (a) RMS Vs Skewness; (b) RMS Vs Kurtosis; (c) RMS Vs SAR; (d) RMS Vs SBI

4.6.3 Skewness versus Kurtosis and SBI

Skewness is considered as the basis texture indicator. Kurtosis and SBI are taken as the comparison texture indicators. The correlation results indicate there are no good agreements between Skewness and Kurtosis or SBI. Both of them should be kept to disclose surface texture properties, as shown in Figure 4.21.

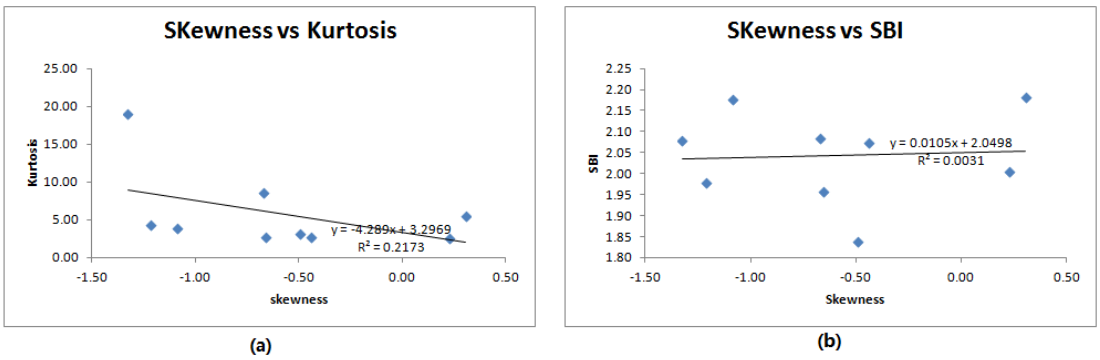

Figure 4.21 Correlation results (a) Skewness VS Kurtosis; (b) Skewness Vs SBI

4.6.4 Kurtosis versus SBI

Figure 4.22 shows there is a poor correlation between kurtosis and SBI, with an R-squared of 0.07, indicating Kurtosis and SBI are two independent parameters, and they cannot estimate each other through an acceptable model. Therefore both of them should be kept to describe surface texture properties.

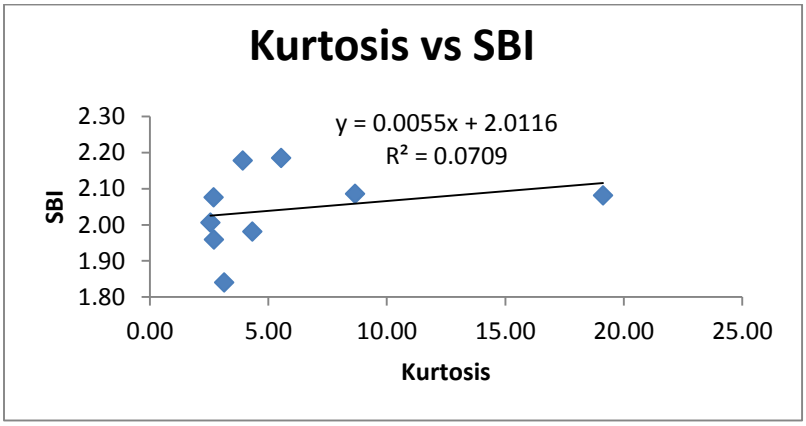

Figure 4.22 Correlation result between Kurtosis and SBI

Based on correlation results from subsections 4.6.1 to 4.6.4, it is found that MPD, Skewness, Kurtosis, TAR, texture direction, SAR, and SBI are capable of disclosing

different aspects of surface texture properties. As a result, the surface texture characterization can be conducted with these seven texture indicators.

4.7 Case Study

To examine the quantitative relationships between the seven surface texture indicators and pavement friction, one pavement section is chosen as the test bed in this study.

4.7.1 Route Description

AL-I 65 data collection starts at GPS coordinate of 32.387859, -86.322212, and ends at GPS coordinate of 32.390949, -86.321396, with a total length of approximately 1290 feet. The data collection site is the ramp from NB I-65 to EB SH152 (Northern Blvd.), as shown in Figure 4.23.

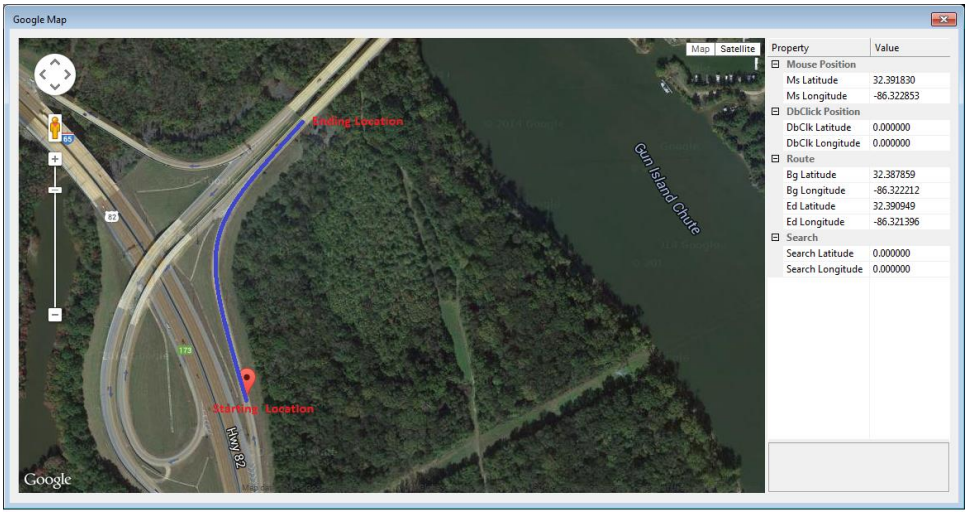

Figure 4.23 AL-I 65 field test site

The route consists of two surface types: High Friction Surface Treatment (HFST) and the regular AC pavement surface type. HFST is located in the middle of the test section. The regular surface is located at the lead-in and lead-out segments. For friction

measurements, the HFST has a length of approximately 675ft, and regular surface has a lead-in and lead-out of lengths of 314ft and 275ft, respectively. Also, a 324ft lead-in and 282ft lead-out are used in 3D data collection, as described in Table 4.3.

Table 4.3 Summary of AL I65-R-N Data Length (Ft)

	Friction Data (Ft)	3D Data (Ft)
lead in	314	324
lead out	275	282
Section length	675	688
total length	1264	1294

4.7.2 Friction Field Measurement

The test section can be sampled into 83 segments with each segment having a length of 15ft based on the total section length of 1264ft. The HFST segment starts with the location of approximately 300ft and ends with the location of approximately 1000ft, as marked in Figure 4.24.

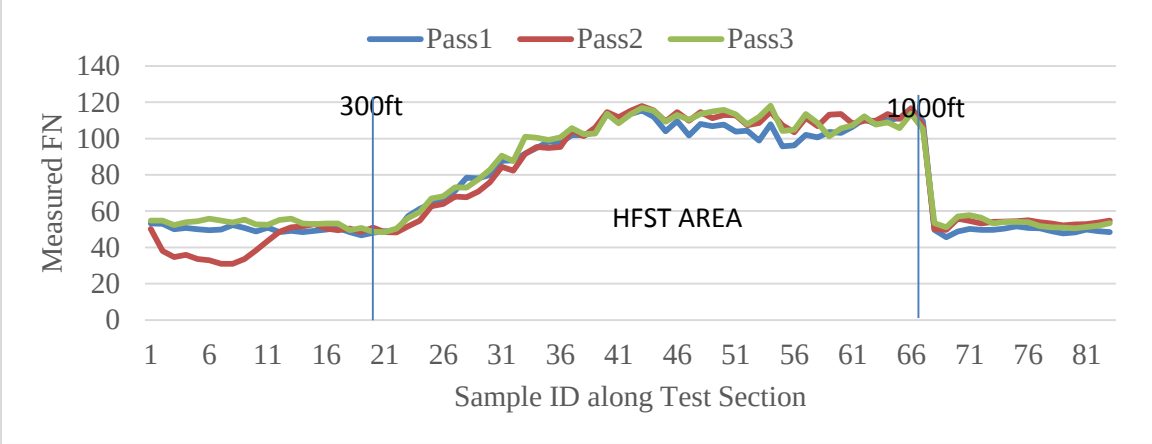

Figure 4.24 Friction measurement results on AL I 65 ramp

To validate the reliability of the collected friction data, three repetitive measurements are conducted on the test route. Note that the excellent agreements exist for the three

measurements, with the correlation coefficients of 0.95, 0.98, and 0.95, respectively. In this study the average FNs from the three measurements are served as the basis for the comparison and validation with predicted friction.

4.7.3 Pavement Friction Prediction

As presented in Section 4.6, pavement friction can be interpreted from the seven texture indicators, namely MPD or MTD, Skewness, Kurtosis, TAR, texture direction, SAR, and SBI. If the chosen test section is the flexible pavements, the indicator of texture direction can be ignored since pavement surface has isotropic properties. Therefore in this study six texture indicators are used to examine their relationships with pavement friction based on the multivariate regression analysis.

Figure 4.25 shows the predicted FNs are compared with the measured FNs, with an R-squared value of 0.76. Note that a good agreement appears at the lead-in and HFST segments, but a large difference exist at the lead-out segment, as illustrated in Figure 4.26.

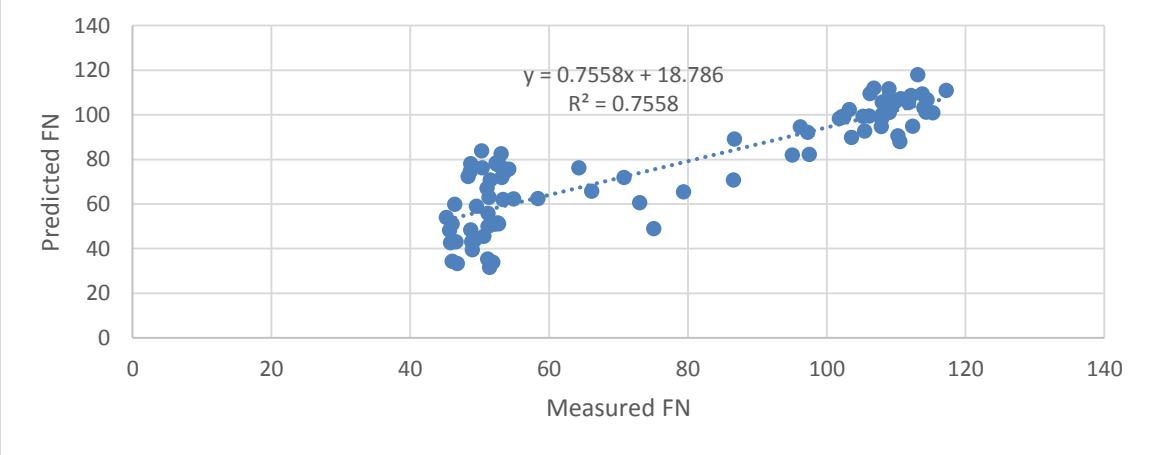

Figure 4.25 Correlation results between the predicted and measured FNs

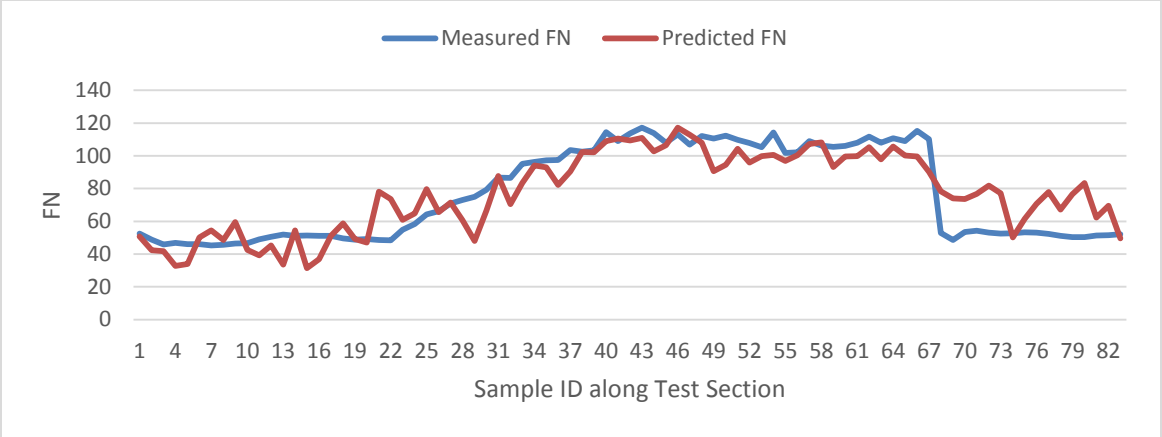

Figure 4.26 Comparison of the measured and predicted FNs from six texture indicators

Based on the multivariate regression analysis, the pavement friction (FN_p) can be predicted with the six texture indicators, as described in Equation 4.10.

$$FN_p = 4.79 \times MTD + 10.72 \times Skewness - 0.26 \times Kurtosis + 12.70 \times TAR - 189.00 \times SAR + 63.09 \times SBI - 32.19 \quad (4.10)$$

However, the sensitivity analyses of the predicted FNs to the six texture indicators indicate MTD, Kurtosis, and SAR have no significant influences on the predicted FNs based on the p-values, as shown in Table 4.4. Accordingly the pavement friction enables to be estimated using the three indicators: Skewness, TAR, and SBI.

Table 4.4 Multivariate Regression Results from the Six Texture Indicators

	Coefficients	t Stat	P-value	Standard Error
Intercept	-32.1885	-0.59366	0.554504	54.22064
MTD	4.789981	0.185045	0.853686	25.88546
Skewness	10.72162	4.390227	3.61E-05	2.442156
Kurtosis	-0.26334	-0.05564	0.955777	4.733085
TAR	12.69876	1.718354	0.089804	7.390068
SAR	-188.999	-0.92695	0.356887	203.8937
SBI	63.08713	7.889286	1.79E-11	7.996558

The multivariate regression analysis method is used to predict pavement friction based on three variables: Skewness, TAR, and SBI. The correlation coefficients between the predicted and measured FNs are 0.75, and the model coefficients are shown in Table 4.5. In this case the pavement friction prediction model can be mathematically described using Equation 4.11.

$$\mathrm{FN}_p = 10.99 \times \mathrm{Skewness} + 16.64 \times \mathrm{TAR} + 68.47 \times \mathrm{SBI} - 72.14 \tag{4.11}$$

Table 4.5 Multivariate Regression Results from Skewness, TAR, and SBI

	Coefficients	t Stat	P-value	Standard Error
Intercept	-72.14128984	-6.03162	4.93698E-08	11.96051074
Skewness	10.98630889	6.612863	4.06772E-09	1.661354481
TAR	16.63509172	2.455651	0.016258354	6.774208625
SBI	68.46577544	12.88464	4.1399E-21	5.313750807

As a result, pavement friction can be estimated based on the three texture indicators: Skewness, TAR, and SBI. Skewness is a representation of surface height distribution, belonging to the amplitude parameters. TAR is one of spacing parameters, describing the pavement surface texture types. SBI is a functional parameter, highly associated with surface bearing capacity and pavement frictional properties.

4.8 Summary

This chapter presents four 3D surface texture characterization techniques namely amplitude parameters, spacing parameters, hybrid parameters, and functional parameters. For amplitude parameters, five texture indicators are introduced. MPD is commonly accepted and used. MTD are highly correlated with MPD, and thus one of them is necessary to be kept to reveal the height property. RMS is highly correlated with the

hybrid parameter (surface areal ratio), so it can be ignored as well if the hybrid parameter is used to reveal surface texture property. In addition, the Skewness and Kurtosis are also used to describe the height distributions of the surface texture. Skewness is useful in determining the predominance of peaks (Ssk>0) or valleys (Ssk <0), and kurtosis is used to determine the presence of extremely peaks or dips (Rku >3).

For spacing parameters, two parameters are firstly applied in pavement engineering to reveal texture properties. Texture aspect ratio is useful in determining texture patterns: isotropic and anisotropic. Texture direction is used to determine the predominant texture orientation. In addition, hybrid parameter and functional parameters are also applied in pavement surface characterization. Surface areal ratio is to represent the hybrid property of amplitude and spacing of pavement surface. Surface bearing index attempts to represent the surface bearing capacity that are highly associated with pavement frictional properties.

The relationships among these texture indicators are investigated as well. For the two texture indicators having a good correlation, one of them can be kept since both of them reveal the similar surface texture properties. Based on this principle, in this study there are seven texture indicators available to represent surface texture characteristics, namely MPD, Skewness, Kurtosis, texture aspect ratio, texture direction, surface areal ratio, and surface bearing index.

To examine the quantitative relationships between texture indicators and pavement friction, one mathematical model is developed to predict pavement friction based on amplitude, spacing, and functional parameters.

CHAPTER 5. PAVEMENT FRICTION PREDICTION BASED ON RUBBER FRICTION THEORY

Chapter 4 primarily presents pavement friction prediction based on surface texture indicators, and a mathematical model is developed based on field test data. Aside from the work done in this study, much other work have been made to predict pavement friction from texture measurements using experimental methods as well (Leu et al, 1978; Do et al 2004; Ergu et al, 2005; Kebrle et al, 2007), with limited successes. Note that the accuracy of predicative models relies on a multitude of factors such as tire inflation pressure, temperature, rubber wear or aging, sliding velocity, vertical load, pavement texture property, and even road evenness and curviness (Klüppel et al, 2000). Therefore, developing a reliable model for the accurate prediction of pavement friction is still a challenge for researchers.

Recently two physical friction theories are developed to investigate rubber friction and contact mechanics (Klüppel et al, 2000; Persson, 2001). The common key feature of

these two theories is that they have a physical basis and predict the frictional coefficient of rubber materials sliding on a rough surface based on fundamental input parameters such as a basic viscoelastic property of the rubber. The friction force is calculated from the dissipated energy during sliding. Studies indicate the predicted friction coefficients from the two theory models match well with the experimental results (Westermann, 2004). In this study, one of these two theories, Klüppel/Heinrich model is used to predict pavement friction based on the 3D texture data.

5.1 Rubber Friction Theory by Heinrich/Klüppel

In Heinrich/Klüppel model, the roughness of self-affine surface or AC pavement surface is described with three texture descriptors, namely the Hurst-Exponent (related to fractal dimension) and the other two correlation lengths parallel and perpendicular to the surface profile (related to the height difference correlation). Accordingly the calculation of these roughness descriptors involves in the fractal dimension analysis and height difference correlations.

Heinrich/Klüppel friction theory describes the elastic contact between tire rubbers and pavement texture asperities using Greenwood-Williamson model (Greenwood, 1966; Klüppel et al, 2000). To predict pavement friction, three parameters (i.e. tire penetration depth, loss modulus, and power spectral density) need to be determined based on tire properties, normal pressure, surface roughness and complex viscoelastic modulus. Typically the calculation of tire penetration depth depends on storage modulus at an excitation frequency and the correlation length parallel to pavement surface. The loss modulus is determined by relaxation time of Zener slider model, sliding velocity, and

surface texture wavelengths. The power spectral density is derived from the Fourier Transform.

The basic idea for the determination of the hysteresis friction coefficients is to calculate the dissipated energy (E_d) during sliding on a rough surface. The loss energy can be mathematically described in Equation (5.1):

$$E_d = \int_0^V \int_0^T \sigma(x, z, t)\dot{\epsilon}(x, z, t)d^2xdt \tag{5.1}$$

Where V represents the volume derived from tire deformation; T represents the time to complete rubber sliding on test segment; $\sigma(x, z, t)$ represents the normal pressure over the time t; $\dot{\epsilon}(x, z, t)$ represents the strain over time t.

Per energy conservation rules, the energy dissipation per unit time must equal to the product of friction force (related to hysteretic energy loss) and the sliding velocity, then one obtains Equation (5.2):

$$\mu_{HK} = \frac{\langle z_p \rangle}{8\pi^2 \sigma_0 v} \int_{w_{min}}^{w_{max}} wE^{||}(w)PSD(w)dw \tag{5.2}$$

Where μ_{HK} represents the hysteresis friction coefficient for a cylindrical rubber block undergoing a one-dimensional deformation during sliding contact at velocity v with a rough surface under contact pressure σ_0; $\langle z_p \rangle$ is the tire penetration depth whose calculation is related to fractal dimension and height difference correlation; $E^{||}(w)$ is the loss energy modulus and determined by Zener slider model; PSD(w) is the energy amplitude at the given angular frequency w and can be determined by the Fourier Transform.

To intuitively describe the implementation of Heinrich/Klüppel model, its working principles are schematically illustrated in Figure 5.1. To better understand texture roughness descriptors and other parameters used in this model, the fractal dimension analysis, height difference correlation method, Zener slider model and the calculation of tire penetration depth, and power spectral density estimation are elaborated in this chapter.

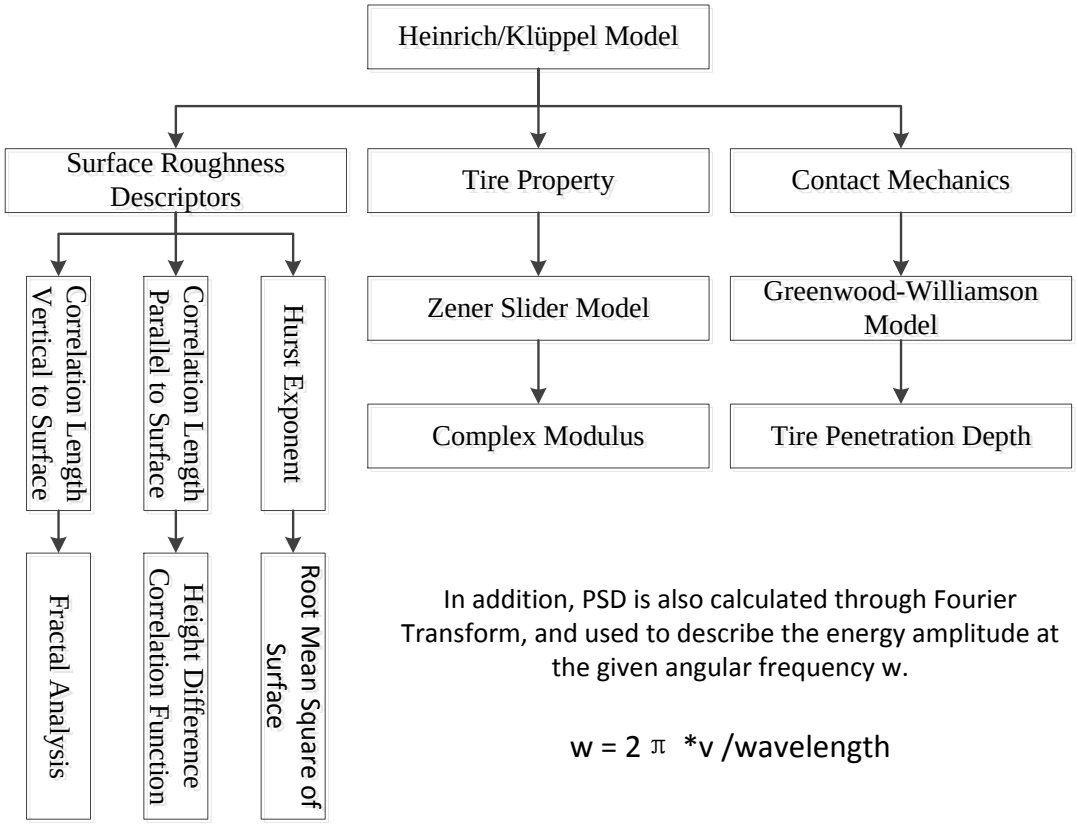

Figure 5.1 Fundamental framework of Heinrich/Klüppel model

5.2 Fractal Dimension (FD) Analysis

The self-affine behavior is observed in the pavement texture structure or shape, leading to a natural way to describe the surface texture under various length scales (Kokkalis,et

al ,1998), as shown in Figure 5.2. Currently fractal concepts have already been successfully used in pavements or relative subjects. For instance, the use of fractals for characterizing aggregate shapes is reported (Carr et al, 1990); the fractal number represents the angularity of the particles (Li et al, 1990); the fractal concepts are also used to determine the surface area of aggregate particles (Carr et al, 1992); the fractal dimensions can be used to simulate the relationship of the surface wetting, wear and skid resistance (Kokkalis, et al, 1998).

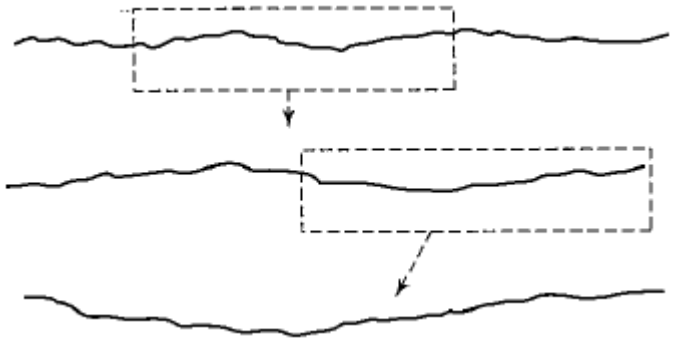

Figure 5.2 Self –Similarity illustrated on a simulated profile (ASME, 2009)

In this paper fractal dimension analysis would be utilized to characterize the properties of 3D surface texture obtained from DHDV with PaveVision3D Ultra, and the resultant fractal dimension is used to calculate one of the three roughness descriptors: Hurst exponent (H).

5.2.1 Methodologies

Although an increasing number of papers provide a theoretical basis for observing fractal behavior in past decades (Bartlett, 1991; Mather et al, 2009), the selection of a method which can provide a consistent and reliable determination of the fractal dimension

remains unsolved. Many methods, such as box counting, walking divider method, power spectrum and so on, have been developed, but most have their practical and theoretical limitations. In this paper both walking divider and box counting method are used to determine the fractal dimension of pavement profile.

5.2.1.1 Walking Divider Method

This method uses a chord length (Step) and measures the number of chord lengths (Length) required to cover a fractal curve (Vallejo, 2001). The technique is based on the principle of taking rulers of varying size (Step) to cover the curve and counting the number of rulers (Length) required in each case, as illustrated in Figure 5.3.

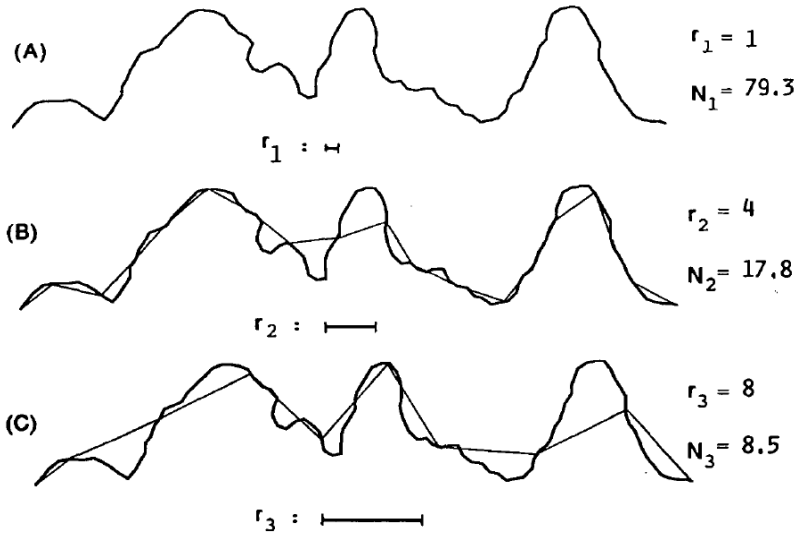

Figure 5.3 The measured profile lengths with various segment length(r), and number of segments (N) (Vallejo, 2001)

Since the profile resolution collected using DHDV is around 1 mm, the fractal behavior cannot be measured at a smaller observation scale. That is, one cannot use ruler with a step length less than 1mm to measure the complexity of profiles. However, the

high resolution (less than 1mm) is necessary to investigate the complexity of profiles using step length based method.

To make the walking divider method have a step length less than 1mm, the interpolation method is used to improve sample resolution by interpolating nine pixel values between each two adjacent pixels. For example, the two adjacent pixel values (P_s and P_{s+1}) are applied to estimate the slope between the two points. Upon obtaining the slope, the nine interpolation values between P_s and P_{s+1} can be calculated using Equation (5.3).

$$\mathrm{InH(i)} = \mathrm{Ps} + \mathrm{Slope} * 0.1 * \mathrm{i};\ \ \mathrm{i} \in 1 \text{ to } 9 \qquad (5.3)$$

Where: $\mathrm{InH(i)}$ is the estimated pixel values at the interpolated pixel number i; Ps represents the first pixel value of these two adjacent pixels; Slope is determined by the two adjacent pixels; 0.1 is the resolution of the newly improved profile.

Fractal Dimension (FD) equals to the ratio of the log of the number of linear elements N with respect to the log of the reciprocal of the linear scaling ratio (r). Its mathematical description is given in Equation (5.4).

$$\mathrm{FD} = \frac{\log \mathrm{N}}{\log(1/\mathrm{r})} \qquad (5.4)$$

5.2.1.2 Box Counting Method

The most popular algorithm for computing the fractal dimension is the box counting, method. In this method, the fractal surface is covered with a grid of n- dimensional boxes or hyper-cubes with various side lengths, and subsequently counting the number of boxes

that contains a part of fractal surface, as illustrated in Figure 5.4. In Figure 5.4, by counting the number of squares that contain part of the Koch curve for each grid. Here three grids with ratios 1: 1/2: 1/4 are used, with counts 18, 41 and 105 as seen in Figure 5.4a, Figure 5.4b,and Figure 5.4c respectively (Wahl, 2014).

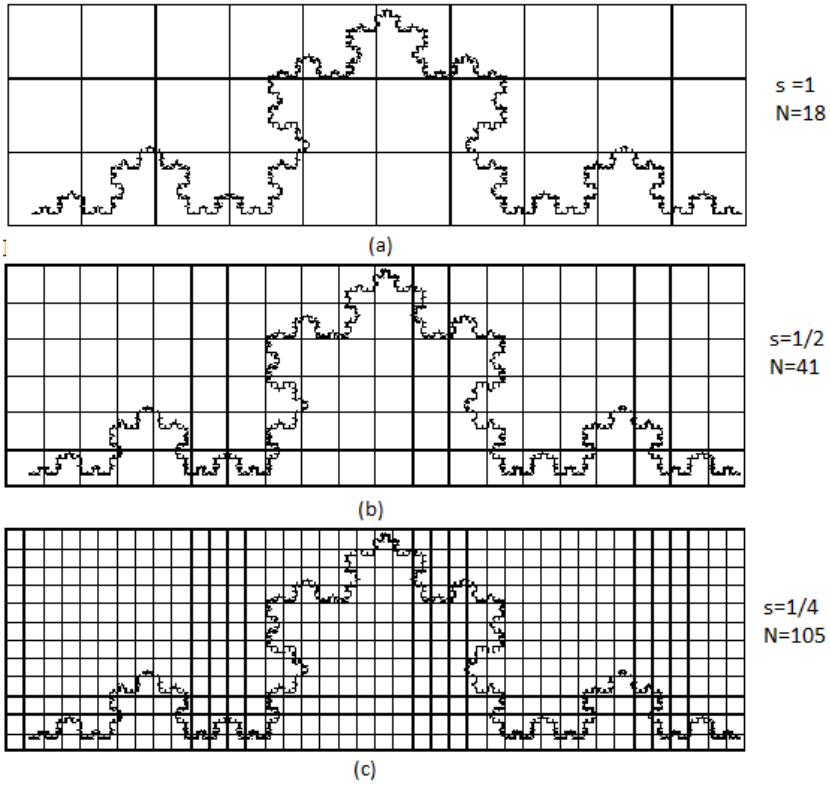

Figure 5.4 The Koch curve with different grid size and the counting number (Wahl, 2014)

The fatal dimension (FD_{box}) is calculated by the Equation (5.5). Where $N(a)$ and $N(b)$ represent the number of boxes that require to cover the entire fractal surface at grid scales of $s(a)$ and $s(b)$, respectively.

$$FD_{box} = \frac{\log N(a) - \log N(b)}{\log\left(\frac{1}{s(a)}\right) - \log\left(\frac{1}{s(b)}\right)} \tag{5.5}$$

5.2.2 FD Calculation

5.2.2.1 Test Specimens

Six test samples are chosen to demonstrate the fractal dimension analysis. The size of each sample is 512 mm long by 1 mm wide, as described in Table 5.1. Note that the six samples have the different MPD values. The profiles with MPD values less than 1mm are considered as the smooth pavement surface. Similarly, for profiles with MPDs ranged at [1.0mm, 1.5mm) and ≥1.5mm, they can be considered as intermediate rough and rough pavement surface, respectively. Accordingly in this case samples 1 and 2 can be taken as the smooth pavement surface; samples 3 and 4 are considered as the intermediately rough pavement surface, and samples 5 and 6 are considered as the rough pavement surface.

Table 5.1 MPD at the Six Test Samples

Sample ID	Sample Length	Sample Width	Starting IMG ID	Ending IMG ID	MPD
1	512	1	28	28	0.79
2	512	1	31	31	0.97
3	512	1	20	20	1.18
4	512	1	34	34	1.30
5	512	1	7	7	1.53
6	512	1	3	3	1.85

5.2.2.2 Sample Interpolation

In order to produce the high resolution profile data (e.g. 0.1mm resolution), the two adjacent pixels in original profiles are interpolated nine pixels and the new profiles are produced, with a resolution of 0.1mm, as shown in Figure 5.5. The original sample consists of 512 pixels, and the newly produced profile has 5211 pixels. Figure 5.5a, Figure 5.5b, and Figure 5.5c represent the newly produced profiles from samples # 1 and

#2 with low complexity, samples #3 and #4 with intermediate complexity, samples #5 and #6 with high complexity, respectively. Afterwards, the walking divider method is used on these newly produced profiles to calculate the measured profile length over a series of observation scales.

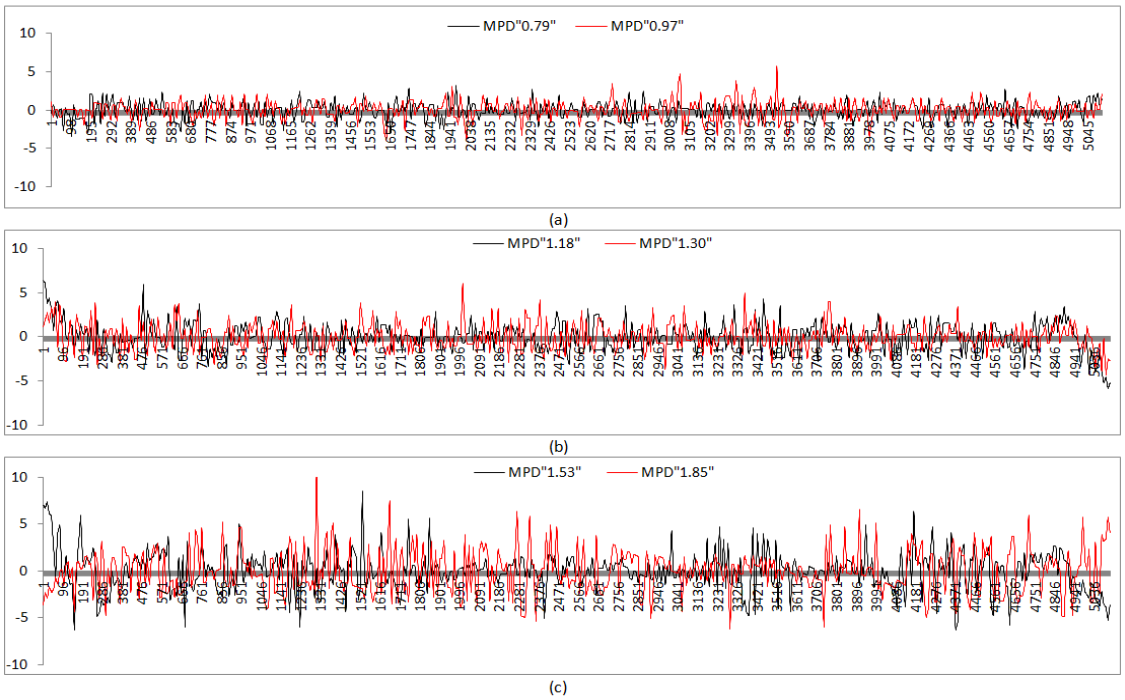

Figure 5.5 Profiles of six different MPDs (a) MPD less than 1mm, (b) MPD ranged at[1mm,1.5mm], (c) MPD ranged at [1.5mm,2mm]

5.2.2.3 FDA by Walking Divider Method

The nominal profile length of each sample is 512 mm which is equivalent to the sample length. The measured profile length would vary with the change of observation scale, as illustrated in Table 5.2. It can be observed that the measured profile length decreases with the increase of step lengths for the six samples, and the measured profile length is approaching the nominal profile length once the step length is long enough.

Table 5.2 Changes of the Measured Profile Length under Different Step Lengths

Step Length (r)	The Measured Profile Length (mm)					
	Sample #1	Sample #2	Sample #3	Sample #4	Sample #5	Sample #6
1	707	749	790	838	874	1006
2	598	644.45	656.36	674.41	736	810
3	564	569.4	579.6	618	628.88	730.71
4	530.8	546.52	552.12	562.42	584	637.71
5	521.51	536.57	540	547.4	566.78	600
6	523.44	530.25	536.8	532.19	581.91	570.75
7	518	527.94	528.32	525.71	549.59	584.46
8	517.33	524.84	523.44	524.25	548.3	547.64
9	514.41	515.91	522.36	518.86	528.82	549.45
10	513.71	515.27	524.38	517.86	531.79	527.58

Based on the nominal and measured profile lengths, the relative length at each step length can be calculated. Followed by is to determine the number of relative lengths and step lengths for FD calculation, as shown in Figure 5.6. Apparently, the slopes are not constant at different step lengths or observation scales, and gradually decease with the increase of step lengths. A constant value (e.g. 0) would be reached when the step length is large enough. Before the slope reaches a fixed value, there is a gradual change at some scales, and these scales can be used for fractal dimension calculation.

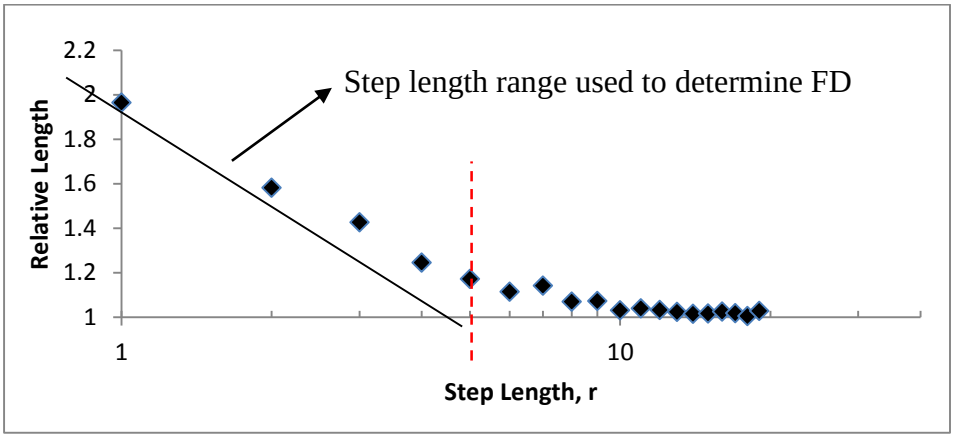

Figure 5.6 A length-scale plot with the step length ranged at [1, 20]

Note that the selection of step lengths and relative lengths is critical for the calculation of fractal dimension. After several trials and errors, the first five pairs of the step lengths and relative profile lengths are used to determine the fractal dimension. Based on the first five data sets, the linear regression method is used to estimate the slope of the log-log plot of relative length versus step lengths, and the fractal dimension at each sample can be calculated using the predefined formula, as given in Table 5.3.

Table 5.3 FD calculated by Walking Divider Method for These Six Profiles

Complexity	Sample #1	Sample #2	Sample #3	Sample #4	Sample #5	Sample #6
MPD	0.79	0.97	1.18	1.30	1.53	1.85
Scale (r)	1 to 5					
Slope	-0.0856	-0.1021	-0.118	-0.1354	-0.1497	-0.1922
FDs	1.0856	1.1021	1.118	1.1354	1.1497	1.1922

5.2.2.4 FDA by Box Counting Method

Three grid scales (i.e. 1, 2, and 4) are used to count the number of grids needed to cover the entire fractal surface, and the calculated results are given in Table 5.4.

Table 5.4 FD by Box Counting Methods for These Six Profiles

Complexity	Sample #1	Sample #2	Sample #3	Sample #4	Sample #5	Sample #6
MPD	0.79	0.97	1.18	1.30	1.53	1.85
Scale: (s)	1 ,1/2,1/4					
FDs	1.2131	1.2480	1.2817	1.3186	1.3489	1.4389

5.2.2.5 Comparison and Analyses

The relationships between FDs calculated from the two approaches are examined. Although the two approaches produce the different FDs for the same samples, the excellent correlations are obtained, as illustrated in Figure 5.7

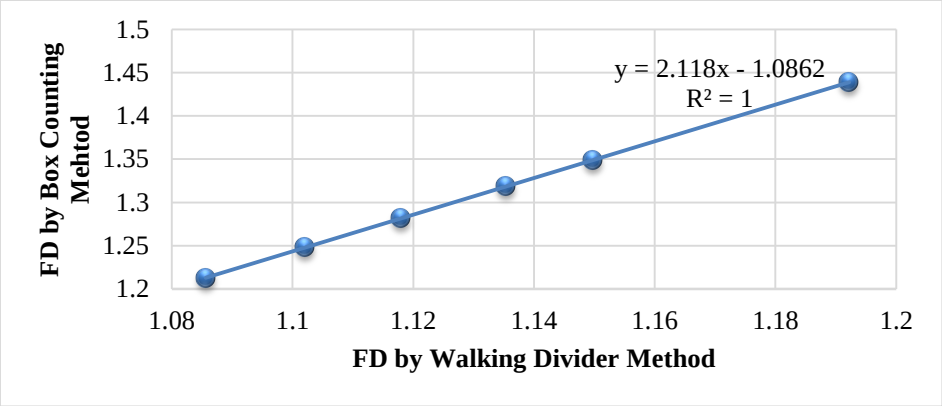

Figure 5.7 Correlation of FDs between walking divider method and box counting method

It can be concluded that the FDs from the two approaches can be transformed from each other based on the build-up models. In this study the fractal dimension from box counting method would be used for Hurst Exponent calculation due to its popularity in fractal dimension calculation.

5.3 Height Difference Correlation

Typically the roughness of a surface texture can be represented with the profile z(x), the arbitrary transformation would keep the surface statistically invariant if the surface is self-affine, as mathematically described in Equation (5.6).

$$x \xrightarrow{\text{yields}} \Lambda x, \qquad z \xrightarrow{\text{yields}} \Lambda^{H} z \tag{5.6}$$

Where H is Hurst exponent which is related to the fractal dimension D (D= 2-H, $0 \leq H \leq 1$).

Apart from the surface fractal dimension D, the other two surface descriptors are also used to characterize a self-affine surface: (1) the correlation length $\xi_{||}$ parallel to the surface and (2) the correlation length $\xi_{\perp}$ perpendicular to surface. One solution to

describe the surface roughness with the height difference correlation function, as given in Equation (5.7).

$$\mathrm{HDCF}(\lambda) = \langle(\mathrm{z}(\mathrm{x}+\lambda) - \mathrm{z}(\mathrm{x}))^2\rangle \tag{5.7}$$

Where $\langle ... \rangle$ denotes the average value; HDCF (λ) describes the mean square height difference of the surface at the horizontal length scale λ.

For the self-affine surface texture, the height difference HDCF(λ) would be approximating to a constant value with the increase of the length scale λ . Assume the HDCF(λ) starts keeping invariant at the length scale λ_z, and the mathematical descriptions can be given in Equations (5.8) and (5.9).

$$HDCF(\lambda) = (\frac{\lambda}{\xi_{||}})^2 \, {\xi_{\perp}}^2 \; for \; \lambda < \xi_{||} \tag{5.8}$$

$$HDCF(\lambda) = {\xi_{\perp}}^2 \; for \; \lambda > \xi_{||} \tag{5.9}$$

From Figure 5.8, it can be observed that the correlation lengths $\xi_{\perp}$ and $\xi_{||}$are determined at the length scale $\xi_{||}$. For the length scale less than $\xi_{||}$, the linear equation with a slope of 2H exists. That is, the $\xi_{||}$ can be determined with the linear equation. To calculate the $\xi_{||}$, the $\xi_{\perp}$ needs to be determined first.

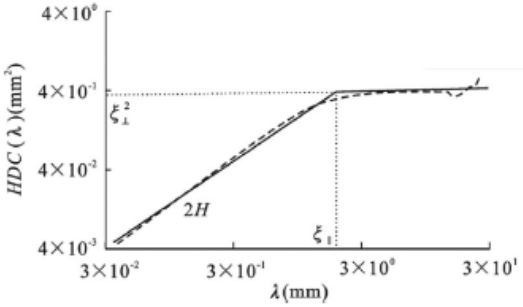

Figure 5.8 Determination of texture descriptors $\xi_{||}$, $\xi_{\perp}$ and H (Torbruegge et al, 2015)

Typically the correlation length $\xi_{\perp}$is dependent on the variance of the measured height distribution of a surface, and the variance is calculated by Equation (5.10).

$$Var(z) = \langle (z(x) - \langle z \rangle)^2 \rangle \tag{5.10}$$

The mean height of the surface profile is represented with $\langle z \rangle$. For the self-affine pavement surface, the relationships between variance and height correlation $\xi_{\perp}$ can be mathematically described using Equation (5.11).

$$\xi_{\perp} = \sqrt{2Var(z)} \tag{5.11}$$

Moreover, using equation to calculate the $HDCF(\lambda_{min})$ at the minimum wavelength scale λ_{min}, and then the correlation length $\xi_{||}$ is calculated by Equation (5.12):

$$\frac{{\xi_{\perp}}^2 - HDCF(\lambda_{min})}{\xi_{||} - \lambda_{min}} = 2H \tag{5.12}$$

So far the three basic elements of surface texture descriptors for self-affine surface have been determined. The accurate estimations of these three texture descriptors are critical for the prediction of pavement friction coefficients.

5.4 Zener Slider Model and Tire Penetration Depth

In addition to the three texture descriptors, the complex viscoelastic properties of the sliding rubber needs to be known over a broad range of frequencies to predict the real area of contact and the energy dissipation during sliding. The theory estimates that various length scales that contribute to the built-up of the rubber friction force (Klüppel et al, 2000). For example, a typical range of wavelengths for an asphalt surface would be between 0.01 mm and 100 mm. Depending primarily on the sliding speed, these

deformation processes lead to excitation frequencies, which can reach the order of 10^7 rad/s and higher.

5.4.1 Zener Slider Model

To represent the viscoelastic behavior of rubbers, a Zener slider models, also termed standard linear solid model, is introduced. The Zener slider model is a generalization of the simple constant spring and dashpot models, as illustrated in Figure 5.9.

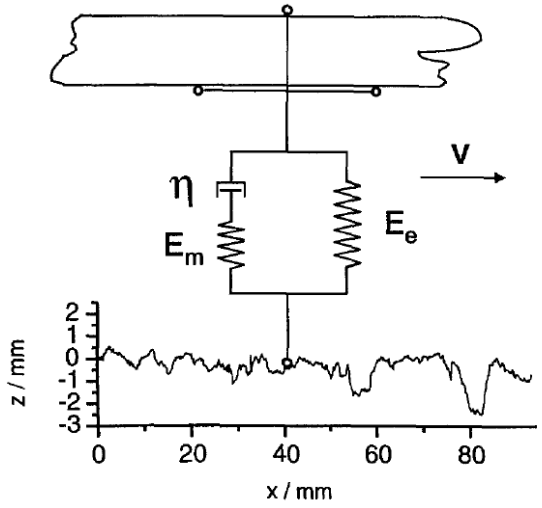

Figure 5.9 Diagram of the basic elements of Zener slider models (Klüppel et al, 2000)

Its complex modulus can be described in Equation (5.13).

$$E(\omega) = E'(\omega) + iE"(\omega) = \frac{E_e + (E_m + E_e)\omega^2{\tau_z}^2}{1 + \omega^2{\tau_z}^2} + i\frac{E_m\omega\tau_z}{1 + \omega^2{\tau_z}^2} \qquad (5.13)$$

Where $\tau_z = \eta/E_m$ is the characterization relaxation is time of the Zener Slider; E_e is the elastic modulus of the spring in parallel with the damping having viscosity modulus of η; E_m is elastic the modulus of the spring in series with the damping; the angular velocity $\omega = 2\pi\upsilon/\lambda$ depends on sliding velocity and surface profile wavelength.

The rubber storage and loss modulus are denoted by $E'(\omega)$ and $E"(\omega)$, respectively, which are related to sliding velocity, surface profile wavelength distribution, and the three modulus in Zener Slider Model.

5.4.2 Tire Penetration Depth (TPD) Estimation

The elastic contact between rubber and rough surfaces typically occurs at the summits of the highest asperities, as described in Figure 5.10. The d is the distance between the two surfaces and $\phi_z$is the normalized distribution function of the surface summits.

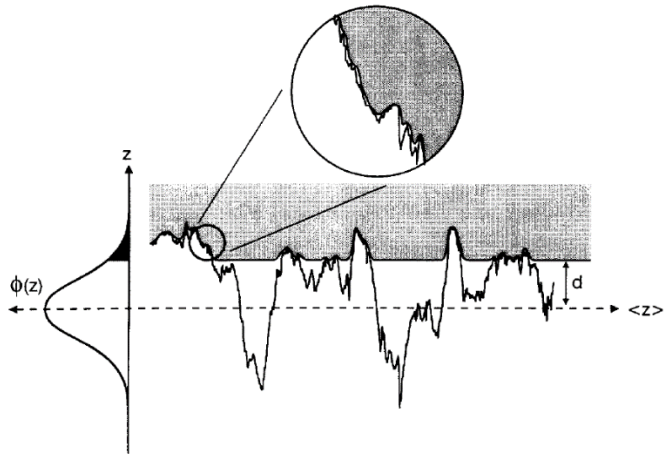

Figure 5.10 The elastic contact between a rubber and rough surface (Klüppel et al, 2000)

Greenwoods and Williamson (GW) developed a rough surface contact theory which can be used to evaluate the mean penetration depth into the asperities, involving in the variance of the surface height (m_0), square mean slope of surface height (m_2), and the curvature of the height (m_4). Their mathematical descriptions are given in Equations (5.14), (5.15), and (5.16), respectively.

$$m_0 = Var(z) \tag{5.14}$$

$$m_2 = \langle \left(\frac{dz}{dx}\right)^2 \rangle \tag{5.15}$$

$$m_4 = \langle \left(\frac{d^2z}{d^2x}\right)^2 \rangle \tag{5.16}$$

The statistical parameter of the GW theory $\alpha = m_0 m_4 / {m_2}^2$ which determines the variance of the surface summit distribution and the asperity density of the surface. The surface summit distribution δ_s and the distance d between two surfaces can be determined by α, as described by Equations (5.17) and (5.18):

$$\delta_s = \left(1 - \frac{0.8968}{\alpha}\right) m_0 \tag{5.17}$$

$$d = 4\sqrt{\frac{m_0}{\pi\alpha}} \tag{5.18}$$

The GW theory can be expressed by the normalized distribution function ϕ_Z of the profile z(x), and the surface height varianceσ, height mean μ, and the mean distance d, given in Equations (5.19) and (5.20):

$$\phi_Z = \frac{1}{\sigma\sqrt{2\pi}} e^{-\frac{(z-\mu)^2}{2\sigma^2}} \tag{5.19}$$

$$F_1\left(\frac{d}{\sigma}\right) = \int_{d/\sigma}^{\infty} \left(z - \frac{d}{\sigma}\right) \frac{1}{\sigma\sqrt{2\pi}} e^{-\frac{(z-\mu)^2}{2\sigma^2}} dz \tag{5.20}$$

Based on Equation, the relationship between the mean penetration depth and the normal stress can be expressed in Equation (5.21):

$$\langle z_p \rangle = \tilde{\sigma}\, F_1\left(\frac{d}{\sigma}\right) \tag{5.21}$$

5.5 Power Spectra Analysis

Power spectral analysis is used to calculate the spectrum density of various wavelengths of the surface profile, which is a well-known method for the interpretation of complicated signals containing a variety of wavelengths and amplitudes (Sayers, 1996). In order to investigate the power energy intensity at various wavelengths, typically two methods are available (Karamihas, 2005). One method is based on its autocorrelation function, which can be obtained by converting the integral calculation to the sum of the sampled elevation points for digitalized discrete road profiles, and these conversions can be mathematically expressed by Equations (5.22) and (5.23):

$$R_{xx}(\tau) = \lim_{L} \int_0^L x(t) * x(t-\tau)\, dt = \sum_{i=1}^{N} |x(t)x(t - i * L/N)| \tag{5.22}$$

$$PSD(f) = \int_0^L R_{xx}(\tau) e^{-j2\pi f\tau} d\tau = \frac{1}{N^2} \sum_{k=1}^{N} \sum_{i=1}^{N} |x(t)x(t - i * L/N)| * e^{-j2\pi fkL/N} \tag{5.23}$$

Where L is the profile length, τ is the offset value for profiles, N represents the sampled elevation points for this profile, $x(t)$represents the road height at the time t along road.

The other method is based on the Fourier Transform (FT) which can be obtained by computing the amplitudes of the sinusoids that are decomposed from the road profile. In this paper FT based power spectral analysis is conducted.

5.5.1 Fourier Transform

Fourier Transform decomposes a series of discrete points into a sum of sinusoids of various frequencies, amplitudes and phases. The output of the transformation represents squared amplitude at each frequency of the original image in the frequency domain (Karamihas, 2005). Typically, Fourier Transform can be mathematically expressed as Equation (5.24).

$$\mathrm{F}(k,l) = \sum_{i=0}^{N-1}\sum_{j=0}^{M-1} f(m,n)e^{-i2\pi(\frac{km}{N}+\frac{ln}{M})} \tag{5.24}$$

Where N and M represent the image size, f (m, n) is the gray intensity of height values at pixel (m, n); F (k, l) is the transformed amplitude at frequency(k, l) or wave number(k, l).

A 2D pavement image with a size of 4096 mm wide by 2048 mm high is chosen to illustrate the implementation of Fourier transform, as the Figure 5.11(a) shows. After Fourier transform, the each pixel in the Fourier image represents the root mean square of the amplitudes, as the Figure 5.11(b) shows. Moreover, the center point in this Fourier image represents the minimum frequency or wave number, namely zero, and the wave number would increase as the distance between the center point and any other point coordinate increases.

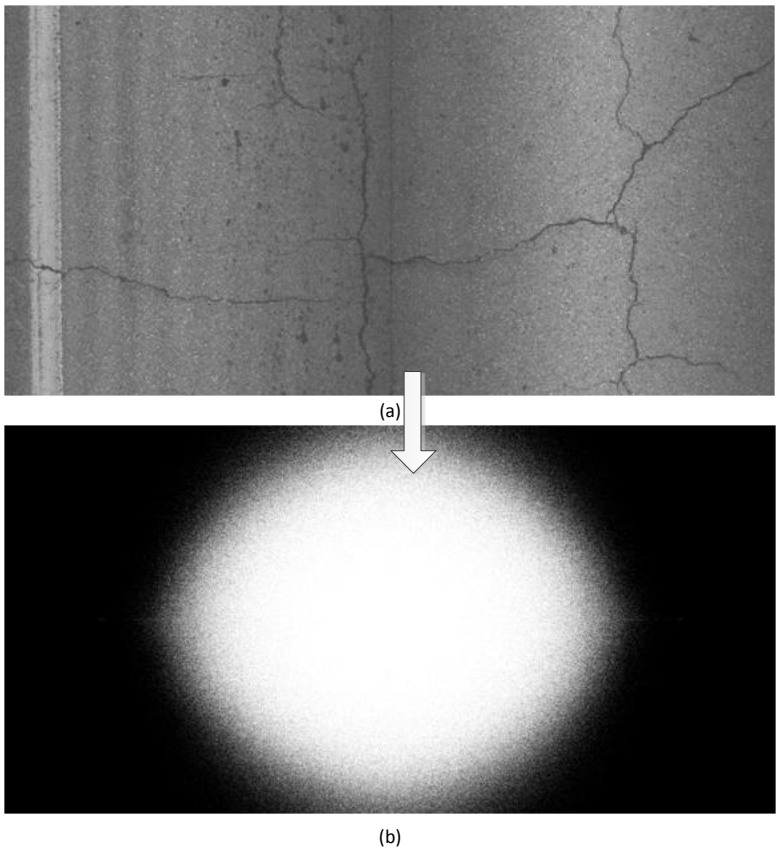

Figure 5.11 (a) 2D image collected by DHDV; (b) the amplitude based Fourier image

5.5.2 Wave Number Determination

Once all the wavelength and their corresponding amplitudes are determined, the following task is to determine the waveband of interest. The range of wave numbers of interest in this study would be restricted to from the 20 to 500 cycle/m covering 480 wave numbers, and the wave numbers out of that range would be discarded.

5.5.3 PSD Calculation

Fourier transform can be scaled such that it shows how variance of profile is distributed over wave numbers associated with sinusoids. When scaled in this manner, this transform is called a PSD function (Sayers, 1996). It can be computed by Equation (5.25)

$$\mathrm{PSD}(j,k) = |Re(j,k)|^2 + |Im(j,k)|^2 \qquad (5.25)$$

Where Re (j,k) represents the real part of a complex variable in u and v directions in frequency domain, and the Im(j,k) represents the imaginary part of this complex.

An example is taken to demonstrate the distribution of PSD over wave number, as shown in Figure 5.12. The result indicates that the PSD of elevation decreases with the increase of wave number, which implies the long wavelength is highly associated with the high amplitudes of elevation variation. Note that there is no sharp increase or decrease in PSD along the wave number, indicating there is no exceptional wavelength ranges that should be noticed.

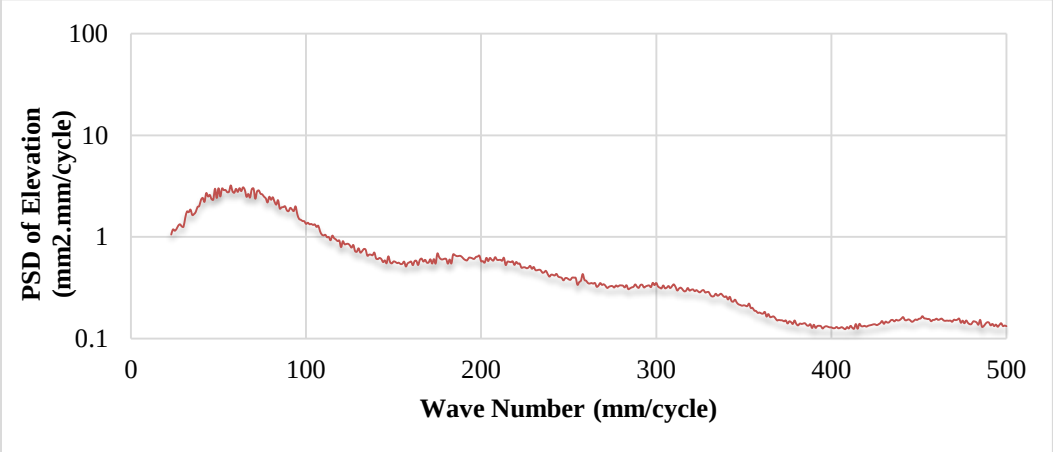

Figure 5.12 PSD distribution along wave number

5.6 Case Study

The same test section presented in Section 4.7.1 is used for pavement friction prediction based on Heinrich/Klüppel model.

5.6.1 Friction Field Measurement

The test section can be sampled into 25 segments with each segment having a length of 50ft based on the total section length of 1264ft. The HFST segment starts with the location of approximately 300ft and ends with the location of approximately 1000ft, as marked in Figure 5.13. Note that the three measurements have the excellent agreements with each other, with the correlation coefficients of 0.96, 0.99, and 0.96, respectively. In this study the average friction number from the three measurements are served as the basis for the comparison and validation with predicted friction.

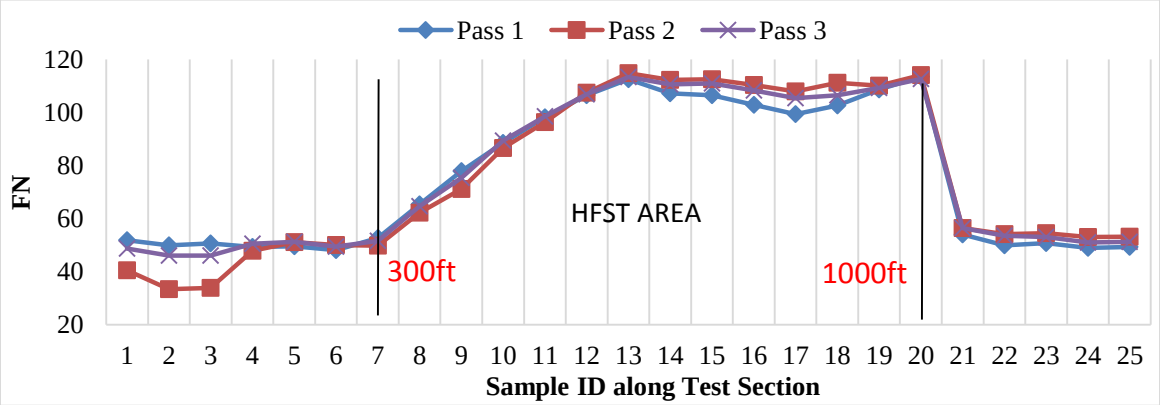

Figure 5.13 Friction measurement results on AL I 65 ramp

5.6.2 Pavement Friction Prediction

As presented in Section 5.1, Heinrich/Klüppel friction theory is used to predict pavement friction number based on the 3D texture data collected on the test section. Through a

series of data processing techniques presented in Sections 5.2, 5.3, 5.4, and 5.5, the friction coefficients can be predicted, as shown in Figure 5.14.

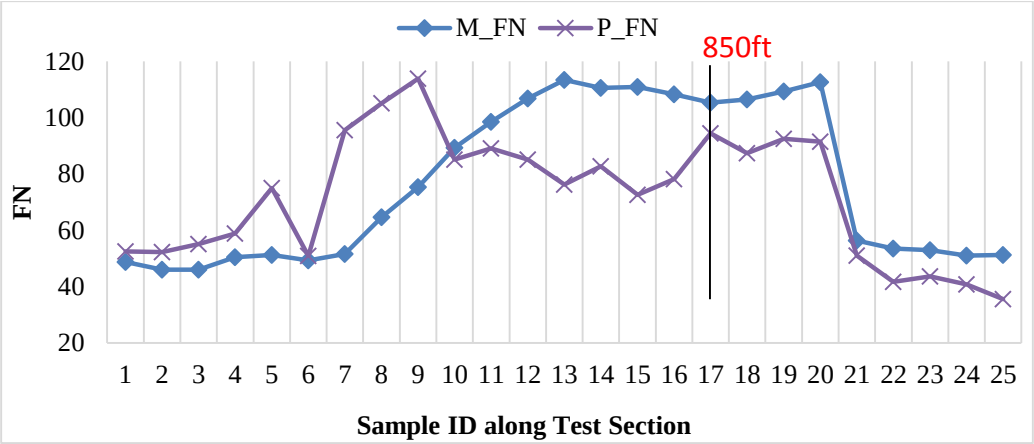

Figure 5.14 Comparison between predicted and measured FNs

Note that the agreements between predicted and measured FNs are not as good as that shown in Figure 5.13, but there is a quite good agreement for the section after 850ft. The large difference appears at the transition segment between regular pavement surface and HFST such as Sample ID#7. Also, the large differences also appear at the HFST segment such as Sample ID# 15. Accordingly more research work are recommended to address these issues.

The linear regression analysis is used to investigate the relationships between the measured and predicted FNs, and their correlation results are plotted in Figure 5.15. Note that all FNs at the regular segment are less than 60, and most FNs at HFST segment are greater than 100. Findings indicate the fair correlation results ($R^2 = 0.58$) are observed due to the presence of the outliers, as marked in Figure 5.15.

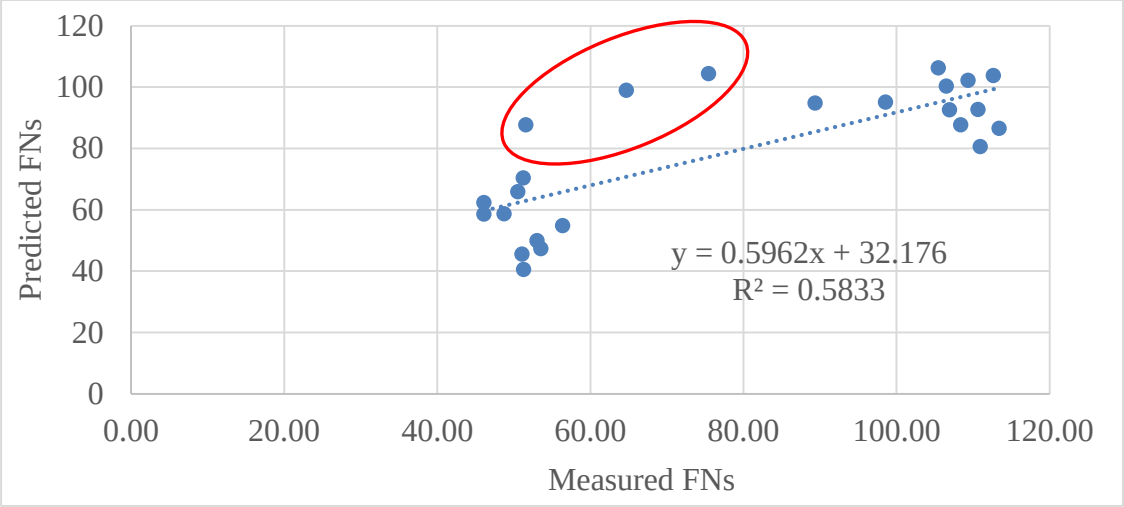

Figure 5.15 Linear regression results between predicted and measured FNs

Once the marked outlier in Figure 5.15 are removed and the remaining data are modeled with linear regression method, a good correlation result is observed, with an R-squared value of 0.79, as shown in Figure 5.16.

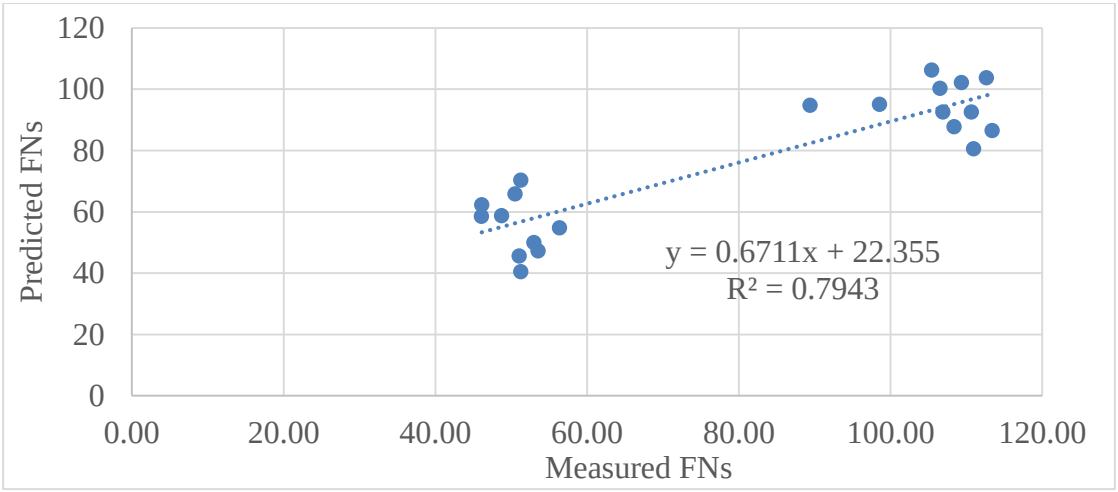

Figure 5.16 Linear regression results after outlier removal

As a result, the good agreement between theory and field measurements is observed once the outliers are excluded. It should be emphasized that the theory models can be improved by tuning up the parameter settings, the use of the calibration coefficients, and

the calculation methods of the parameters. In addition, more field validations are recommended to improve the reliability of the theory model on the project- or network-level pavement safety surveys.

5.7 Summary

This chapter firstly introduces the basic working principle of the rubber friction theory by Heinrich/Klüppel, in which the hysteresis friction coefficient is calculated from the dissipated energy during sliding on a rough surface. The estimation of dissipated energy over a distance needs to deal with surface texture roughness, the rubber properties, and the contact mechanics between rubber surface and pavement surfaces.

Several key parameters are presented to describe surface texture roughness, rubber properties, and the contact mechanic in Heinrich/Klüppel model. For instance, Hurst Exponent, height difference correlation lengths parallel and perpendicular to pavement surface are used to describe surface texture roughness. The complex modulus is used to describe rubber properties, and the mean tire penetration depth is the representation of the contact mechanics between the tire and pavement surface. Subsequently their computations are presented as well.

Finally a case study is used to illustrate the application of Heinrich/Klüppel model on pavement friction prediction, and a good agreement is observed between the predicted and measured FNs. However, for the purpose of the project- and network- level safety survey, more field validation work need to be conducted on various AC pavements in order to improve the reliability of the models.

CHAPTER 6. AUTOMATED GROOVE IDENTIFICATION, MEASUREMENT, AND EVALUATION

Pavement and airport grooves are designed and constructed : 1) to improve pavement friction-related safety by increasing contact areas of pavement and aircraft/vehicle tires; 2) to eliminate the potential hydroplaning risk by providing a path for water to escape from under the tire of an aircraft/vehicle as rapidly as possible; 3) to increase the lateral stability and maintain aircraft/vehicle on the road by maneuvering aircraft/vehicle in a safe manner (in both longitudinal and lateral direction); and 4) to minimize influences of the tire-pavement noises on drivers, passengers, and urban residents.

Substantial field studies and research efforts have scientifically proven that pavement surface grooves play a significant role in preventing skid-related crashes, exclusive of other contributing factors such as driver-related and vehicle-related. In addition, hydroplaning speed prediction models have been developed to investigate the relationships between skid resistance and groove dimensions (depth, width, and spacing). Results indicate larger

groove depth and width, and tighter groove spacing would result in better frictional properties. Particularly, changes in groove depth are found to have the most significant effect on hydroplaning.

Typically the newly constructed grooves enable to meet the prescribed performance requirement during the initial service phase; however, surface grooves deteriorate over time from repeated interaction with aircraft or vehicle traffic, as well as from additional interaction with pavement maintenance activities such as rubber removal, sweeping, and snowplowing operations. Therefore, the periodic monitoring and assessment on grooves are critical for avoiding the skid-related crashes and lowering the louder tire-pavement noises. In this chapter, two types of pavement grooves are chosen as examples to demonstrate the implementation of automated groove identification, measurement, and evaluation.

6.1 Types of Grooves

Roadway grooves can be broadly grouped into two categories based on groove configuration orientation relative to traveling direction, namely transverse and longitudinal grooves. Transverse grooves mainly include rectangular-shaped and trapezoidal shaped grooves, and the longitudinal grooves encompass the traditional longitudinal grooves and Next Generation Concrete Surface (NGCS).

In this paper the rectangular-shaped transverse grooves would be examined for automated transverse groove identification, measurement, and evaluation since the rectangular-shaped transverse grooves are commonly used in airport runways and state highways. For the study on longitudinal groove performance evaluation, NGCS would be

used because it has three advantages over the traditional longitudinal grooves, such as the lower noise, the higher pavement friction, and the better lateral stability.

6.1.1 Transverse Grooves

Currently rectangle-shaped transverse grooves are the most commonly used surface texture technique on airport runways. Based on the field test results from FAA research program, a groove configuration of 1/4-in.-by 1/4-in.-square grooves spaced at 1 1/2 in. center to center is adopted as the FAA standard to date (see Figure 6.1a) (FAA, 1997). As shown in Figure 6.1, the transverse groove is perpendicular to the traveling direction. The areas between two adjacent grooves are termed as the landing area.

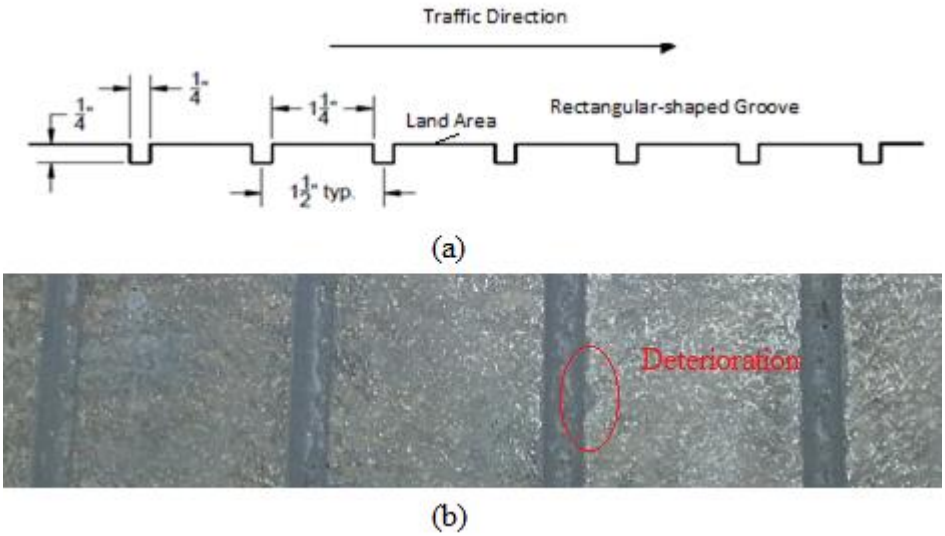

Figure 6.1 Photographs of a) schematic diagram of standard groove configurations; b) deteriorated transverse groove

It is well known that the rectangular-shaped transverse groove would deteriorate over time due to effects of repeated traffic, as shown in Figure 6.1b. To determine whether the worn grooves comply with groove performance requirement, the FAA research program

provides a certain tolerance for standard grooves (FAA, 1997), described as follows: 1) the acceptable depth range at [0.19in, 0.31in]; 2) the acceptable groove width range at [0.25 in, 0.31 in]; 3) and the acceptable groove spacing range at [1.38in, 1.5 in], as illustrated in Table 6.1.

Table 6.1 Recommended Groove Configuration and Its Tolerance

Groove type	Recommended configuration (Unit: in)		Tolerance (Unit: in)		Acceptable range			
			Lower limit	Upper limit	Unit: inch		Unit: mm	
Rectangular	Depth	1/4	-0.0625	1/16	0.19	0.31	4.76	7.94
	Width	1/4	0	1/16	0.25	0.31	6.35	7.94
	Space	1 1/2	-0.125	0	1.38	1.5	34.9	38.1

6.1.2 Longitudinal Grooves

Longitudinal grooves are broadly used to enhance the lateral stability during wet weather, as well as to decrease influences of road-tire noises on drivers and passengers. However, field studies indicate the longitudinal grooves provide the lower pavement friction when compared with transverse grooves with the same dimension (including groove width, depth, and spacing) (Mahone et al, 1977), and lead to the potential safety issues.

To increase surface skid resistance on the longitudinally grooved pavement, Next Generation Concrete Surface (NGCS) is developed. NGCS is the new non-porous concrete texture introduced in the last 20 to 30 years, which is a hybrid texture that resembles a combination of diamond grinding and longitudinal grooving for concrete pavement. Field studies and research efforts indicate that NGCS places a significant role in noise reduction, aircraft/vehicle lateral stability, and hydroplaning resistance (Scofield, 2011).

The currently constructed NGCS dimension is provided by Kansas DOT (see Figure 6.2a-b), which has a size of 11/32 in deep, 5/32in wide and spaced 5/8 in apart (Scofield, 2012). Currently there is no tolerance range provided for NGCS dimension since more investigations need to be conducted on the impacts of groove dimension on safety performance. NGCS has not widely used in state highways due to the high cost for construction of NGCS.

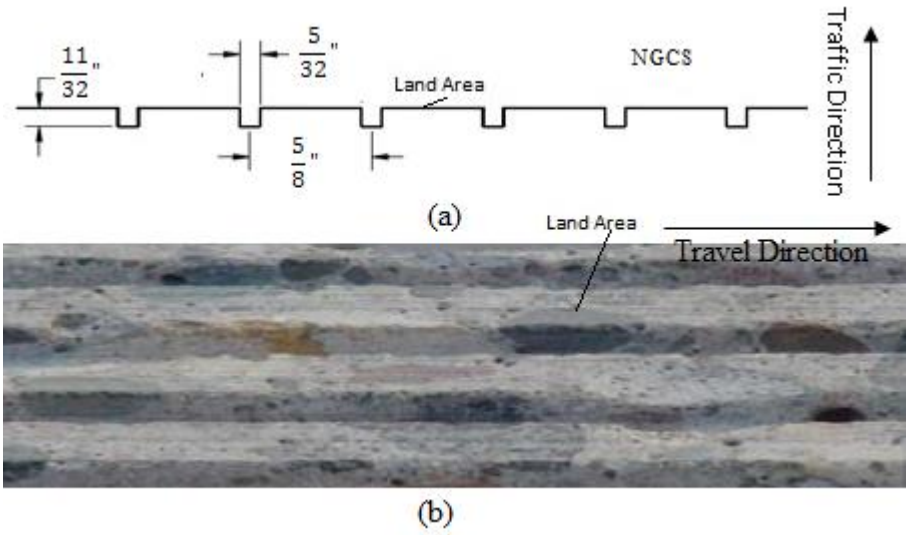

Figure 6.2 Photographs of a) schematic diagram of NGCS configuration; b) constructed NGCS in the field

6.2 Methodology Framework

The proposed methodology for automated groove identification, measurement, and evaluation is implemented in four phases, as schematically illustrated in Figure 6.3. The first phase aims to identify potential dips namely grooves and joints; the second phase is to determine the starting and ending position of a dip and calculate the corresponding dip dimensions; the third phase is to separate joints from grooves, and the last phase is to

evaluate groove performance in accordance with the guidelines specified in FAA Advisory Circular AC 150-5320-12C.

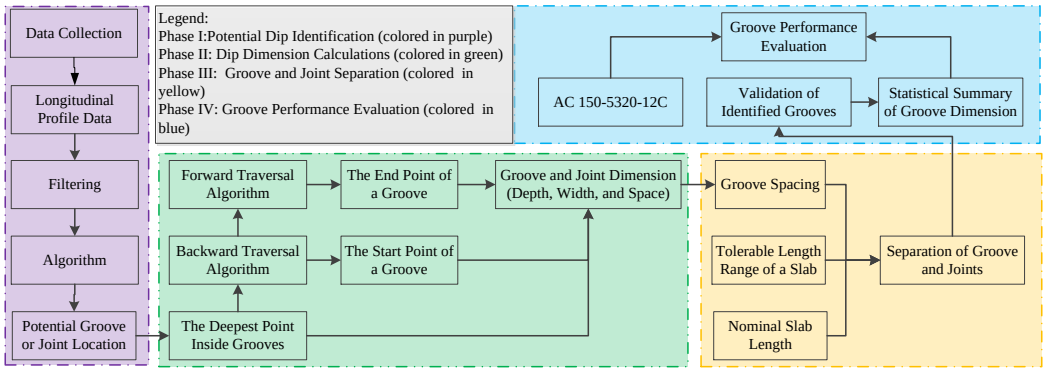

Figure 6.3 Schematic diagram of the methodology for groove identification, measurement, and performance evaluation

6.3 Filtering Techniques

The identification of potential dip is dependent on elevation differences between the raw and filtered profile data. In this study the raw profile is defined as the initially collected profile data, and the filtered profile stands for the processed profile after removing the unwanted information, as demonstrated in Figure 6.4(a). However, for grooving pavements, the generation of filtered profile is susceptible to the impact of narrow dips, which leads to the elevation difference (i.e. 2.84mm) at narrow dips smaller than the actual dip depths(i.e. 3.33mm), as shown in Figure 6.4(b). Generally the smaller elevation difference would result in identification difficulty of shallow grooves. For example, if the threshold used to identify dips is set to 3.0 (greater than 2.84mm) in Figure 6.4, the shallow groove would be failed to be identified. Therefore suppressing effects of narrow dips on filtered profile is critical to identify the potential dips.

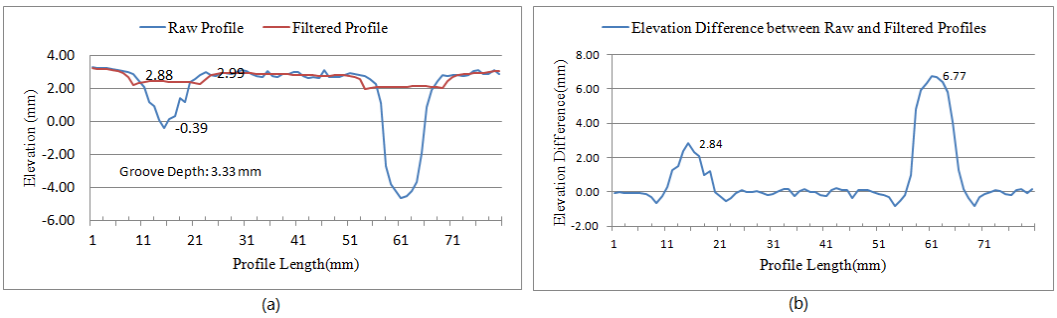

Figure 6.4 a) Example of raw profile and filtered profile; b) example of elevation difference between raw and filtered profile

In this study filtering techniques are designed to aim to maximally eliminate the long wavelengths and retain or enhance groove features, as well as remove the unconcerned noises (short wavelengths). As a result, three fitlers namely mask filter, landing area data based filter, and Euler-Bernoulli beam filter are designed and used for roadway groove identificaiton.

6.3.1 Mask Filter

Moving average filter, an important component of mask filtering, is a simple but widely used traditional method in profile analysis. It is implemented by simply replacing each profile point with the average of several adjacent points within a specified base length. For a profile P that has been sampled at interval Δ, its moving average filter is given in Equation (6.1):

$$\mathrm{P}_{mo}(i) = \frac{1}{N} \times \sum_{j=i-B/\Delta}^{j=i+B/\Delta} P_{ori}(j) \qquad (6.1)$$

Where P_{mo} represents the smoothed profile after moving average filter is applied; B stands for the base length of the filter; P_{ori} represents the original profile; and N stands for the number of adjacent points centered at i.

Applying Equation (6.1) on the original profile produces the smoothed profile, in which the long wavelength component of the original profile remains unchanged, but the short wavelength component is altered significantly, as shown in the Figure 6.5(a).

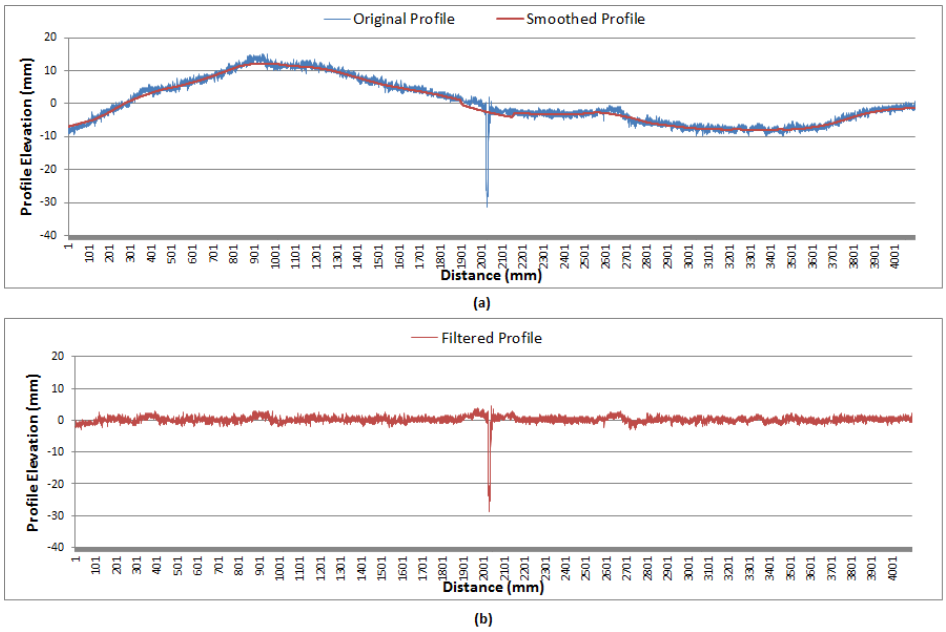

Figure 6.5 Plots of (a) original profile and its corresponding smoothed profile, (b) the filtered profile after applying the mask filter

It can be seen that the short wavelength components such as groove or joints have been suppressed, but the smoothed profile still has the similar trend with the original profile, which indicates moving average filter fails to get rid of the long wavelength components of profiles. As a result, moving average filter is an efficient tool to remove the short wavelength component of the profiles but not suitable for suppressing the long

undulations of the profile. However, the suppression of the long wavelengths plays an important role in groove identification. If the long undulations cannot be eliminated, the undesired identification results would be obtained. Accordingly, the high pass filter should be used to remove the long undulations, and typically it can be conducted in spatial domain and frequency domain. The mask filter, conducted in spatial domain, is proposed to reduce influences of long wavelengths on groove identifications.

The implementation of masking filter is divided into two steps: 1) producing the new profile by smoothing the original profile with moving average filter; 2) producing the filtered profile by subtracting the smoothed profile from the original profile. The resulting difference is called the mask. Making filter has two advantages over other high pass filters: 1) easy to implement; 2) a better noise reduction effect especially for profiles with various wavelengths. Letting P_{ori} and P_{maf} denote the original and smoothed profile respectively, the filtered profile $\mathrm{P_{mf}}$ can be calculated using Equation (6.2).

$$\mathrm{P}_{mf}(i) = P_{ori}(i) - P_{maf}(i) = P_{ori}(i) - \frac{1}{N} \times \sum_{j=i-B/\Delta}^{j=i+B/\Delta} P_{ori}(j) \qquad (6.2)$$

The filtered profile that is produced from mask filter is illustrated in Figure 6.5(b). Note that the long wavelength components including the general shape of the original profile have been totally suppressed, meanwhile, the short wavelength components are kept, but there is one weakness for this filter. It is not easy to determine the appropriate base length for moving average filter. If the selected base length is too short, a sharp drop in profile elevation would appear at the approaching and departing surface grooves due to influences of grooves, leading to some potential dips might not be identified depending

on dip widths, depths, and spacing. If the selected base length is too long, although the filtered profile can maximally suppress influences of dips on the resulting smoothed profiles, it also introduces some noise in landing area, which causes the quantity of the identified dips might be more than the actual quantity.

6.3.2 Land Area Data based Filter

The design of this filter is based on the assumption that a small portion of rubber tire would penetrate into the road grooves when aircraft or vehicles travels on road surface, whilst the large portion of rubber tires would sit on the landing areas of grooving pavements (karamihas,2005), as shown in Figure 6.6. The filter aims to eliminate effects of narrow dips on the filtered profiles, so grooving profile data can be modeled with the non-grooving profile data. With this filter, the dip identification accuracy depends on the selection of contact patch summit and length.

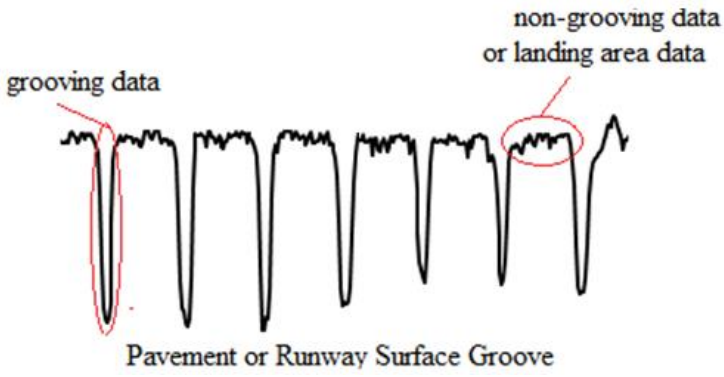

Figure 6.6 Grooving data and landing area data for grooving pavements

6.3.2.1 Contact Patch Summit Determination

The histogram based approach is proposed to determine percentages of landing area data. To intuitively illustrate the philosophy of this approach, an example is given in Figure 6.7

(a). In this example, the raw profile consisting of 1000 points contains 22 grooves. The filtered profile after removing long undulations is shown in Figure 6.7 (b). The corresponding histogram is illustrated in Figure 6.7 (c). It can be observed that 77.3% data (100%-19.1%-3.6% =77.3%) has the elevation no less than 0 mm. In other words, the non-grooving data accounts for around 80% of the profile data in terms of the test example.

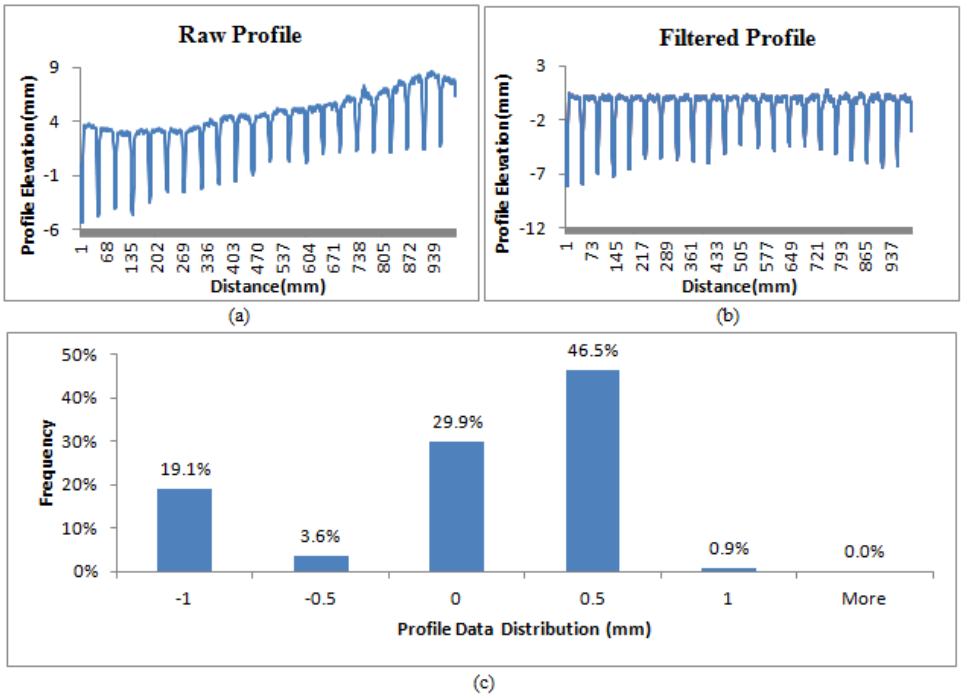

Figure 6.7 Photographs of a) example of the raw profile data; b) the filtered data after long undulation suppression; 3) histogram based groove and non-groove data distribution

Note that rubber tires only interact with large portions of road surface when aircraft or vehicles travel, and the contact patch summits can be described using the percentage of histogram frequency that is used to denote the percentages of the profile data. Due to the presence of surface irregularities and grooves, the possibility of complete contact between tires and road surface are trivial, accordingly the maximum percentage of 80% is

used in this study. In order to determine the most appropriate histogram frequency for the new filter, three percentage (40%, 60%, and 80%) levels are used, as shown in Figure 6.8. Herein, 40% histogram frequency implies the largest 40% profile data within a certain base length are used to filter the grooving data, and the similar usage are for 60% and 80% histogram frequencies.

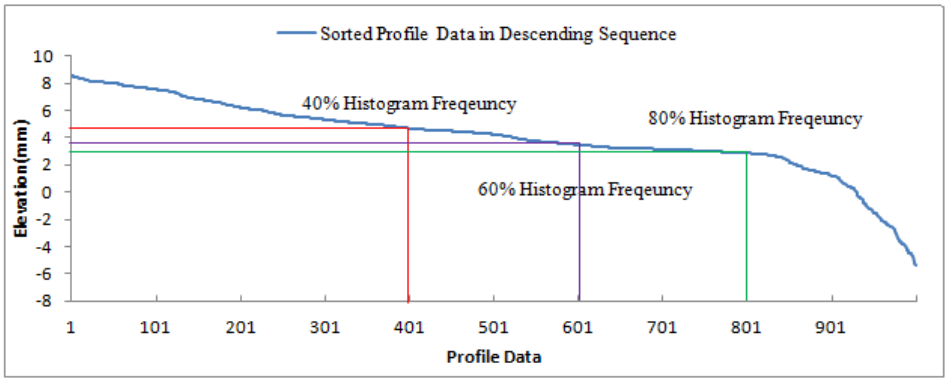

Figure 6.8 The three percentage levels of profile data for filtering

6.3.2.2 Contact Patch Length Determination

The selection of contact patch length depends on three factors: groove width, groove spacing, and footprint areas between tires and pavement surface. In this paper, three contact patch lengths: 9 mm, 43 mm, and 75 mm are tested.

6.3.2.3 Filter Implementation

The landing area based filter is implemented in four steps. Firstly draw a window centered at point P with a predetermined length and store the framed profile data (candidate data) into an array; secondly sort the candidate data in descending sequence and store results into a new array (Arr); thirdly calculate the mean elevation at a given histogram frequency ($Per\%$) and set it as the corresponding point elevation (E) of the

filtered profile; fourthly repeat steps 1 to 3 until all point elevations in the raw profile are replaced with the new values. The mathematical description of this filter is given in Equation (6.3).

$$\mathrm{E} = \frac{1}{N_i} \times \sum_{j=0}^{j=N_i} Arr(j), \quad N_i = Per\%_i \times N \tag{6.3}$$

Where E: the point P elevation of the filtered profile; Arr: the sorted array in descending sequence; $Per\%_i$: the histogram frequency ($Per\%_1$ =40%, $Per\%_2$ =60%, $Per\%_3$ =80%); N: the total number of points within a contact patch; N_i: the number of contact points between tires and pavement surface at percentage level i

Based on statistical analyses from test samples, it is found the landing area data based filter produces the best effects when the 60% histogram frequency and the 43mm contact patch length are used.

6.3.3 Euler–Bernoulli Beam Filter

Euler–Bernoulli beam theory is also designed to suppress influences of narrow dips on the filtered profiles base on the assumption that a small portion of rubber tire would penetrate into the grooves after aircrafts or vehicles have traveled on pavement surface.

6.3.3.1 Euler–Bernoulli Beam Theory

Euler–Bernoulli beam theory is a simplification of the linear theory of elasticity which provides a means of calculating the load-carrying and deflection characteristics of beams, as illustrated in Figure 6.9. The relationship between the beam's deflection and the applied load can be described in Equation (6.4) (Gere, 1997).

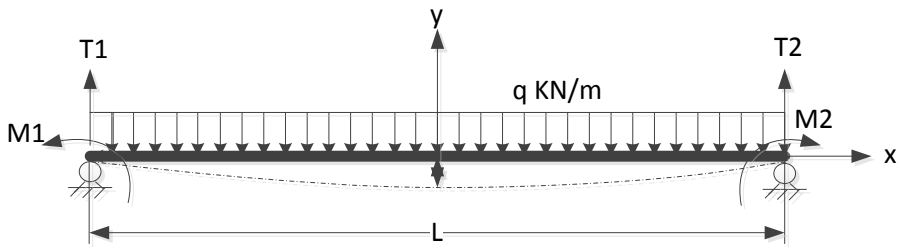

Figure 6.9 Diagram of acting force and bending moment of contact model

$$\frac{d^2}{dx^2}\left(EI\frac{d^2w}{dx^2}\right) = q(x) \tag{6.4}$$

where $w(x)$ describes the deflection of the beam in the y direction at some position x ; $q(x)$ is a distributed load along x direction(a force per unit length); E is the elastic modulus and I is the second moment of area of the beam's cross-section; EI is a constant to describe beam bending stiffness.

In addition, the bending moment M in the beam can be derived from successive derivatives of the deflection w(x), as described in Equation (6.5).

$$\mathrm{M} = -EI\frac{d^2w}{dx^2} \tag{6.5}$$

6.3.3.2 Conservation of Energy Formulation

Per the law of energy conversation, the virtual work generated from vehicle tire loads should be equivalent to the strain energy. In this paper the strain energy is assumed to be associated with profile data, and its computation can be described in Equation (6.6). The generated virtual work is the product of tire loads applied on the beam and its virtual displacement, as expressed in Equation (6.7). As a result, the energy equilibrium formulation can be described in Equation (6.8). For the purpose of simplification of

computation, in this case the mean virtual displacement is assumed to 1 mm (Karamihas 2005), so that the tire load can be readily derived.

$$E_t = \sum_{i=1}^{N} (y_i - \bar{y})^2 \tag{6.6}$$

$$\sum \delta W = \sum_{i=1}^{N} F_i \cdot \delta r_i = N \times \bar{F} \times \overline{\delta r} \tag{6.7}$$

$$\sum \delta W = E_t \tag{6.8}$$

where E_t denotes the total strain energy; y_i represents the profile elevation at point i; N represents the number of points at the contact area between tires and pavement surface (in this case N is set to 75); $\bar{y}$ denotes the mean of profile elevation; δW describes the virtual work; $\bar{F}$ denotes the mean tire load; $\overline{\delta r}$ denotes the mean virtual displacement.

6.3.3.3 Deflection or Displacement Calculation

Due to the symmetry of the tire-pavement contact area, it can be assumed that the vehicle load is symmetrically distributed about the beam center. The uniform stress q and bending moment M(x) at point x can be derived as in Equation (6.9) and (6.10).

$$\mathrm{q} = \frac{\bar{F}}{L} = (E_t \,/\overline{\delta r})/L \tag{6.9}$$

$$M(x) = \int_{-L/2}^{x} -qx\, dx = \frac{q}{2}(L^2/4 - x^2) \tag{6.10}$$

Under a prescribed load, the bending moment at a point x should be a constant, and thus bending moment from Euler–Bernoulli beam theory should be equivalent to that derived from the shear stress q acting on the beam, as described in Equation (6.11).

Finally the defection at point x and the filtered profile elevation h(x) can be calculated using Equations (6.12) and (6.13), respectively. An example is taken to demonstrate the new filter eliminating effects of narrow dips on filtered profile, as illustrated in Figure 6.10. Note that the effects of narrow dips are totally suppressed after the Euler-Bernoulli beam filter is applied.

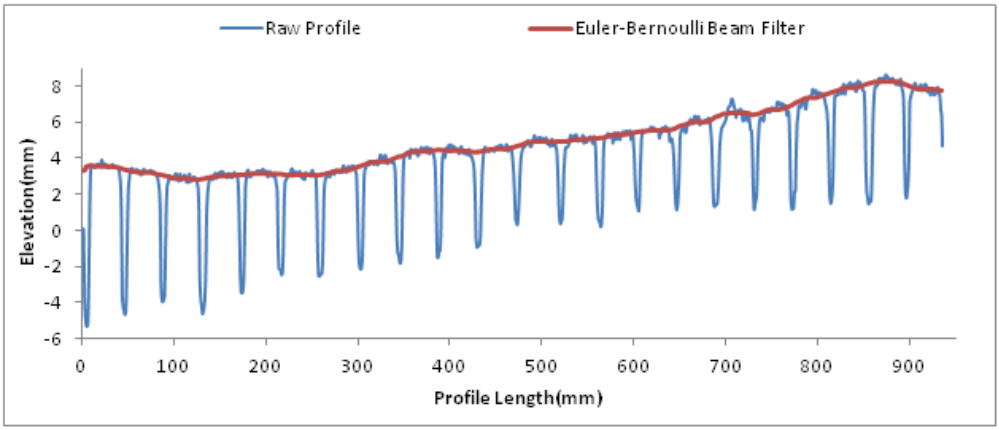

Figure 6.10 Example of the Euler-Bernoulli beam filter

$$-EI\frac{d^2\mathrm{w}}{dx^2} = \frac{q}{2}(L^2/4 - x^2) \tag{6.11}$$

$$w(x) = -\frac{q}{EI}(0.125L^2x^2 - 0.083x^4 - 0.026L^4) \tag{6.12}$$

$$h(x) = \frac{y_{p1} + y_{p2}}{2} - \overline{w(x)} \tag{6.13}$$

where L represents the length of contact area between tires and pavements, x represents the x coordinates, with the origin at the beam center (computed as: $i \times N/L$); $h(x)$ represents the filtered profile elevation at coordinates x; y_{p1} and y_{p2} respectively represent two highest peaks within the contact area.

Generally mask filter cannot effectively eliminate influences of narrow dips on the filtered profile and further the subsequent dip identification, but is easy to implement. Landing area data based filter and Euler-Bernoulli beam filter produce the better filtering effects on the filtered profiles than mask filter. By comparison with landing area data based filter and Euler-Bernoulli beam filter, the preceding one can maximally suppress the influences of dips on the filtered profile, which benefit in identifying the shallow dips but simultaneously introduce some unexpected noises, whilst Euler-Bernoulli beam filter can effectively decrease identified noises.

6.4 Groove Identification Approaches

Once the filtered profile is produced, the following task is to use it as the basis for the groove identification. Two groups of groove identification techniques are presented in this section. One technique is gradient based, in which the groove location is dependent on the presence of a pair of larger gradients. The other one is based on the identification of deepest dip, that is, the grooves can be identified by locating the deepest point inside grooves, including template matched algorithm and geometry contour based algorithm.

6.4.1 Gradient based Algorithm

The basic idea behind this algorithm is that each groove has a pair of gradients or slopes varying sharply. The calculation of gradient is implemented using the first-order derivative, as mathematically described in Equation (6.14). For a profile f(x), the gradient of f at coordinates x is defined as the one-dimensional column vector: This one-dimensional vector has the important geometrical property that it points to the direction of the greatest rate of change of fat location x, which can be illustrated using Figure 6.11.

$$\nabla f = grad(f) = \left[\frac{\partial y}{\partial x}\right] = \mathrm{f(x+1)} - \mathrm{f(x)} \qquad (6.14)$$

Figure 6.11 (a) shows he original profile data extracted from the raw image; Figure 6.11 (b) shows the filtered profile data after reducing the long undulation, Figure 6.11 (c) shows the gradients or slopes of each groove that are calculated from the filtered profile.

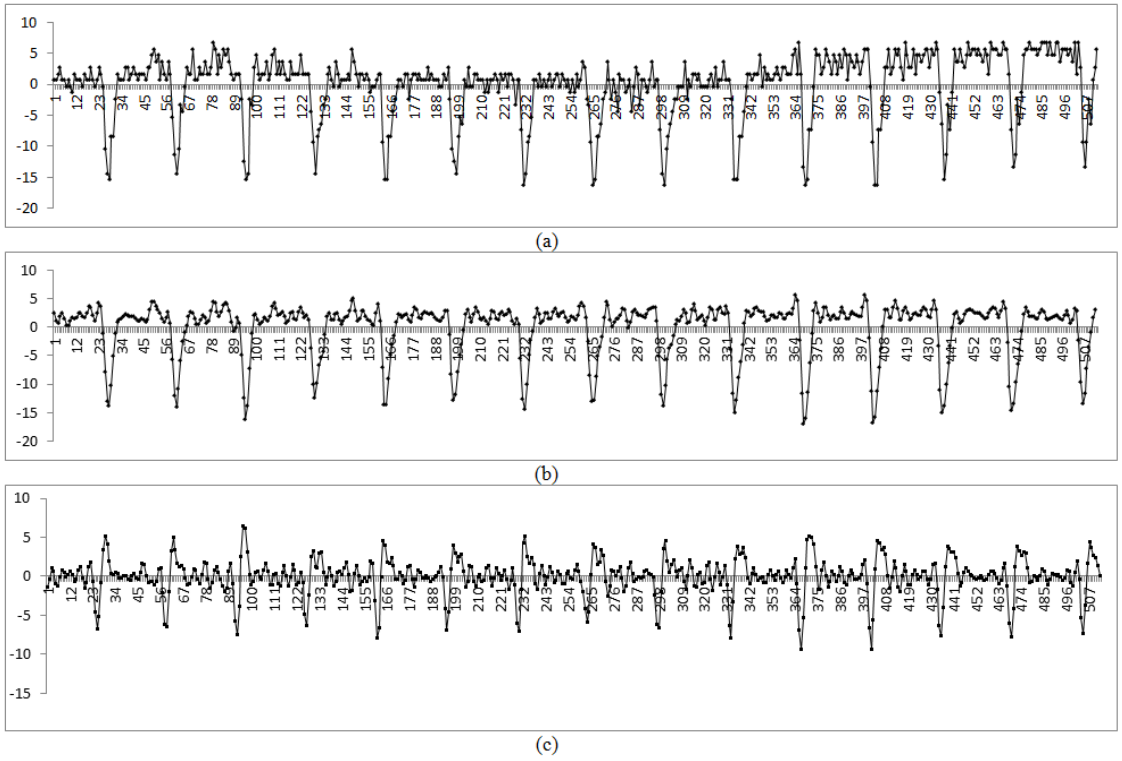

Figure 6.11 Plotting of (a) the original profile; (b) the filtered profile; (c) the gradients or slopes of the filtered profile

Note that a pair of extreme points (gradients) appears inside each groove by comparing Figure 6.11 (b) and Figure 6.11 (c). These extreme points represent the depths at these locations that vary fastest, especially for the depth variations inside grooves. Therefore the potential groove may be identified based on the presence of this pair of extreme points.

Since the extreme points indicate depths vary fastest at these locations, they cannot be considered as the starting and ending points of a groove. To locate the starting point of a groove, a backward traversal operation would be performed by starting at the minima of a pair of extreme points, and be terminated by the traversed gradient is no smaller than -1.0. The threshold of -1.0 is determined through several errors and trials. Similarly, the forward traversal operation would be conducted by starting at the maxima of a pair of extreme points, and be terminated by the traversed gradient is no greater than 1.0.

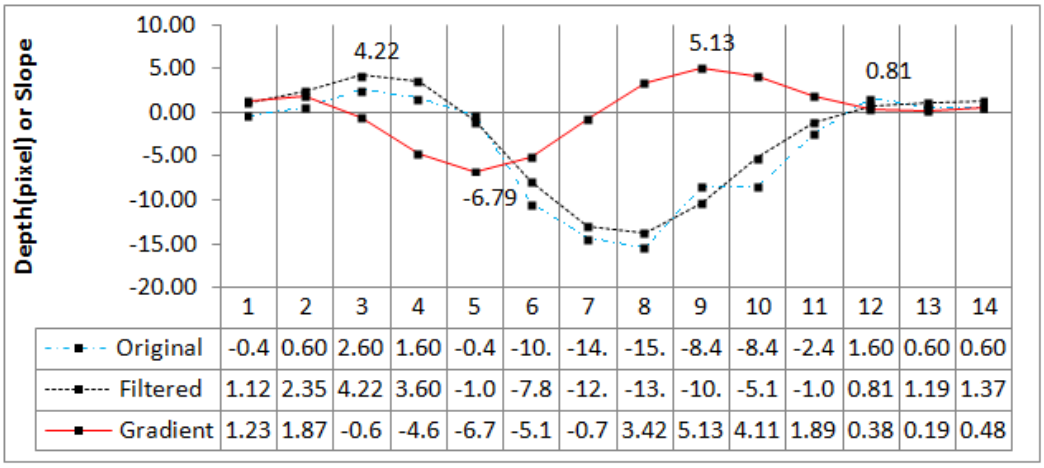

	1	2	3	4	5	6	7	8	9	10	11	12	13	14
Original	-0.4	0.60	2.60	1.60	-0.4	-10.	-14.	-15.	-8.4	-8.4	-2.4	1.60	0.60	0.60
Filtered	1.12	2.35	4.22	3.60	-1.0	-7.8	-12.	-13.	-10.	-5.1	-1.0	0.81	1.19	1.37
Gradient	1.23	1.87	-0.6	-4.6	-6.7	-5.1	-0.7	3.42	5.13	4.11	1.89	0.38	0.19	0.48

Figure 6.12 Example of a groove identification principle

An example is to illustrate the procedure of identifying the starting and ending points of a groove, as shown in Figure 6.12.The minimum gradient with a value of -6.79 is located at the point # 5. Apparently the point #5 is not the starting point of this groove, so the backward traversal approach is used to help locate the starting point of the groove. In this case the traversal operation is terminated at the point #3 with a gradient value of -0.62, so the starting point of the groove is identified as the point # 3, as Figure 6.12 shows. The maximum gradient with a value of 5.13 stands at the point # 9, likewise, the

forward traversal is utilized to help locate the ending point of this groove. The traversal operation is terminated at the point # 12 since the corresponding gradient is no greater than 1.0. Accordingly, the starting and ending points of this groove are identified at point # 3 and the point #12, respectively. Upon locating the starting and ending points of the groove, the deepest point within the groove can be determined by searching the point with deepest elevation values. As a result, the three basis points of one groove are identified.

In this algorithm, the pair of extreme points with the minima and maxima values in gradient is utilized to identify the potential dip, based on which the backward and forward transversal algorithms are proposed to determine the starting and ending points of grooves. Once the two ends of one groove are determined, the deepest point inside grooves can be located based on the profile elevation within the groove. Finally the groove dimension is able to be calculated in compliance with FAA calculation practice.

6.4.2 Template Matched Algorithm

The template matched algorithm, one of the most popular edge detection approaches, is used to detect and identify pavement and runway grooves. The basic concept of template matched algorithm is to pre-define filters that can match the features of a linear pattern such as pavement grooves, and apply the predesigned filters to match with the specific feature of the search profile to be detected.

To design filters that can well match the specific feature of the search target, it is assumed that the cross section of the longitudinal groove has a Gaussian-like shape. Moreover, since groove configurations might vary, three templates or kernels with

different standard deviations are designed. The kernel orientation is constant for the three kernels. These templates or kernels can be mathematically expressed in Equation (6.15) and their corresponding filter shape is illustrated in Figure 6.13.

$$T(i) = -k \times \frac{1}{\sqrt{2\pi}\sigma} exp\left(-\frac{i^2}{2\sigma^2}\right) \forall\, i\, \boldsymbol{\epsilon}\, [-\boldsymbol{N}, \boldsymbol{N}] \qquad (6.15)$$

Where $T(i)$ denotes the discrete Gaussian distribution at location i; k is the reciprocal of the standard deviation (σ); N represent the template window size and it equals to the triple σ.

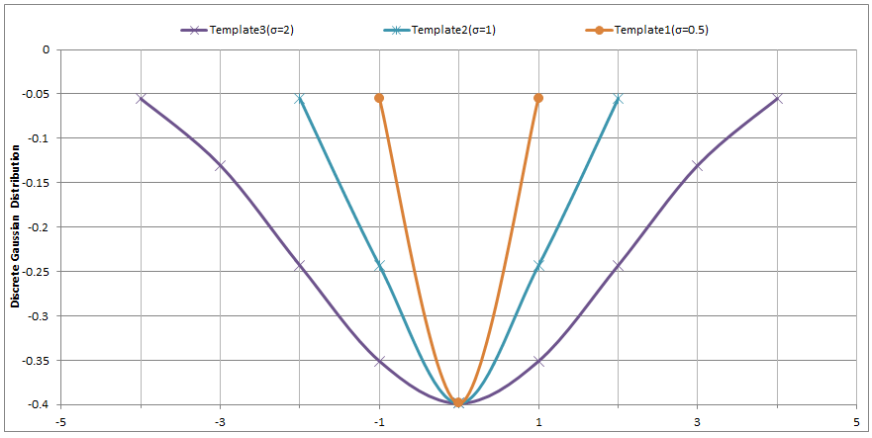

Figure 6.13 An example of three template matched filters

The predefined templates are applied on the filtered profiles to identify the potential grooves. There are two approaches available for groove identification. One method is to find grooves by calculating the cross correlation (R) or the Minimum Square Errors (MSE) between the target profile section and the predefined template. The other method is to identify the grooves by convoluting the predefined kernel with the filtered profile, as described in Equation (6.16). Subsequently comparing the convolution coefficients with

adaptive thresholds is to determine the potential grooves locations. The first approach is expensive in computation, so the second approach is used in this study.

$$C(i) = \sum_{j=max(0,i-\frac{N}{2})}^{j=min(M,i+\frac{N}{2})} F(j) * T(j) \; \forall \; i \; \boldsymbol{\epsilon} \; [\mathbf{0}, \boldsymbol{M}] \qquad (6.16)$$

where $C(i)$ denotes the convolution result at location i; $F(j)$ represents the filtered profile at location j ; $T(j)$ denotes the discrete Gaussian distribution at location j; N represents the template window size and it equals to the triple σ; N stands for the number of pixels for the filtered profile.

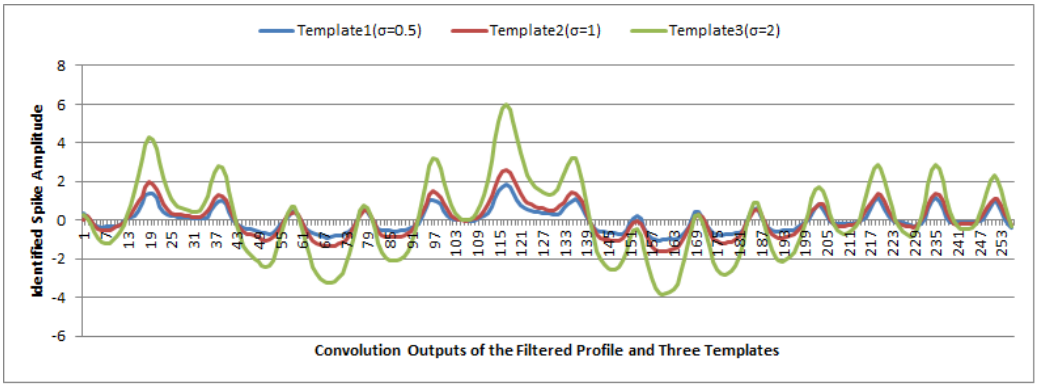

Figure 6.14 Outputs after convoluting filtered profile with three predefined kernels

Figure 6.14 plots the convolution outputs after convolving the filtered profile with three predefined kernels. Even though the spike amplitudes of the three convolution outputs are not identical, the locations of the spikes being consistent are observed. In this study, the convolution outputs from template #3 are used to detect and identify the potential grooves since results from template# 3 have the highest amplitude. Typically each spike, the highest amplitude within a small range, represents one potential groove.

Once the deepest point within one groove is demined, the two end points of each groove can be located by the transversal operations as described in the gradient based algorithm. Herein, the smoothed profile is used as the threshold to replace the prescribed thresholds in gradient based algorithm (e.g. -1.0 and 1.0), and subsequently the two end points are determined based on the original profile and the smoothed profile. An example is taken to illustrate how the new approach is to determine the two end points of one groove, as demonstrated in Figure 6.15.

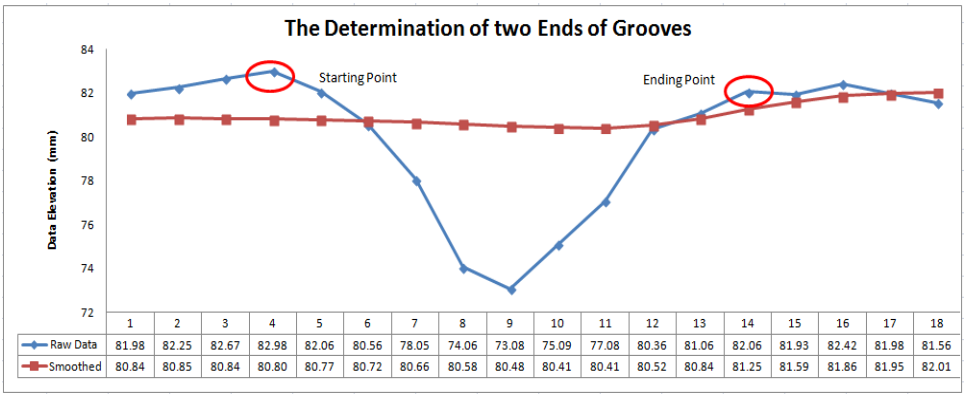

	1	2	3	4	5	6	7	8	9	10	11	12	13	14	15	16	17	18
Raw Data	81.98	82.25	82.67	82.98	82.06	80.56	78.05	74.06	73.08	75.09	77.08	80.36	81.06	82.06	81.93	82.42	81.98	81.56
Smoothed	80.84	80.85	80.84	80.80	80.77	80.72	80.66	80.58	80.48	80.41	80.41	80.52	80.84	81.25	81.59	81.86	81.95	82.01

Figure 6.15 The principle for determination of two end points of grooves

In this example the smoothed profile after applying moving average is used as the reference line to assist in locating the beginning and ending positions of grooves. There is one solid rule that needs to follow: pixel values of the starting and ending position of grooves must be larger than the corresponding pixel values of the smoothed profile. In other words, the two end points of grooves of original profiles should be above the corresponding points of smoothed profile, as marked in Figure 6.15.

To find the starting point of a groove, a forward traversal operation is performed by starting with the deepest point within grooves, and is terminated until the traversed

gradient is no smaller than 0 and the current pixel value is larger than the corresponding pixel value of the smoothed profile, in this case the starting position is located at the pixel #4. The determination of starting point Gs at coordinates of i is given in Equation (6.17).

$$\mathrm{Gs}(i) = \begin{cases} op(i) > rp(i) \\ \nabla f(i) \leq 0 \\ \nabla f(i-1) > 0 \end{cases} \qquad \forall\, i \,\boldsymbol{\epsilon}\, [\mathbf{1}, \boldsymbol{N}] \tag{6.17}$$

Similarly, the backward traversal technique is used to find the ending position of grooves by starting with the deepest point within grooves, and is terminated until the traversed gradient is no larger than 0 and the current pixel value is larger than the corresponding pixel value of the smoothed profile, in this case the ending point of the groove is located at the pixel # 14. The determination of ending point Ge at coordinates of i is given in Equation (6.18).

$$\mathrm{Ge}(i) = \begin{cases} op(i) > rp(i) \\ \nabla f(i) > 0 \\ \nabla f(i+1) \leq 0 \end{cases} \qquad \forall\, i \,\boldsymbol{\epsilon}\, [\mathbf{0}, \boldsymbol{N} - \mathbf{1}] \tag{6.18}$$

This traversal approach avoids some unexpected errors on determining two end points of grooves. For example, some identified starting or ending points of grooves may fall inside grooves, instead of standing on landing areas due to groove irregularities.

6.4.3 Geometry Contour based Algorithm

The filtered profile f_f is constituted by the resultant elevation points$h(x)$, and then the elevation differences h_d between the filtered profile f_f and original profile $\mathrm{f_o}$ are calculated and stored into a new array $\mathrm{f_d}$. In Figure 6.16, each spike represents one potential dip occurred in grooves or joints. To identify potential spikes, geometry contour

based algorithm is developed. It aims at identifying the maximum peaks of array f_d across the window length WL, as elaborated as follows:

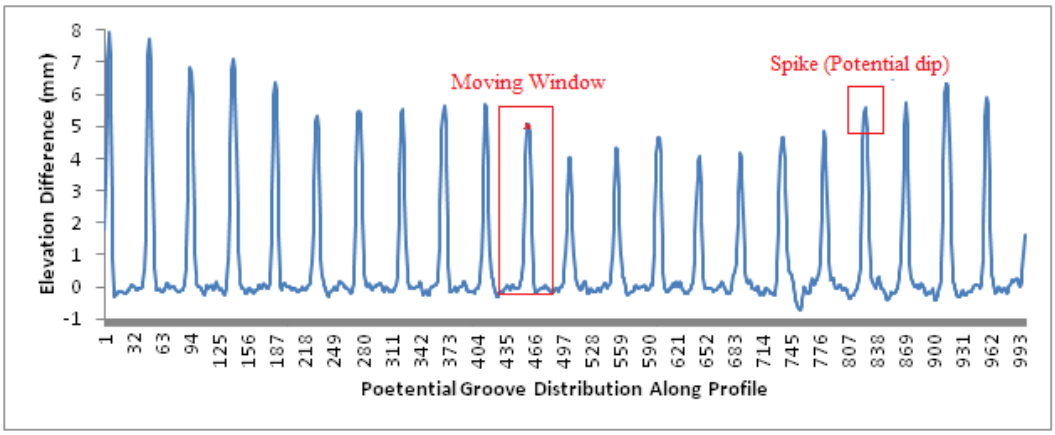

Figure 6.16 Example of implementation of geometry contour based algorithm

For each point i in the array f_d, the corresponding window centered at point i can be derived. If the elevation at point i is greater than the elevations of all points within the window, and simultaneously is larger than the prescribed threshold (T), this point is considered as one of the potential spikes of array f_d, in other words, the point belongs to the profile grooves. Its mathematical description is described in Equation (6.19).

$$\begin{cases} \mathrm{f}_d(i) \geq T \\ f_d(i) \geq f_d(j) \end{cases} \quad j \in \left[i - \frac{WL}{2}, i + \frac{WL}{2} \right] \& j \neq i \tag{6.19}$$

Practically the threshold setting depends on groove depth, and the window length are dependent on groove space. Once the deepest point inside grooves is identified, the subsequent task is to determine the two end points of grooves, and it can be implemented with the transversal algorithms that are used in template matched method.

In summary, gradient based algorithm has the different principle with the other two methods since it is implemented by locating the pair of gradients that have a great rate of the change of data elevation, whereas the other two methods are designed to locate the deepest point within the dips. Based on test results, it is found that the other two methods produce the better results than gradient based method due to the irregularities of grooves.

6.5 Groove Dimension Measurements

6.5.1 FAA AC 150-5320-12C Calculation Practice

Once two end points and the deepest point within a groove are determined, the groove dimension can be calculated by following measurement procedure specified in the FAA Advisory Circular No. 150/5320-12C (FAA, 1997).

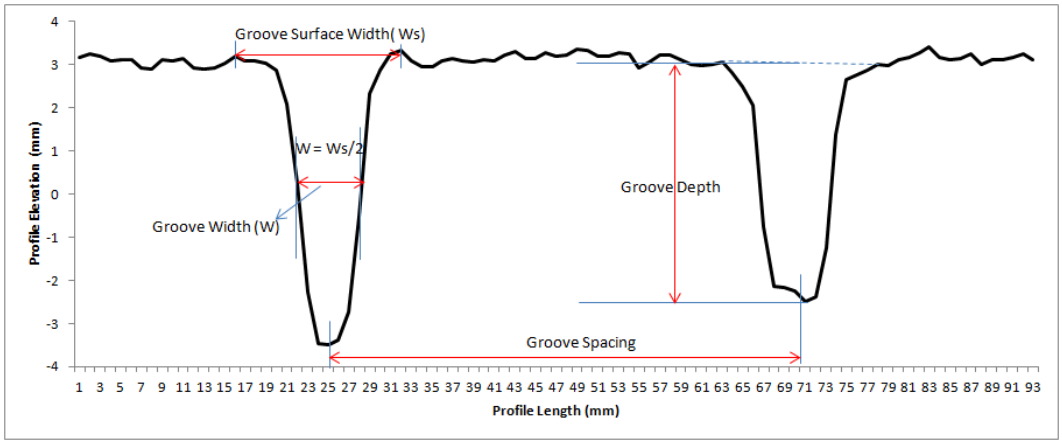

Figure 6.17 The diagram of groove dimension calculation

As Figure 6.17 shows, groove depth is the elevation difference between the average of the maximum depths at both sides of the groove and the minimum depth inside the groove (see Equation (6.20)). Groove width is the half of the distance between the

starting and ending points (see Equation (6.21)). Groove spacing is the distance between the centers of two adjacent grooves.

$$Groove\ Depth = \frac{1}{2} * [f(s) - f(e)] - f(m) \tag{6.20}$$

$$Groove\ Width = \frac{1}{2} * abs(e - s) \tag{6.21}$$

Where $f(s)$ represents the elevation at starting point s of a groove; $f(e)$ represents the elevation at end point e of a groove; $f(s)$ represents the elevation at minimum point m inside a groove.

6.5.2 Multiple Profiles based Groove Dimension Measurement

Due to the existence of surface irregularities, the identified groove quantity may be inconsistent for the different longitudinal profiles, as shown in Figure 6.18.

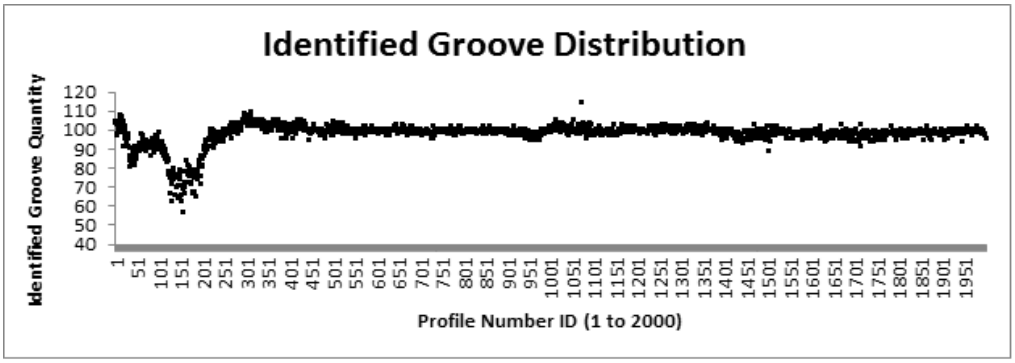

Figure 6.18 Identified groove quantity distribution versus profile number ID

Profile number IDs from 1 to 500 appear the unexpected identification results since the identified groove quantity is much less than the actual quantity. From this figure, it can be concluded that groove dimension calculated from one single profile cannot represents the actual groove dimension of the entire lane. Therefore in this study the

multiple profiles are used in lieu of one line-of-sight profile to identify runway grooves and calculate their dimensions

6.5.3 Groove Volume based Calculation Practice

Groove volume, an important statistical index associated with wet pavement safety, is initially proposed to describe the drainage capacity of measured grooves. Its calculation can be described as follows.

1) Use the two end points of grooves to produce one linear equation, and the reference elevation value $f(x_i)$ at each point within grooves can be calculated in Equation (6.22).

$$f(x_i) = \frac{(y_n - y_1)x_i + y_1 x_n - y_n x_1}{(x_n - x_1)} \qquad \forall\, i \in [x_1, x_n] \qquad (6.22)$$

Where (x_1, y_1) and (x_n, y_n) represents the beginning and ending locations of grooves, respectively; x_i represent the x - coordinates of points within grooves, $f(x_i)$ represent the reference elevation values at point x_i.

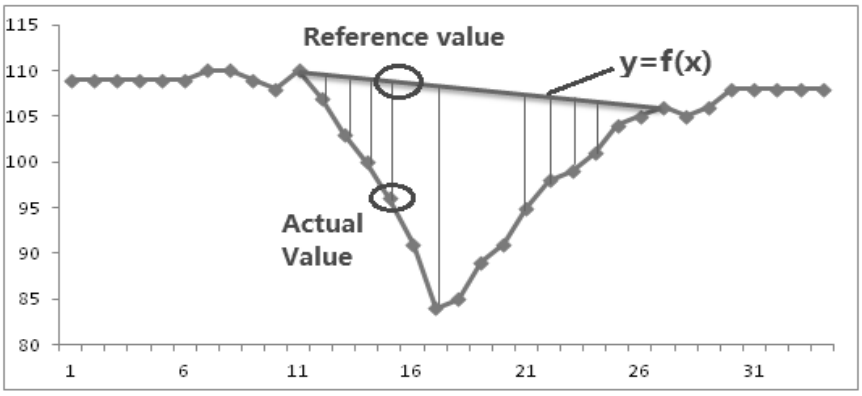

Figure 6.19 The diagram of groove volume calculation

2) Calculate elevation differences between the actual value and the reference value, as illustrated in Figure 6.19, and estimate each groove volume by integrating the elevation difference with the horizontal and lateral resolution, and the mathematical formula can be described in Equation (6.23).

$$\mathrm{V} = \sum_{i=1}^{i=n} (f(x_i) - y_i) * \nabla x \ * \nabla z \qquad (6.23)$$

Where V represent the groove volume, ∇x represent the pixel interval in longitudinal direction, ∇z represent the pixel interval in lateral direction.

6.6 Separation of Joints from Grooves

Typically the identified dips include the grooves and transverse joints. The presence of joints would affect the groove identification results due to the differences of dimensions. Therefore, separating joints from grooves is critical for groove dimension measurement.

6.6.1 Introduction

Studies indicated joints can be discriminated from grooves based on the identified groove depths or/and width (Wang et al, 2003b). However, this approach is conducted on the assumption that the joint has a much larger width or depth than the grooves. But actually most joints might be filled with rubbers, debris, or the loosened aggregators and mortars, it is cumbersome to identify out joints having above-mentioned features. In addition, some joints are sealant out of water penetration that would damage the pavement base and lead to unexpected distress. These facts cause more difficulties in separation of joints and grooves based on groove depth and widths. As a result, the new method should be proposed to address these issues.

Two parameters namely joint spacing and joint window are initiated to separate joints from identified grooves in ProVAL software (Transtec Group, 2012). Joint spacing represents the nominal or designed slab length, and joint window represents a certain tolerance for the nominal slab length. Compared to other joint location algorithm, these two parameters are less prone to the influences of groove width and depth.

6.6.2 Joint Location Method

In this paper, one heuristic joint location method is proposed and its fundamental process procedures are described in Figure 6.20. Upon loading the raw profile data into the application software, the first joint and its location can be automatically identified. In addition, a supplementary manual function is provided to designate the first joint and its location. Once the first joint location has been determined, two variables: Nominal Slab Length (NSL) and Slab Tolerance Length Range (STLR) are introduced in the paper to roughly estimate the possible range of the next joint and assist in determining the Next Joint Location (NeJL) through software application (Transtec Group, 2012).

If there are no dips falling in the possible range of next joint, the Nominal Joint Location (NoJL) is assumed to be at NeJL and the location of the joint is computed as the current joint location (CJL) plus the NSL. If there is only one spike falling in the possible range of next joint, the location of the spike is the NeJL. If there are multiple spikes that fall in possible range of next joint, the one with the largest spacing is taken as the NeJL.

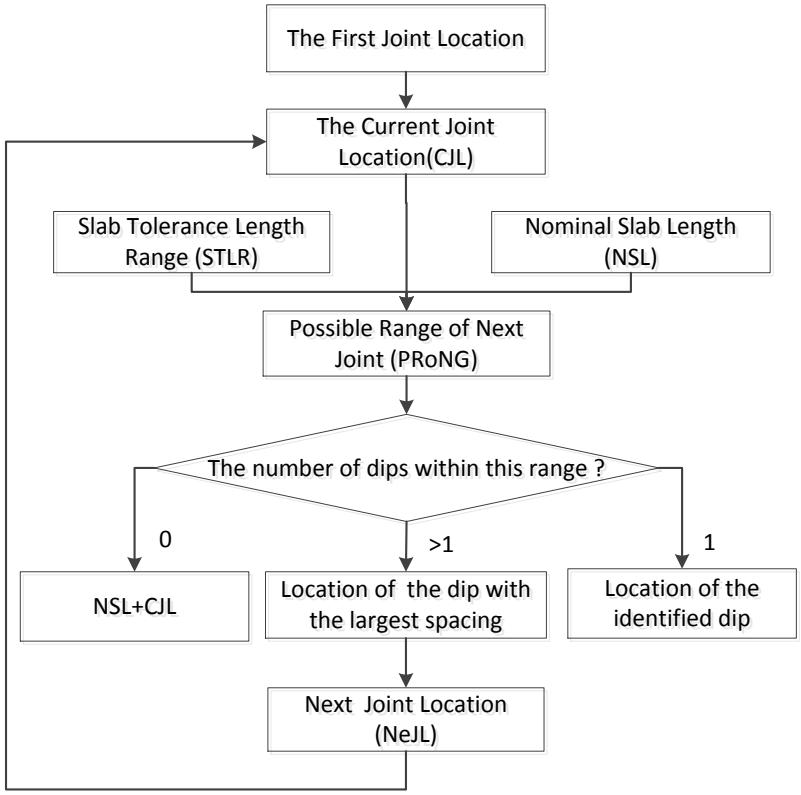

Figure 6.20 Flowchart to separate joints from grooves

6.6.3 Field Test and Validation

In this section the rigid pavement, located on N Husband St in Stillwater OK, is chosen to investigate effects of joint identification method on locating joints. For the 1200ft long segment, there are a number of cracks with various severities but no surface texture finish were constructed. To ensure the data quantity, a 300ft lead-in and lead-out is used, in other words, the 600ft effective test sample spanning over 40 concrete slabs is examined in this experiment. Note that the most slabs have a size of approximately 15ft long by 12ft wide.

Two approaches are used to examine which algorithm is more powerful in locating joints. The first approach is the proposed by authors, and the other one is the downward spike algorithm from PROVAL which is developed to be oriented at one single profile analysis and view. With the purpose of validation, the same profile data, nominal joint spacing and joint window are used when these two approaches are used to identify joints. Table 6.2 list the detailed joint identification results from these two algorithms (Wang et al, 2014).

In light of joint locations produced from these two algorithms, they almost totally match other than several joints that fail to be detected by the downward spike algorithm. All the joints on this test segment can be identified out with the template matched algorithm, and the identified joint locations completely correspond to the joint locations in the field.

Table 6.2 Joint Location Comparison between Two Different Algorithms

ID	Template Matched Algorithm		PROVAL (Downward spike Algorithm)	
	Joint Location	Dip Type	Location Distance (m)	Description
1	1.4	Joint	1.4	Joint
2	5.99	Joint	6	Joint
3	10.57	Joint	10.58	Joint
4	15.18	Joint	15.19	Joint
5	19.76	Joint	19.76	Joint
6	24.35	Joint	24.36	Joint
7	28.92	Joint	N/D (Not Detected)	
8	33.54	Joint	33.56	Joint
9	38.13	Joint	38.15	Joint
10	43.43	Joint	43.84	Joint
11	47.35	Joint	N/D (Not Detected)	
12	52.53	Joint	52.55	Joint
13	56.48	Joint	56.97	Joint
14	60.41	Joint		
15	65.71	Joint	65.73	Joint
16	70.27	Joint	N/D (Not Detected)	
17	74.88	Joint	74.88	Joint
18	79.48	Joint	79.49	Joint
19	84.08	Joint	84.09	Joint
20	88.67	Joint	88.68	Joint
21	93.26	Joint	93.27	Joint
22	98.57	Joint	98.57	Joint
23	102.4	Joint	N/D (Not Detected)	
24	107	Joint	107.04	Joint
25	111.6	Joint	111.65	Joint
26	116.2	Joint	116.22	Joint
27	120.7	Joint	N/D (Not Detected)	
28	126.2	Joint	125.64	Joint
29	130.7	Joint	129.99	Joint
30	135.7	Joint	134.6	Joint
31	140.3	Joint	139.19	Joint
32	144.5	Joint	143.77	Joint
33	148.3	Joint	148.36	Joint
34	153.5	Joint	152.94	Joint
35	157.5	Joint	157.51	Joint
36	162	Joint	162.1	Joint
37	167.2	Joint	169.79	Joint
38	171.2	Joint	N/D (Not Detected)	
39	175.8	Joint	175.87	Joint
40	180.4	Joint	180.88	Joint

6.7 Groove Performance Evaluation

Groove performance evaluation results would help decision-makers to make a decision whether a series of maintenance and rehabilitation activities should be taken on the test pavement section. If surface groove does not meet the relevant performance requirement, the immediate measures should be taken to ensure traveling, landing, and take-off safety. Currently there are no relevant standards regarding how to conduct groove performance evaluation. In this study two approaches are able to be used for performance evaluation. One evaluation guideline is provided by FAA advisory committee, and the other one is proposed by the author of this dissertation.

6.7.1 FAA Groove Evaluation Guideline

The evaluation guideline provided by FAA advisory committee indicates that each type of the groove has a certain tolerance (FAA, 1997). For standard groove pattern, the depth of groove is 1/4 in. (±1/16 in), the width of the groove is 1/4 in. (+1/16 in, -0 in), and the spacing between groove centers is 1 1/2 in. (-1/8 in, +0 in, as illustrated in Table 6.3.

Table 6.3 Recommended Groove Configuration and Its Tolerance

Groove type	Recommended configuration (inch)		Tolerance (inch)		Acceptable range			
			Lower limit	Upper limit	Unit: inch		Unit: mm	
Rectangular	Depth	1/4	-0.0625	1/16	0.19	0.31	4.76	7.94
	Width	1/4	0	1/16	0.25	0.31	6.35	7.94
	Space	1 1/2	-0.125	0	1.38	1.5	34.9	38.1

For the rectangular grooves, the depth and width of 90 percent or more of the grooves shall not be less than 3/16 in (4.76 mm); the depth and width of 60 percent or more of the grooves shall not be less than 1/4 in (6.35 mm); the depth and width of 10

percent or less of the grooves shall not be more than 5/16 in (7.94mm) (FAA, 1997). This guideline is specially developed for airport runway groove performance evaluation, and thus it is not suitable for highway groove performance evaluation.

However, this evaluation method cannot efficiently reflect the drainage ability of the test grooves. For instance, the groove in Figure 6.21a have the same depths and widths with the groove in Figure 6.21b, so they should have the same performance in accordance with the FAA groove evaluation guideline. But actually the two grooves have the different drainage capacity due to the different groove volumes.

Figure 6.21 Two groove shapes with the same groove width and depth

6.7.2 Groove Volume based Evaluation Method

In Figure 6.21, note that the volume of groove #1 is larger than that of groove #2, which indicates groove #1 takes less time to drain out of the same amount of pavement surface water than groove #2. Therefore groove #1 would produce the better "escape water" capacity than groove #2. This method can better describe the drainage capability of grooves than the groove dimension. As a result, the groove volume based evaluation method is initially used for groove performance evaluation in this paper.

6.8 Case Study for Airport Runway

Two sections are chosen to illustrate implementations of automated groove identification, measurement and evaluation. One section is the XNA airport runway used for transverse groove identification and measurement. The other section is located on I-70 NGCS used for longitudinal groove identification and measurement.

6.8.1 XNA Airport Test Site

Northwest Arkansas Regional Airport (XNA) Runway Construction and Maintenance Program requested WayLink Systems Co. to perform runway and taxiway surface condition survey using the DHDV equipped with the 1mm PaveVision3D (3D Ultra) laser imaging technology. The test runway is newly constructed, with a size of 150ft in width and 8800ft in length (marked in blue), as shown in Figure 6.22.

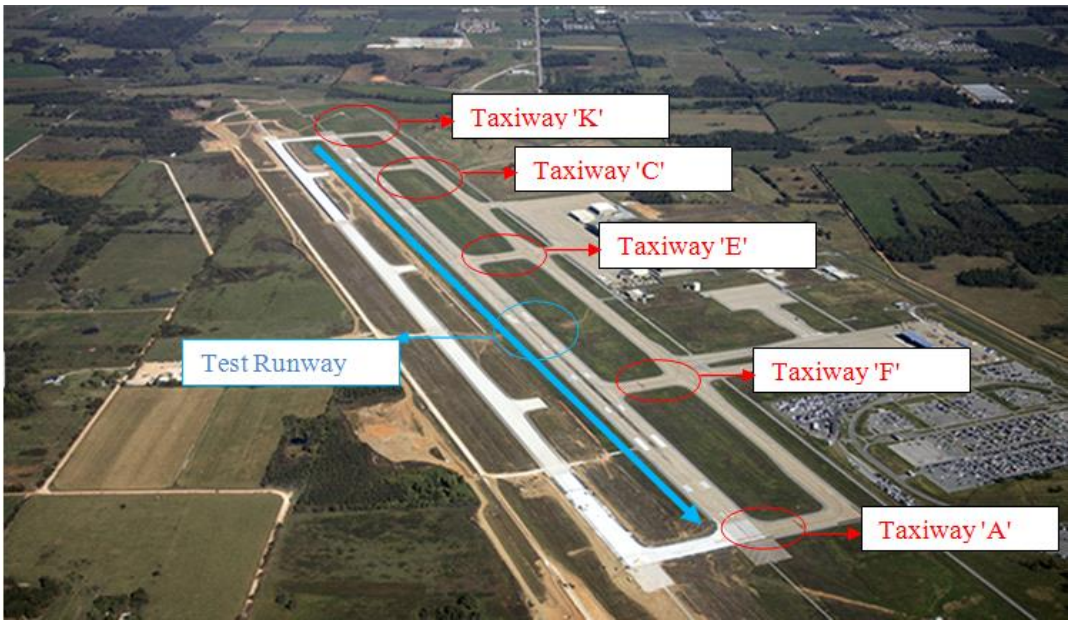

Figure 6.22 Diagram of XNA airport runway and taxiways

The designed groove dimension comply with the relevant FAA guideline that is the constructed groove has a dimension of 1/4-in.-by 1/4-in.-square grooves spaced at 1 1/2 in.

6.8.2 Filter and Algorithm Validation

25 samples on airport runway are randomly chosen to examine which filter and algorithm produce the best groove identification results. The actual groove quantity at each sample is manually counted based on the collected 3D data, which is considered as the ground truth in this study. By comparing the identified groove quantity with the ground truth (GT), the appropriate filter and algorithm that produce the best identification results can be determined.

As shown in Table 6.4, there are four groups of identification results produced by combining each individual filter with each individual algorithm. This four combination methods include the Landing area based filter and Template matched algorithm (LT in short), Landing area based filter and Geometry Contour based algorithm (LG in short), Euler-Bernoulli beam filter and Template matched algorithm (ET in short), and Euler-Bernoulli beam filter and Geometry Contour based algorithm (EG in short).

In Table 6.4, the differences between the actual quantity and the identified groove quantities from these four combos are denoted by Diff (LT), Diff (LG), Diff (ET) and Diff (EG), respectively. If the difference equals to 0, indicating the identified quantity is equivalent to the actual quantity. If the difference is less than 0, it indicates the identified quantity is less than the actual count. In contrast, the identified quantity is more than the actual count if the difference is larger than 0.

Table 6.4 Identification Results with Different Filters and Algorithms

Sample ID	LT	LG	ET	EG	GT	Diff (LT)	Diff (LG)	Diff (ET)	Diff (EG)
1	52.87	51.15	52.88	51.96	52	0.87	-0.85	0.88	-0.04
2	60	59.4	60	58.89	60	0	-0.6	0	-1.11
3	52	51.85	52	52.12	52	0	-0.15	0	0.12
4	58.5	58.42	58.46	58.31	60	-1.5	-1.58	-1.54	-1.69
5	57.98	56.99	57.98	57.26	58	-0.02	-1.01	-0.02	-0.74
6	51.86	51.64	51.87	51.29	53	-1.14	-1.36	-1.13	-1.71
7	61	60.95	61	60.98	61	0	-0.05	0	-0.02
8	50.91	50.56	50.91	51.11	51	-0.09	-0.44	-0.09	0.11
9	60	59.82	60	59.74	60	0	-0.18	0	-0.26
10	52	51.96	52	52.07	53	-1	-1.04	-1	-0.93
11	60	59.32	60	59.48	59	1	0.32	1	0.48
12	60	59.83	60	59.63	59	1	0.83	1	0.63
13	50.99	50.92	50.99	51.15	52	-1.01	-1.08	-1.01	-0.85
14	59.99	59.61	59.99	59.69	60	-0.01	-0.39	-0.01	-0.31
15	49.07	48.58	49.06	48.67	51	-1.93	-2.42	-1.94	-2.33
16	60	59.83	60	59.9	60	0	-0.17	0	-0.1
17	51	50.84	51	51.22	51	0	-0.16	0	0.22
18	60	59.72	60	59.76	60	0	-0.28	0	-0.24
19	60	60	60	59.86	60	0	0	0	-0.14
20	50.99	50.63	50.99	50.92	51	-0.01	-0.37	-0.01	-0.08
21	60.19	59.16	60.26	60.58	60	0.19	-0.84	0.26	0.58
22	50.76	49.62	50.78	50.41	51	-0.24	-1.38	-0.22	-0.59
23	60.99	60.44	60.99	60.16	61	-0.01	-0.56	-0.01	-0.84
24	49.86	49.6	49.93	50.22	50	-0.14	-0.4	-0.07	0.22
25	60.7	59.22	60.78	60.6	60	0.7	-0.78	0.78	0.6

The difference between the identified groove quantity and the ground truth are plotted in Figure 6.23. Even though they do not totally agree with each other, the identified groove quantity are very close to each other for most sample sites.

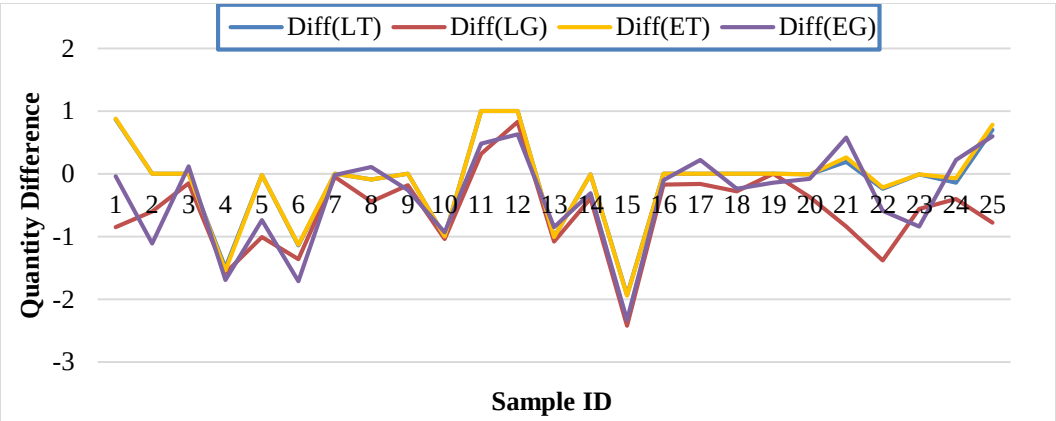

Figure 6.23 Comparison of identified groove quantity and ground truth

Several statistical indices are used to evaluate effects of these four methods on groove identification, as presented in Table 6.5. The mean values are all negative for the four methods, which indicate these four methods underestimated the groove quantity. Also, note that the equivalent mean differences between LT and ET exist, which indicate the identification result is not dependent on the filters if template matched method is used.

Table 6.5 Statistical Analyses of Identification Results from the Four Combo Methods

Statistical Indices	Diff(LT)	Diff(LG)	Diff(ET)	Diff(EG)
Mean	-0.13	-0.60	-0.13	-0.36
STD	0.71	0.89	0.72	0.83
Absolute Mean	0.43	0.69	0.44	0.60
Coefficient of Variation	0.75	1.21	0.75	1.01

It can be found that the template matched algorithm produces the relatively smaller STD than the geometry contour based method. The similar phenomenon is observed for absolute mean values and coefficient of variation as well, which indicate the template matched algorithm has an advantage on groove identification over the contour based method. In addition, the landing area data based filter and Euler-Bernoulli beam filter do

not result in the significant differences of the groove identification results when template match algorithm is used for transverse groove identification. However, there is a significant difference for these two filters if the contour based method is chosen for groove identification.

In summary, the template matched algorithm has the distinct advantage over the contour based algorithm in terms of transverse groove identification. Since there is no significant difference of groove identification results for these two filters, either of them can be used for transverse groove identification. In this study, the Euler-Bernoulli beam filter and template matched algorithm are chosen for the airport runway groove identifications. The groove identification results are described in Figure 6.24.

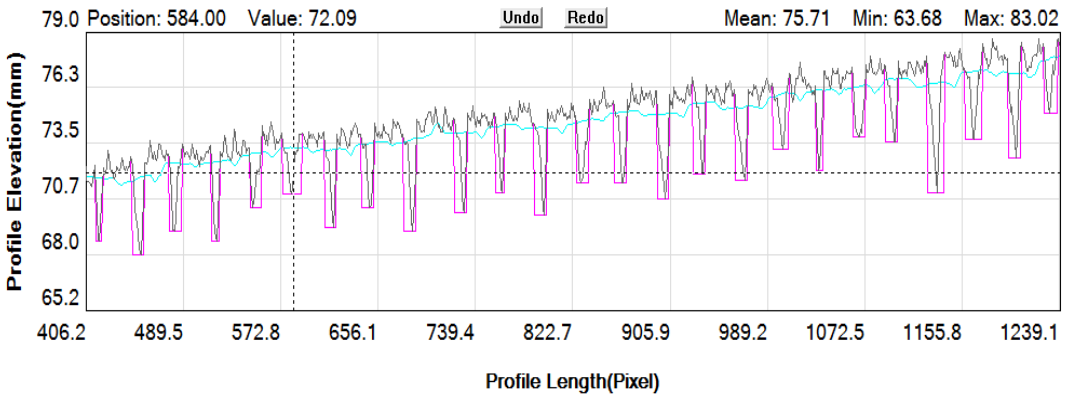

Figure 6.24 Screenshots of groove identification results

6.8.3 Performance Evaluation

XNA airport runway test section is composed of 1164 raw images. Each raw image is served as a sample for runway groove performance evaluation.

6.8.3.1 Groove Dimension Evaluation

The measured groove depths along the test runway are plotted in Figure 6.25, in which the legends L_Gro_Depth and R_Gro_Depth represent the groove depths calculated from the left and right sides of the sample, respectively. The lower limit and upper limit represent the minimum and maximum acceptable values respectively. It is unacceptable for the measured value larger than the upper limit or less than the lower limit. The design value represents the groove standard specified in FAA Advisory Circular No. 150/5320-12C.

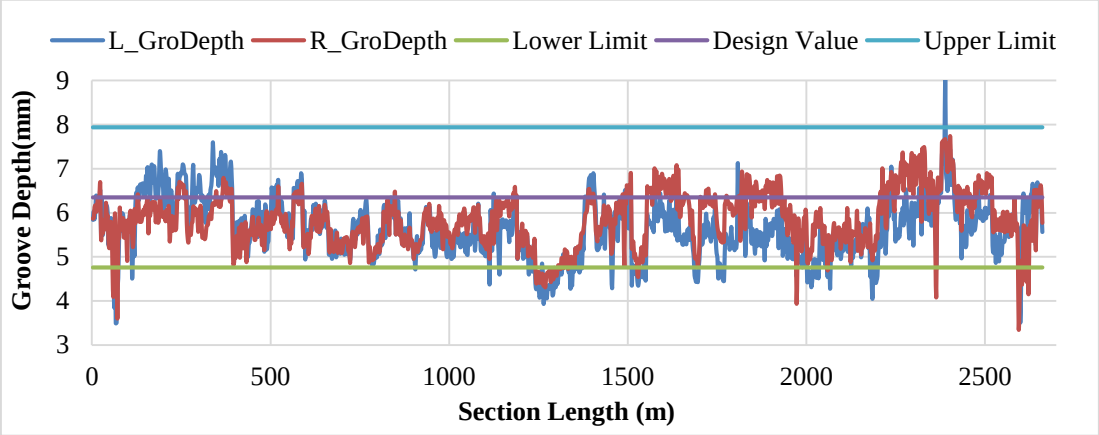

Figure 6.25 Groove depth distribution along XNA airport runway

Note that most groove depths fluctuate along the designed value, and over 90% test samples have the acceptable groove depths. However, the depths of grooves on some segment (e.g. samples #494 to #521) fail to meet the minimum dimension requirement, indicating the potential safety issue may occur within that small segment. To avoid the occurrence of skid-related traffic accident, measures should be taken to correct these runway segments with unacceptable groove depths. The statistical analysis result for

groove depth is presented in Table 6.6. Note that the average value of the measured grooves is 5.74mm, which is 0.6mm difference with the designed values.

Table 6.6 Summary of Groove Dimension and Volume at Runway Test Site

Statistical Summary	Depth(mm)	Width(mm)	Space(mm)	Volume(mm^3)
Average	5.74	6.38	38.09	25.48
STD	0.64	0.20	1.66	3.56
C. O. V	0.11	0.03	0.04	0.14

In addition, the groove width and spacing distribution along test runway are measured as well. The groove width fluctuates along the design value for almost all samples, but less than the upper limit, as presented in Table 6.6. The measured groove spacing is equivalent to the design value. It can be considered that the measured groove spacing is consistent along test section based on the trivial coefficient of variations (e.g. 0.04).

6.8.3.2 Groove Volume Evaluation Results

Figure 6.26 shows the groove volume distribution along runway test. The lower limit of the acceptable groove volume is 30.23 mm^3, which is computed as the product of the lower limit of groove depth by the design value of groove width. The design value of groove volume is 40.32 mm^3, which is computed as the product of the design groove width by the design groove depth. Note that the measured groove volume is less than the acceptable value, which might be caused by the loosened aggregates, mortar, and debris that falls in the grooves, as shown in Table 6.6. In this case it is presumed that the data interval in both lateral and horizontal direction is 1mm.

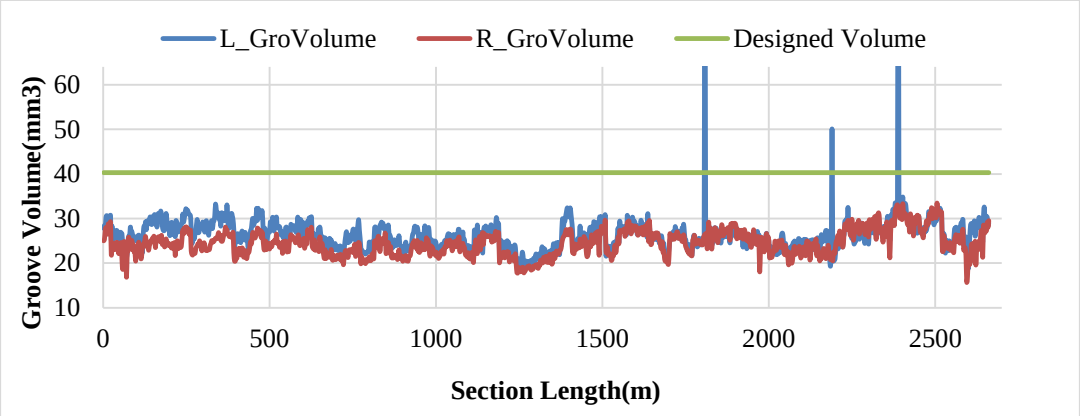

Figure 6.26 Groove volume along XNA airport runway

In addition, the Groove Volume Index (GVI) is proposed to represent the proportion of the measured groove volume relative to the design volume. In this study the GVI of 75% is used as the acceptable ratio, which is determined based on the standard groove depth and its tolerance. Generally pavement groove can be considered in good condition if the GVI is no less than 75%. It can be observed that almost the entire section has the GVI values less than the acceptable ratio, indicating the pavement volume does not satisfy the lowest safety performance requirement, as shown in Figure 6.27.

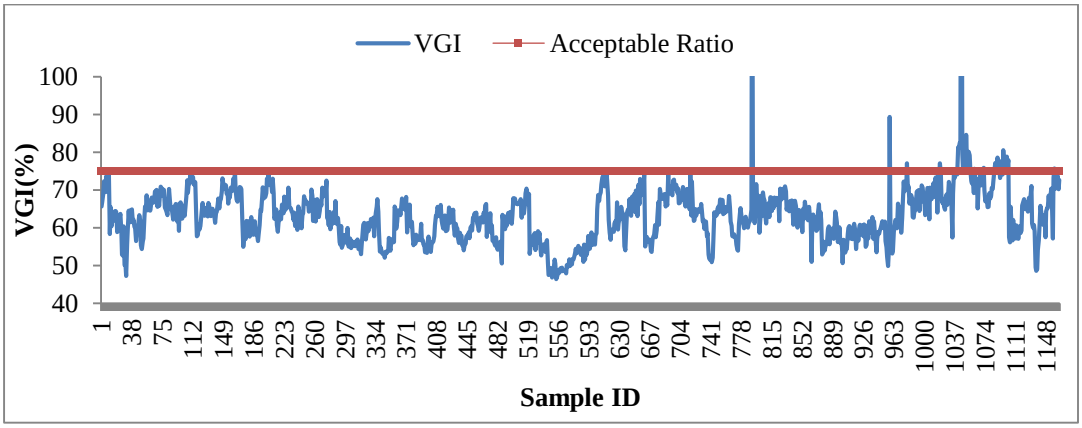

Figure 6.27 Comparison of GVI and acceptable reference value

In summary, the XNA airport runway has the acceptable safety performance base on the groove evaluation guidelines provided by FAA advisory committee. Unfortunately, the measured groove volumes are less than the acceptable volume value (30.23 mm^3), and the estimated GVIs are less than the acceptable volume ratio as well, which indicates the XNA runway groove might be padded with pavement debris or loosened aggregates and mortars, and not efficient for rapid discharge of the rainy water on the pavement surface during wet weather.

Based on evaluation results from these two approaches, two measures can be taken immediately to correct the existing groove performance issues. The first corrective activity is to increase groove depths at runway locations from samples #494 to #531 and to ensure groove depths is above the lower limit of acceptable range. The second activity is to sweep away the surface debris or loosened aggregates inside grooves and to ensure runway surface grooves have the good drainage ability during wet weather.

6.9 Case Study for Highway I-70

6.9.1 I-70 NGCS Test Site

Seven experimental sections with various surface textures, located on I-70 near Abilene Kansas, are constructed by Kansas Department of Transportation (KDOT) aiming to investigate the tire-pavement noise levels of these textures. As described in Figure 6.28(a), the test section starts with the longitudinal tining constructed per the KDOT standards, followed by is longitudinal grooving, astro-truf drag, astro-turf drag plus longitudinal grooving, conventional diamond grinding, Next Generation Concrete Surface, and Exposed Aggregate. The total section has a length of 4250m (13943ft), and

each test section is 800 m (2624ft) long except for the last texture experiment section having a length of 1250 m (3750ft).

In this study the NGCS texture section is chosen to illustrate implementations of longitudinal groove identification, measurement, and evaluation. Since each collected 3D image has a length of 2.286m (7.5ft), so the test section consists of consecutive 350 images. Figure 6.28(b) indicates a close up of the actual NGCS texture. The constructed groove is 11/32 inches (8.73 mm) in depth and spaced approximately 5/8 inches (15.88mm) apart. The groove width can be roughly estimated by the ruler in Figure 6.28(b), with a value of 4mm.

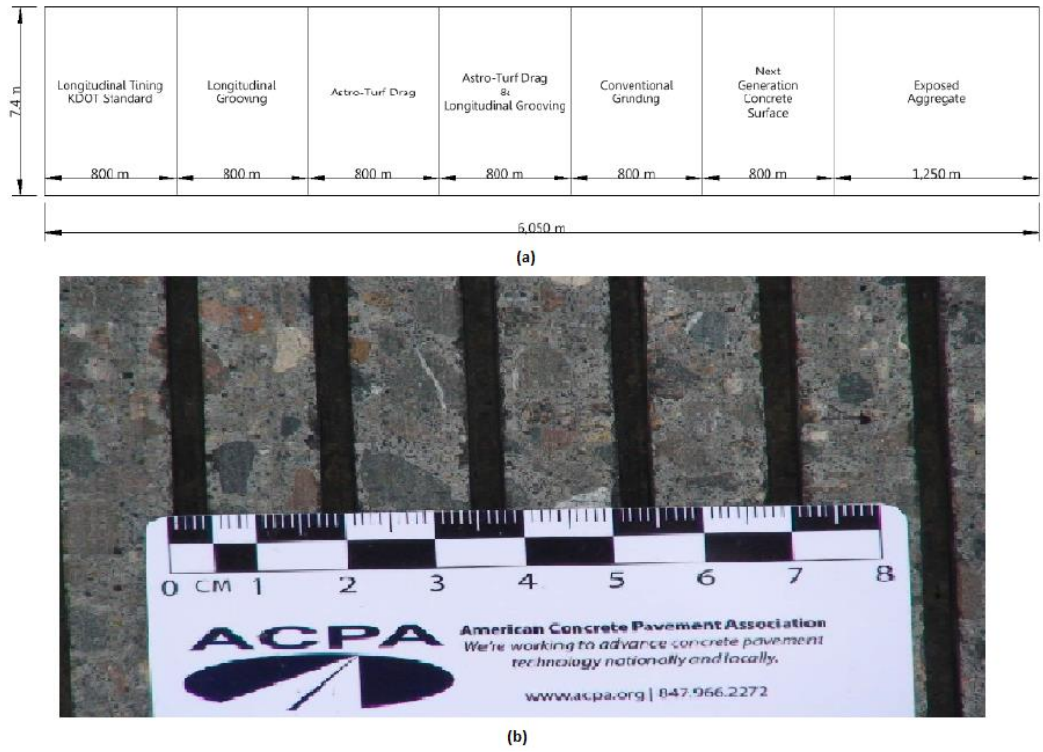

Figure 6.28 Photographs of (a) construction layout of I-70 surface textures; (b) close up of NGCS texture with a ruler

6.9.2 Filter and Algorithm Validation

Likewise 25 test samples are continuously chosen to determine which filter and algorithm is more efficient in identifying longitudinal grooves. The ground truth (GT) is manually counted from test specimen. As presented in Table 6.7, each combo (e.g. LT, LG, ET, or EG) method produces one group of identification result. The differences between the actual and the identified groove quantities are presented in Table 6.7 as well.

As aforementioned, Diff (LT) denotes the difference between the ground truth and the identified groove quantity with LT combo method, the same name convention applies to other three combo methods namely Diff (LG), Diff (ET), and Diff (EG). The negative difference indicates the identified groove quantity is less than the ground truth, while the positive difference indicates the identified groove quantity is overestimated.

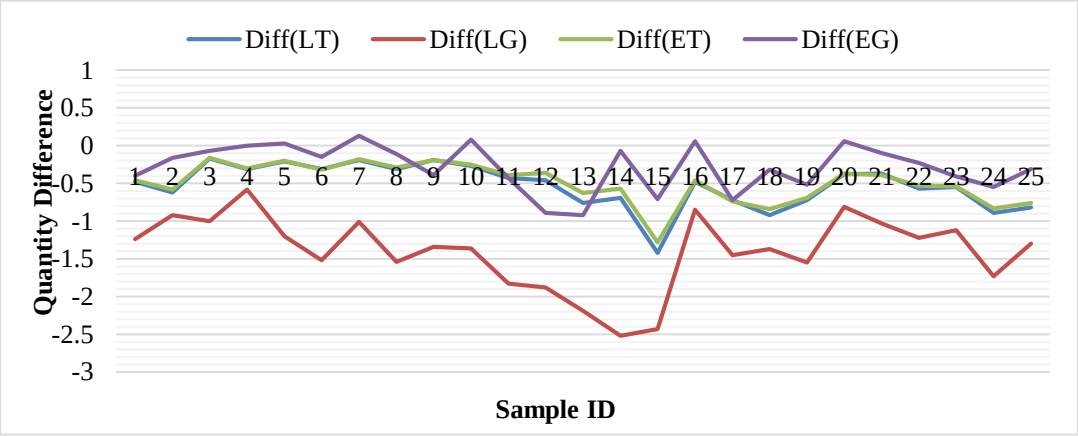

Figure 6.29 Groove quantity difference between GT and other methods

Figure 6.29 is used to intuitively illustrate differences between the identified groove quantities with the ground truth. In this case the LG combo method produces the largest

errors in longitudinal groove identification, followed by are the LT and ET combination methods. The EG combination method produce the best identification result.

Table 6.7 Results from the Four Combo Methods at NGCS Test Site

Sample ID	LT	LG	ET	EG	GT	Diff (LT)	Diff (LG)	Diff (ET)	Diff (EG)
1	54.52	53.76	54.54	54.6	55	-0.48	-1.24	-0.46	-0.4
2	54.38	54.08	54.42	54.84	55	-0.62	-0.92	-0.58	-0.16
3	54.83	54	54.84	54.93	55	-0.17	-1	-0.16	-0.07
4	54.69	54.42	54.7	55	55	-0.31	-0.58	-0.3	0
5	54.79	53.8	54.8	55.03	55	-0.21	-1.2	-0.2	0.03
6	54.69	53.48	54.68	54.85	55	-0.31	-1.52	-0.32	-0.15
7	54.81	53.99	54.82	55.13	55	-0.19	-1.01	-0.18	0.13
8	54.69	53.46	54.71	54.89	55	-0.31	-1.54	-0.29	-0.11
9	54.81	53.66	54.81	54.61	55	-0.19	-1.34	-0.19	-0.39
10	54.73	53.64	54.75	55.08	55	-0.27	-1.36	-0.25	0.08
11	54.57	53.17	54.61	54.57	55	-0.43	-1.83	-0.39	-0.43
12	54.54	53.12	54.64	54.11	55	-0.46	-1.88	-0.36	-0.89
13	54.24	52.81	54.37	54.08	55	-0.76	-2.19	-0.63	-0.92
14	54.31	52.48	54.43	54.93	55	-0.69	-2.52	-0.57	-0.07
15	53.58	52.57	53.72	54.29	55	-1.42	-2.43	-1.28	-0.71
16	54.52	54.15	54.54	55.06	55	-0.48	-0.85	-0.46	0.06
17	54.28	53.55	54.26	54.28	55	-0.72	-1.45	-0.74	-0.72
18	54.08	53.63	54.16	54.68	55	-0.92	-1.37	-0.84	-0.32
19	54.28	53.45	54.31	54.48	55	-0.72	-1.55	-0.69	-0.52
20	54.62	54.19	54.63	55.06	55	-0.38	-0.81	-0.37	0.06
21	54.63	53.97	54.61	54.9	55	-0.37	-1.03	-0.39	-0.1
22	54.43	53.78	54.47	54.77	55	-0.57	-1.22	-0.53	-0.23
23	54.45	53.88	54.46	54.59	55	-0.55	-1.12	-0.54	-0.41
24	54.11	53.27	54.17	54.45	55	-0.89	-1.73	-0.83	-0.55
25	54.18	53.7	54.24	54.69	55	-0.82	-1.3	-0.76	-0.31

The optimal filter and algorithm are determined based on statistical analysis results, as described in Table 6.8. Among these four combo methods, the EG has the smallest differences, depending on the mean value, the standard deviation, the absolute mean value, and coefficient of variation, followed by is the LT and ET combo methods. The

LG has the worst identification results among these four methods. Therefore, EG method is considered as the most efficient combo method for longitudinal groove identification.

Table 6.8 Statistical Analysis of Identification Results from the Four Combo Methods

Statistical Index	Diff(LT)	Diff(LG)	Diff(ET)	Diff(EG)
Mean	-0.53	-1.40	-0.49	-0.28
STD	0.60	1.48	0.56	0.41
Absolute Ave	0.53	1.40	0.49	0.31
Coefficient of Variation	1.81	2.87	1.87	1.14

6.9.3 Performance Evaluation

The NGCS segment consisting of 350 raw images is used for longitudinal groove performance evaluation. Each 3D image with a length of 2.286 m (7.5ft) is served as a sample for data process and analysis. The legends from Figure 6.30 to Figure 6.33 have the same name convention with the legends presented in Section 6.7.3. The groove dimension and volume are calculated based on the identified grooves.

6.9.3.1 Groove Dimension Evaluation Results

Figure 6.30 shows the groove depth distribution versus NGCS sections. The KDOT specifies the designed groove should have a depth of 8.73mm. The measured groove depths fluctuate along the design value for most segments, with the exception of the segment from 320m to 420 m, in which the measured groove depth is around 7.5mm.

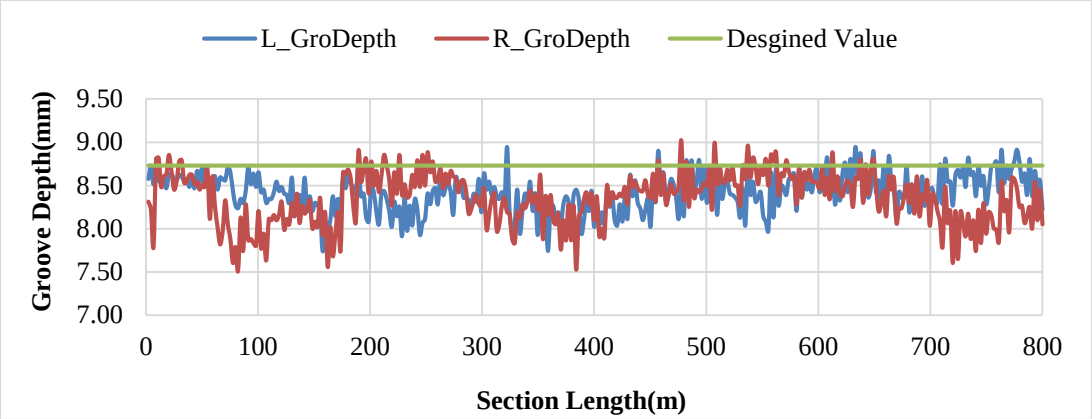

Figure 6.30 Groove depth distribution versus section length

As per the groove depth tolerance range provided FAA practice, the acceptable depth range for NGCS should be located at [7.14mm,10.32mm], which indicate the measured groove depths are larger than the minimum acceptable range with no exceptions. Also, Table 6.9 shows the average depth of the measured grooves is 8.39 that is 0.34mm smaller than the standard groove depth.

Table 6.9 Summary of Groove Dimension and Volume at Highway Test Site

Statistical Analysis	Depth	Width	Spacing	Volume
Average	8.39	4.04	15.90	30.73
STD	0.26	0.06	0.05	1.28
Coefficient of Variation	0.03	0.01	0.00	0.04

The measured groove width and spacing are plotted along the NGCS section, as shown in Figure 6.31 and Figure 6.32 respectively. It can be observed that the width and space is evenly distributed along the designed value. As Table 6.9 shows, the variation coefficients and the standard deviation for these two parameters are no more than 0.01 and 0.06 respectively, which indicate the measured groove width and spacing are consistent along NGCS section and have a good agreement with the design values.

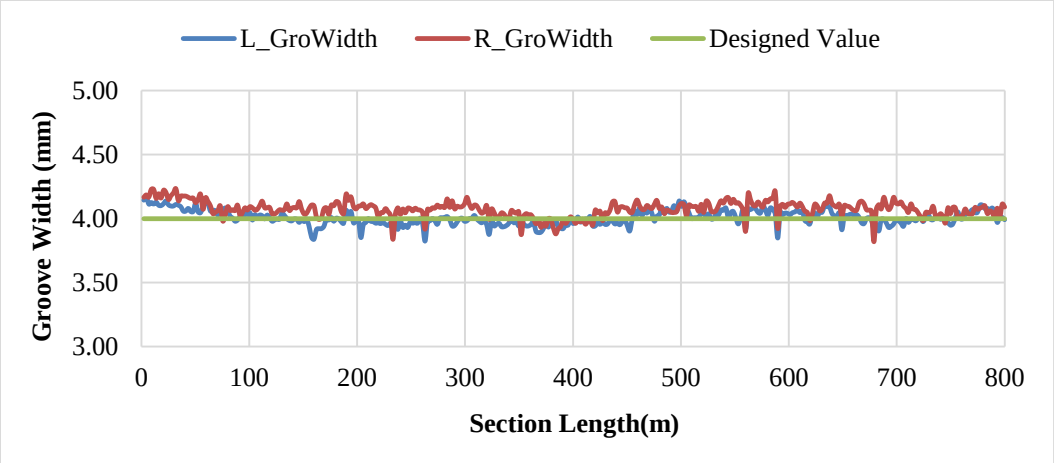

Figure 6.31 Groove width distribution versus section length

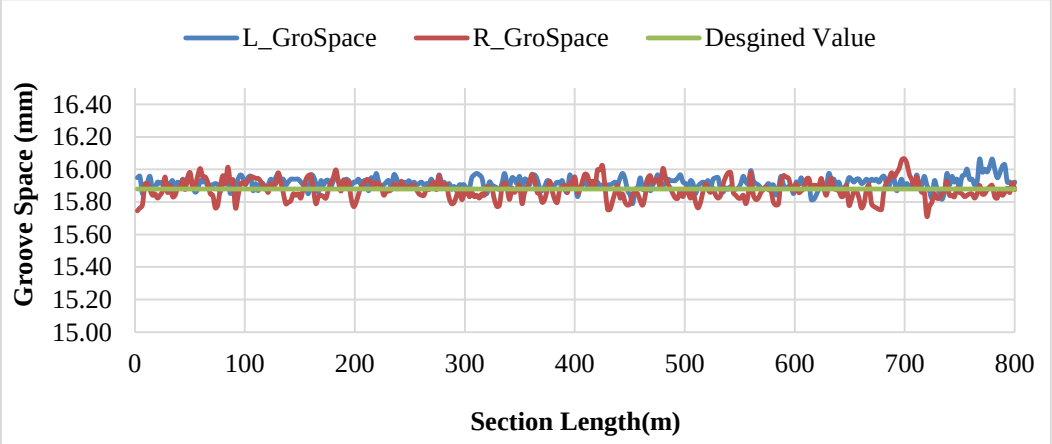

Figure 6.32 Groove space distribution versus section length

6.9.3.2 Groove Volume Evaluation

As Figure 6.33 shows, the measured groove volumes are below the reference volume with a value of 34.92 mm^3, but they are much closer to the reference volume for most segments, with two exceptional segments from 80 m to 180 m and from 320m to 420 m.

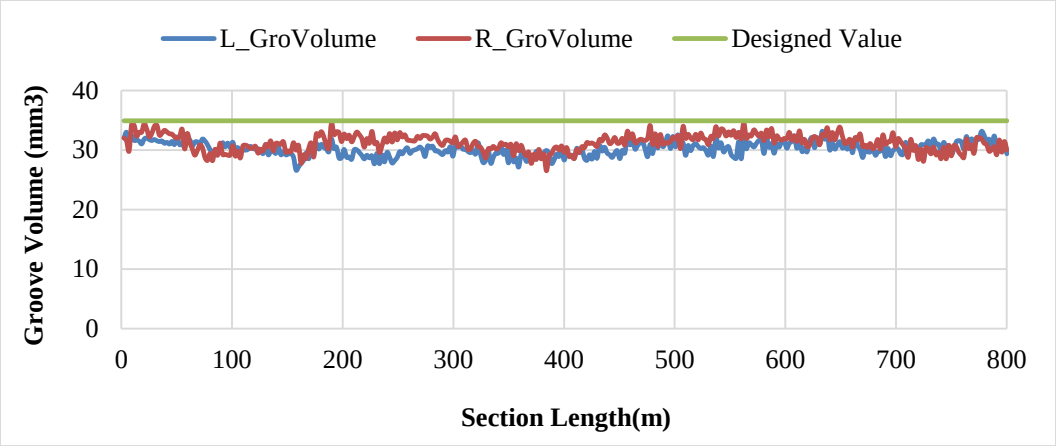

Figure 6.33 Groove volume distribution versus section length

The GVI, as an important component of volume based evaluation method, is used to disclose groove drainage capability. Based on the groove configuration and its tolerance, the reference groove volume index can be calculated with a value of 75%. Figure 6.34 shows the measured GVI along the test section, it can be observed that all measured GVIs are above the acceptable ratio or reference GVI, indicating the measured grooves have a good drainage capacity during wet weather.

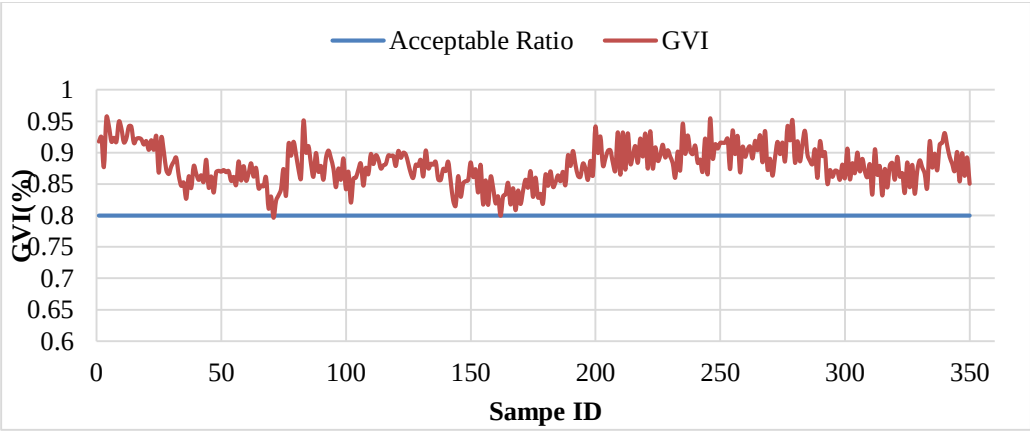

Figure 6.34 Comparison of GVI and the acceptable reference value

In summary, NGCS test section still has a good groove performance based on the measured groove dimension and volume after several years of in-service. There is no further corrective measures taken on this tests section.

6.10 Summary

The groove-related studies are investigated in this chapter. Firstly, longitudinal and transverse grooves are presented, which are broadly used to prevent traffic accidents by increasing surface frictional properties and reducing the potential hydroplaning risks. Two case studies are provided to help demonstrate implementations of automated groove identification, measurement, and evaluation. One case study is regarding the transverse groove performance evaluation conducted on XNA airport runway test section, and the other case study is regarding the longitudinal groove performance evaluation conducted on the I-70 NGCS test section.

Secondly, three data filtering techniques are designed and used to suppress impacts of narrow dips on the filtered profiles which are critical for the implementation of groove identification algorithms. Mask filter is easy to implement, but it is hard to determine the proper base length to eliminate influences of narrow dips. Landing area data based filter and Euler-Bernoulli beam filter are much powerful in suppressing effects of narrow dips on filtered profiles than mask filter.

Followed by is that three algorithms are developed for groove identification based on the filtered data. The gradient based method is proposed for identifying a pair of extreme points where the slope or gradient varies fastest, and subsequently the three basis points (starting, ending, and the deepest point of one groove) of the groove can be located based

on the pair of extreme points. Although this method can be used for groove identification, the results are not as good as those from the other two methods: the template matched algorithm and geometry contour based method. Both of them are oriented at finding the deepest point within the groove, and subsequently determining the starting and ending point of one groove with transversal methods. The findings indicate the template matched algorithm is more robust in transverse groove identification, whilst the geometry contour based algorithm are much powerful in longitudinal groove identification.

Thirdly, two groove evaluation approaches are presented: one is to calculate and evaluate groove dimension based on FAA calculation practice, the other one is to calculate and evaluate groove volume based on the newly proposed calculation principle. To ensure the reliability of measurement results, the multiple profiles are used in lieu of the one-sight-line profile for groove dimension measurement. In addition, one heuristic based joint location technique is also presented to separate the joints from identified grooves, which aims to eliminating effects of joints on groove performance evaluation.

Finally, two case studies are presented to demonstrate the implementation of proposed filters, algorithms, and evaluation approaches. Results indicate the techniques are powerful in accurately identifying grooves, calculating groove dimension, and evaluating groove performances, no matter what groove types are investigated.

CHAPTER 7. CONCLUSIONS AND RECOMMENDATIONS

7.1 Conclusions

The dissertation presents a thorough study on the evaluation of pavement safety based on 1mm 3D pavement surface texture collected from DHDV with PaveVision3D Ultra system. The methodologies and findings in the dissertation would be beneficial in the continuous measurement and evaluation of pavement safety for the project- and network-level pavement surveys.

Firstly signal and image processing techniques are applied to preprocess the raw 3D texture data so that the processed data can be served as the basis for the subsequent data analyses. The data preprocessing technologies in CHAPTER 3 include height difference reduction approach, invalid data repair techniques, unwanted information removal techniques, as well as the data sampling principle. Results indicated the proposed methodologies are powerful in suppressing the unwanted noises and errors, which are critical for the following pavement safety evaluation.

CHAPTER 4 presents several surface texture indicators to characterize surface properties, based on which surface safety can be evaluated. Aside from the widely used MPD, MTD, and RMS, the Skewness and Kurtosis are firstly utilized to reveal the distribution of surface heights. Skewness reveals the predominance of peaks or valleys, and Kurtosis reveals the presence of extreme peaks or dips on the test surface. Findings indicate the negative Skewness and the large kurtosis can be used as good pavement frictional property parameters since the negative Skewness indicate the rapid water runoff under rubber tires and a large kurtosis value indicate the increase of the tire penetration depth into pavement surface.

Texture aspect ratio can represent the presence of isotropic or anisotropic surface texture, and texture direction is used to imply the predominant direction of anisotropic surface, especially for artificially textured pavements. Isotropic texture produces quieter pavement surface than isotropic texture. Texture direction also relates to the pavement frictional properties. Surface areal ratio and surface bearing index are employed to describe the surface wearing capacity and frictional properties. Generally the larger the surface areal ratio and surface bearing ratio are, the better the frictional property it has. In this study the relations among different texture indicators are investigated as well, and the findings indicate pavement friction can be estimated with the following three texture indicators namely Skewness, surface aspect ratio, and surface bearing ratio.

CHAPTER 5 presents the use of Heinrich/ Klüppel rubber friction theory on pavement friction prediction with 1mm 3D texture data. Heinrich/ Klüppel model is constituted of three components: surface roughness, tire properties, and elastic contact

between rubber tires and pavement surface. In order to describe surface roughness, the fractal dimension analysis (e.g. box counting method) and height difference correlation function are used to calculate the three texture descriptors (e.g. Hurst Exponent, height difference correlation length parallel and vertical to surface). To model rubber properties, the Zener slider model is used to simulate the viscoelastic behaviors of rubber tires and the complex modulus is used. To represent the actual contact area of rubber tires and pavement surface, the Greenwood-Williamson model is used to calculate the tire penetration depth. Moreover, the Fourier Transform is used to calculate the power spectral density at various wavelengths. As a result, the pavement friction can be estimated based on the Heinrich/ Klüppel model. Findings indicate a good agreement between the predicted and measured FNs is observed.

CHAPTER 6 presents the comprehensive study on automated groove identification, measurement, and evaluation. To identify the potential dips inclusive of grooves and joints, three filters and three identification algorithms are developed. Comparison and validation indicated the landing area data based filter and Euler-Bernoulli beam filter have pronounced advantage over the mask filter in suppressing the effects of narrow dips on filtered profile, based on which the identification algorithms are used to identify the location of potential dips. Findings indicate template matched algorithm and geometry contour based algorithm produce better identification results than the gradient based algorithm.

Once the potential dips are located, the dip dimensions can be calculated in accordance with FAA AC 150-5320-123C based on multiple profiles. In addition, dip

volume can be estimated as well based on the proposed method. In order to separate the identified joints from grooves, one heuristic method is used. Finally groove safety performance can be evaluated under two scenarios: groove dimension based method and groove volume based method. Results indicate these techniques proposed in this paper are robust and powerful in identifying grooves, calculating groove dimension, and evaluating groove performances on transversely and longitudinally grooved pavements.

7.2 Recommendations

For the purpose of the project- and network- level safety surveys, more field validation work need to be conducted on various AC pavements to improve the reliability of the model, and they can be implemented as follows:

1) Data processing techniques need to be further investigated to remove the noises of texture data, determine the wavelengths of interest, and calculate the related parameters used in Heinrich/Klüppel model;
2) The initialization of the variables needs to be validated, such as the modulus of the rubber block and the tire pressure.
3) The texture data resolution is highly associated with the prediction of pavement frictions, and thus the high resolution data in both vertical and horizontal directions is necessary.

In addition, a comprehensive software are recommended to be developed and it should cover the four contents of pavement safety evaluation: calculation of surface texture indicators and their application on pavement friction predication, pavement friction prediction with Heinrich/ Klüppel model on AC pavements, groove performance

evaluation on grooved pavements, and hydroplaning speed prediction on both AC and PCC pavements.

REFERENCES

Abe, H., Tamai, A., Henry J. J. and Wambold, J., 2001. Measurement of Pavement Macro texture with Circular Texture Meter, *Transportation Research Record 1764 Paper No. 01-3519.*

Ahammed, M. Alauddin, Tighe, Susan L., 2008. Pavement Surface Mixture, Texture and Skid Resistance: A Factorial Analysis. *Airfield and Highway Pavements*, pp 370-382.

Alvarez, L. & J. M Morel, 1994. Formalization and computational aspects of image analysis, *Acta Numerica*, 3, pp1–59.

American Society for Testing and Materials (ASTM), 2011. ASTM E 274: Standard Test Method for Skid Resistance of Paved Surfaces Using a Full-Scale Tire, *ASTM Standard Practice E 274 Book of ASTM Standards*, Volume 04.03 Philadelphia, P A.

American Society for Testing and Materials (ASTM), 2011. ASTM E 303: Standard Test Method for Measuring Surface Frictional Properties Using a British Pendulum Tester, *ASTM Standard Practice E 303 Book of ASTM Standards*, Volume 04.03 Philadelphia, P A.

American Society for Testing and Materials (ASTM), 2011. ASTM E 867: Standard Terminology Relating to Vehicle-Pavement Systems, *ASTM Standard Practice E 867 Book of ASTM Standards*, Volume 04.03 Philadelphia, P A.

American Society for Testing and Materials (ASTM), 2011. ASTM E 965: Standard Test Method for Measuring Pavement Macro texture Depth Using a Volumetric Technique, *ASTM Standard Practice E 965 Book of ASTM Standards*, Volume 04.03 Philadelphia, P A.

American Society for Testing and Materials (ASTM), 2011. ASTM E 1845: Calculating Pavement Macro texture Profile Depth, *ASTM Standard Practice E 1845 Book of ASTM Standards,* Volume 04.03 Philadelphia, P A.

American Society for Testing and Materials (ASTM), 2011. ASTM E 1911: Standard Test Method for Measuring Paved Surface Frictional Properties Using Dynamic Friction Tester, *ASTM Standard Practice E 1911 Book of ASTM Standards*, Volume 04.03 Philadelphia, P A.

American Society for Testing and Materials (ASTM), 2011. ASTM E 1960: Standard Practice for Calculating International Friction Index of a Pavement Surface, *ASTM Standard Practice E 1960 Book of ASTM Standards,* Volume 04.03 Philadelphia, P A.

American Society for Testing and Materials (ASTM), 2011. ASTM E 2157: Standard Test Method for Measuring Pavement Macro texture Properties Using the Circular Track Meter, *ASTM Standard Practice E 2157 Book of ASTM Standards*, Volume 04.03 Philadelphia, P A.

American Society for Testing and Materials (ASTM), 2011. ASTM E 2380: Standard Test Method for Measuring Pavement Texture Drainage Using an Outflow Meter, *ASTM Standard Practice E 2380 Book of ASTM Standards,* Volume 04.03 Philadelphia, P A.

ASME, 2009. Surface Texture (Surface Roughness, Waviness, and Lay). ASME B46.1, *American Society of Mechanical Engineers,* Three Park Avenue, New Work, NY.

Bartlett, ML. 1991 Comparison of methods for measuring fractal dimension. *Australia's Phys Eng Sci Med*. 14(3):146-52.

Beaton, J. L.; Zube, E.; Skog, J. 1969. Reduction of accidents by pavement groovings. *Special Rep. No. 101*, Highway Research Board, Washington, D.C., 110–125.

Carr, J.R., Norris, G.M. and Newcomb, D.E., 1990. Characterization of aggregate shape using fractal dimension, *TRB, 69th Annual Meeting*, Washington DC.

Carr, J.R.,Mirsa, M., and Litchfield,J.,1992.Estimating surface area for aggregate in the size range: one millimeter or larger, *TRB, 71st Annual Meeting*, Washington DC.

Chambers, Joseph R., 2003. Concept to Reality: Contributions of the NASA Langley Research Center to U.S. *Civil Aircraft of the 1990s*, NASA sp-2003-4529, 2003.

Choubane, B., Holzshuher, C.R., and Gokhale, S., 2003. Precision of Locked Wheel Testers for Measurement of Roadway Surface Friction Characteristics, *Research Report FL/DOT/SMO/03-464*. State Materials Office, Florida.

Design Manual for Roads and Bridges (DMRB), 2004. Pavement Design and Maintenance, *Pavement Maintenance Assessment*, Volume 7, Section 3, Part 1, HD 28/04, The Highways Agency, Scottish Executive, Welsh Assembly Government, The Department for Regional Development Northern Ireland.

Do, M.T., Marsac, P., Delanne, Y., 2004. Prediction of tire/wet road friction from road surface microtexture, and tire rubber properties. In: *5th International Symposium on Pavement Surface Characteristics*, Toronto.

Ergun, M.D., Lyinam Sukriye, Lyinam A.F.., 2005. Prediction of Road Surface Friction Coefficient Using only Macro- and Micro texture Measurement, *Journal of Transportation Engineering*, pp311-319.

Federal Aviation Administration (FAA), 1997. Measurement, Construction and Maintenance of Skid-resistant Airport Pavement Surfaces, *FAA AC 150/5320-12C*, U.S. Department of Transportation, Washington, D.C.

Flintsch, G. W., de León, E., McGhee K., and Al-Qadi I. L., 2003. Pavement Surface Macro texture Measurement Applications, In *Transportation Research Record: Journal of the Transportation Research Board, No. 1860*, Transportation Research Board of the National Academies, Washington, D.C., pp168-177.

Flintsch, G. W., Huang, M., and McGhee, K., 2005. Harmonization of Macro texture Measuring Devices, *Journal of ASTM International*, Volume 2, No. 9, 1-12.

Fwa, T. F, Choo, Y. S., and Liu, Y., 2003. Effect of Aggregate Spacing on Skid Resistance of Asphalt Pavement, *Journal of Transportation Engineering*, American Society of Civil Engineers, Volume 129, No. 4, 420-426.

Gendy, Amin EI and Ahmed Shalaby, 2007. Mean Profile Depth of Pavement Surface Macro texture Using Photometric Stereo Techniques, *Journal of Transportation Engineering*, Volume 133, No. 7, 2007, pp433–440.

Gere, J. M. and Timoshenko, S. P., 1997. Mechanics of Materials, *PWS Publishing Company*.

Gonzalez, Rafael C. 2009. Digital image processing. Pearson Education India.

Grady, J. E., and Chamberlin, W. P., 1981. Groove-Depth Requirements for Tine-Textured Pavements, *Journal of the Transportation Research Board*, Washington D.C., Transportation Research Record, No. 836, 67-76.

Greenwood, J.A. and Williamson, J.B.P., 1966. Contact of nominally flat surfaces. *Proc. R. Soc. Lond. A.*, 295(1442):300 – 319.

Hall, J. W., Smith, K. L., Titus-Glover, L., Wambold, J. C., Yager, T. J., and Rado, Z.; 2009. Guide for Pavement Friction. *Final Report for NCHRP Project 01-43*,

National Cooperative Highway Research Program (NCHRP), Transportation Research Board of the National Academies, Washington, D.C.

Harwood, D.W.; Blackburn, R.R.; Heenan, P.J., 1978. Effectiveness of alternative skid reduction measures, Vol. IV. Criteria for Improvement Surface Macrotexture, *FHWA-RD-79-25 Final Report*.

Henry, J. J., 1983. Comparison of Friction Performance of a Passenger Tire and the ASTM Standard Test Tires, *ASTM STP 793 American Society for Testing and Materials (ASTM)*, Philadelphia, Pennsylvania.

Henry, J. J., 2000. Evaluation of Pavement Friction Characteristics, *NCHRP Synthesis 291*, National Cooperative Highway Research Program (NCHRP), Washington, D.C.

Horne, Walter B.; Leland, Trafford J.W. 1962. Influence of tire tread pattern and runway surface condition on braking friction and rolling resistance of a modern aircraft tire, *NASA TN D-1376*, 1962.

Horne, W.B., and Tanner, J. A. 1969. Joint NASA-British Ministry of Technology Skid Correlation Study: Results from American Vehicles: Pavement Grooving and Traction Studies, *NASA SP-5073, National Aeronautics and Space Administration*, Washington DC., pp325-360.

Horne, W.B., Buhlmann, F., 1983. A Method for Rating the Skid Resistance and Micro/macro-texture Characteristics of Wet Pavements. In*: Frictional Interaction of* Tire and Pavement, pp. 191e218. ASTM STP 793.

Hoerner, T. E., Smith, K. D., Larson, R. M., and Swanlund, M. E., 2003. Current Practice of PCC Pavement Texturing, *Transportation Research Board 2003* Annual Meeting CD-ROM.

Hui, C.Y.; Lin, Y.Y., and Baney, J.M. 2000. The mechanics of tack: Viscoelastic contact on a rough surface. *J POLYM SCI B-POLYM PHYS*, 38(11):1485 – 1495.

International Standards Organization (ISO), 1998. Characterization of Pavement Texture using Surface Profiles – Part 1: Determination of Mean Profile Depth, *Acoustics, ISO Standard 13473*, International Standards Organization, Geneva, Switzerland.

Janoo, V.C., and Horhonen C, 1999. Performance Testing of Hot-Mix Asphalt Aggregates, *Special Report 99-20*, U.S. Army Corps of Engineers Cold Regions Research & Engineering Laboratory.

Karamihas, S. M. (2005). Critical profiler accuracy requirements.

Kebrle, J., Walker, R., 2007. Texture measurement and friction estimation using laser data acquisition and neural networks. In: *Proceedings of the 9th WSEAS*

International Conference on Mathematical and Computational Methods in Science and Engineering, Trinidad and Tobago 2007.

Kennedy, C.K, Young, A.E., and Butler I. C., 1990. Measurements of Skidding Resistance and Surface Texture and the Use of Results in the United Kingdom, *Surface Characteristics of Roadways: International Research and Technologies, ASTM STP 1031,* American Society for Testing and Materials, Philadelphia, PA.

Kl¨uppel M. and Heinrich, G., 2000. Rubber friction on self-affine road tracks. *Rubber Chem. Technol*., 73(4):578 – 606.

Kokkalis, A. and Panagouli, O., 1998. Fractal Evaluation of Pavement Skid Resistance Variations. I: *Surface Wetting. Chaos, Solitons & Fractals*, 10.1016/S0960-0779(97)00138-0, 1875-1890.

Kuennen, T., 2003. Creating Friction Where Rubber Meets the Road, Better Roads.

Kulakowski, B. T., and Harwood, D. W., 1990. Effect of Water-Film Thickness on Tire-Pavement Friction, *Surface Characteristics of Roadways: International Research and Technologies, ASTM STP 1031,* American Society for Testing and Materials, Philadelphia, PA.

Lee, M.H, Chou, C.P., and Li, K.H., 2009. Automatic Measurement of Runway Grooving Construction for Pavement Skid Evaluation, *Automation in Construction 18*, 856-863.

Leu, M.C., Henry, J.J., 1978. Prediction of skid resistance as a function of speed from pavement texture measurements. *Transportation Research Record 666,* 7-13.

Li, L., Chan,P., Zollinger, D.G. and Lytton, R.L.,1990. Quantitative analysis of aggregate shape based on fractals", *ACI Materials, 90(4),* pp.357-365.

Luo, Wenting, Wang, Kelvin C. P., Li, Lin, 2014. Surface Drainage Evaluation for Rigid Pavements Using IMU and 1 mm 3D Texture Data. *Transportation Research Record: Journal of the Transportation Research Board,* Washington, D.C.

Mahone, D. C., McGhee, K. H., McGee, J. G. G., and Galloway, J. E., 1977. Texturing New Concrete Pavements, *Journal of the Transportation Research Board*, Washington D.C., Transportation Research Record, No. 652, 1-9.

Mansour, F. and Amoosoltani, E., 2005. Skid Resistance Assessment of Chip Seal Mixtures, *Proceedings, International Conference on Surface Friction,* Christchurch, New Zealand.

Martinez, J.E., 1977. Effect of pavement grooving on friction, braking, and vehicle control, *Transportation Research Record 633 1977 8–13*.

Mather, Paul, and Brandt Tso. 2009. Classification methods for remotely sensed data. *CRC press*.

McCarty J.L., 1971. Effects of runway grooving on aircraft tire spin-up behavior, *NASA TM X-2345*, 1971

McDaniel, R., and Coree B. J., 2003. Identification of Laboratory Techniques to Optimize Superpave HMA Surface Friction Characteristics, *No. SQDH 2003-6, 2003.*

McGhee, Kevin K., and Flintsch, Gerardo W., 2003. High-speed Texture Measurement of Pavements, *Virginia Transportation Research Council (VTRC) 03-R9.*

Mosher, L. G., 1969. Results from studies of highway grooving and texturing by several state highway departments: Pavement traction and grooving studies. *NASA SP-5073, National Aeronautics and Space Administration*, Washington, D.C., 465–504

Olek, J., Weiss, W. J., and Garcia-Villarreal, R., 2004. Relating Surface Texture of Rigid Pavement with Noise and Skid Resistance, Purdue University, West Lafayette, Indiana, *Report No. SQDH-2004-1* (Final Report HL 2004-1).

Ong, G.P.; Fwa, T.F. 2006a. Transverse pavement grooving against hydroplaning. I. Simulation model, *Journal of Transportation Engineering 132* 6 2006 .441–448.

Ong, G.P.; Fwa, T.F. 2006b. Transverse pavement grooving against hydroplaning. II. Design, *Journal of Transportation Engineering 132* 6 2006 .449–457.

Ong, G.P., and Fwa, T.F., 2006c. Analysis of Effectiveness of Longitudinal Grooving Against Hydroplaning, *Journal of the Transportation Research Board*, Washington D.C., Transportation Research Board, No 1949, 113-125.

Ong, Ghim Ping, Fwa, Tien F, 2008. Hydroplaning Risk Management for Grooved Pavements, *Seventh International Conference on Managing Pavement Assets*.

Owen, M.T., and Donbavand J., 2005.There's a Fraction Too Little Friction, *Proceedings, International Conference on Surface Friction*, Christchurch, New Zealand.

Patterson, J.W., 2012. Evaluation of Trapezoidal-Shaped Runway Grooves, *DOT/FAA/TC-TN12/7*.

Persson, B.N.J., 2001. Theory of rubber friction and contact mechanics. *J CHEMPHYS*, 115(8):3840 – 3861.

Persson, B.N.J., 2006. Contact mechanics for randomly rough surface, *Surface Science Reports*, 61(2006), pp7789-7823.

PIARC World Road Association, 1987. Report of the Committee on Surface Characteristics. In *Proceeding of XVIII World Road Congress*, Brussels, Belgium, 13–19.

Prowell, Brian D. and Hanson, Douglas I., 2005. Evaluation of Circular Texture Meter for Measuring Surface Texture of Pavements, Transportation Research Record: *Journal of the Transportation Research Board*, No 1929, Transportation Research Board of the National Academics, Washington, D. C., pp 88-96.

Rado, Z., 1994. Analysis of Texture Models, *PTI Report No. 9510*, Pennsylvania Transportation Institute (PTI), Penn State University, State College, Pennsylvania.

Rapol, J.L., and Wang, Q., 2010. Automatic Runway Groove Identification and Evaluation, *FAA Worldwide Airport Technology Transfer Conference*, April 20-22.

Reazei, Arash; Masad, Eyad; Chowdhury, Arif and Harris, Pat, 2009. Predicting Asphalt Mixture Skid Resistance by Aggregate Characteristics and Gradation, Transportation Research Record: *Journal of the Transportation Research Board*, No. 2014, Transportation Research Board of the National Academies, Washington, D. C., pp. 24-33.

Sandburg, U., 1998. Influence of Road Surface Texture on Traffic Characteristics Related to Environment, Economy, and Safety: A State-of-the-Art Study Regarding Measures and Measuring Methods, *VTI Report 53A-1997*, Swedish National Road Administration, Borlange, Sweden.

Sayers, Michael W., and Steven M. Karamihas. 1998. The little book of profiling. *Ann Arbor: Transportation Research Institute, University of Michigan*. http://www. umtri. umich. edu/erd/roughness/lit_book. pdf

Schmähling, J., F. A. Hamprecht, and D. M. P. Hoffmann. 1996. A three-dimensional measure of surface roughness based on mathematical morphology. *International Journal of Machine Tools and Manufacture* 46.14: 1764-1769.

Scofield, Larry. 2011. Development and implementation of the next generation concrete surface.

Scofield, Larry, 2012. Kansas I-70EB Surface Texture Test Section OBSI Evaluation, *IGGA*, 1/9/ 2012.

Smith, T. E., Chen, X., Song, W. and Hedfi, A., 2006. Investigation of Skid Resistance of Hot-Mix-Asphalt-Surfaced Pavements in Maryland State Highway Network System, *Proceedings CD from the 85th Annual Meeting of the Transportation Research Board*, Washington D.C.

Stout, K. J.; Sullivan, P.J.; Dong, W.P.; Mainsah, E., Luo, N.; Mathia, T.; and Zahyouani, H. 1993. The development of methods for the characterization of roughness in three dimensions, (commission of the European Communities) *(ISBN 0 70441 313 2)*.

Toan, D.V., 2004. Runway Friction Performance in NZ, *Beca Infrastructure Ltd*, Auckland, New Zealand.

Torbruegge, S and Wies, B., 2015. Characterization of pavement texture by means of height difference correlation and relation to wet skid resistance *Journal of Traffic and Transportation Engineering* (English Edition) Volume 2, Issue 2, Pages 59–67.

Transtec Group, 2012. ProVAL User's Guide (V3.4).

Ueckermann, A;Wang, D; Oeser,M, and Steinauer ,B., 2015. Calculation of skid resistance from texture measurements, *Journal of Traffic and Transportation Engineering* (English Edition) Volume 2, Issue 1, Pages 3–16.

Vallejo, Luis E.2001. Fractal Assessment of the Surface Texture of Pavements, *International Journal of Pavement Engineering*, 2:2, 149-156.

Wahl, Bernt, 2014. Calculating Fractal Dimension, Accessed on June 2014 at http://www.wahl.org/fe/HTML_version/link/FE4W/c4.htm.

Wang, K. C., Li, L., Luo, W.T., Larki.n AI, 2012. Potential Measurement of Pavement Surface Texture Based on Three-Dimensional Image Data, *TRB 91st Annual Meeting*, Washington DC.

Wang, K.; Li, Lin; Li, Q.; Nguyen, V.; Hayhoe, G.; Larkin, A. 2013a. Runway Groove Identification and Evaluation Using 1 mm 3D Image Data. *Airfield and Highway Pavement 2013*: pp. 730-741.

Wang, K., Li, L.; Li, J. 2014. Automated Joint Faulting Measurement Using 3D Pavement Texture Data at 1 mm Resolution. *T&DI Congress 2014*: pp. 498-510.

Wang, Qiang and Hayhoe, Gordon F. 2013b, Development and Implementation of a Beam-Bridging Filter for Use in Airport Groove Identification, *Transportation Research Record: Journal of the Transportation Research Board, No. 2369*, Transportation Research Board of the National Academies, Washington, D.C., 2013, pp. 95–103.

Westermann.S; Petry.F; and Noes, R., 2004. Experimental investigations into the predictive capabilities of current physical rubber friction theories, Kautschuk Gummi Kunststoffe, 57 (12), pp. 645–650.

Williams, Stacy G., 2008. Surface Friction Measurements of Fine-Graded Asphalt Mixtures, *MBTC 2066 Final Report*, Department of Civil Engineering, University of Arkansas, Fayetteville, Arkansas.

Wong, Shui-Yang., 1990. Effectiveness of Pavement Grooving in Accident Reduction, ITE Journal, 60 (7) 30-34.

Yager, T. J. 1969. Comparative braking performance of various aircraft on grooved and ungrooved pavements at the landing research runway, *NASA Wallops Station: Pavement grooving and traction studies. NASA SP-5073*, National Aeronautics and Space Administration, Washington, D.C., 35–66.

Yager, T. J., and Buhlmann, F., 1982. Macrotexture and Drainage Measurements on a Variety of Concrete and Asphalt Surfaces, Pavement Surface Characteristics and Materials, *American Society of Testing and Materials*, Philadelphia, ASTM STP 763, 16-30.

APPENDICES

APPENDIX A: SURFACE TEXTURE CHARACTERAZATION SOFTWARE

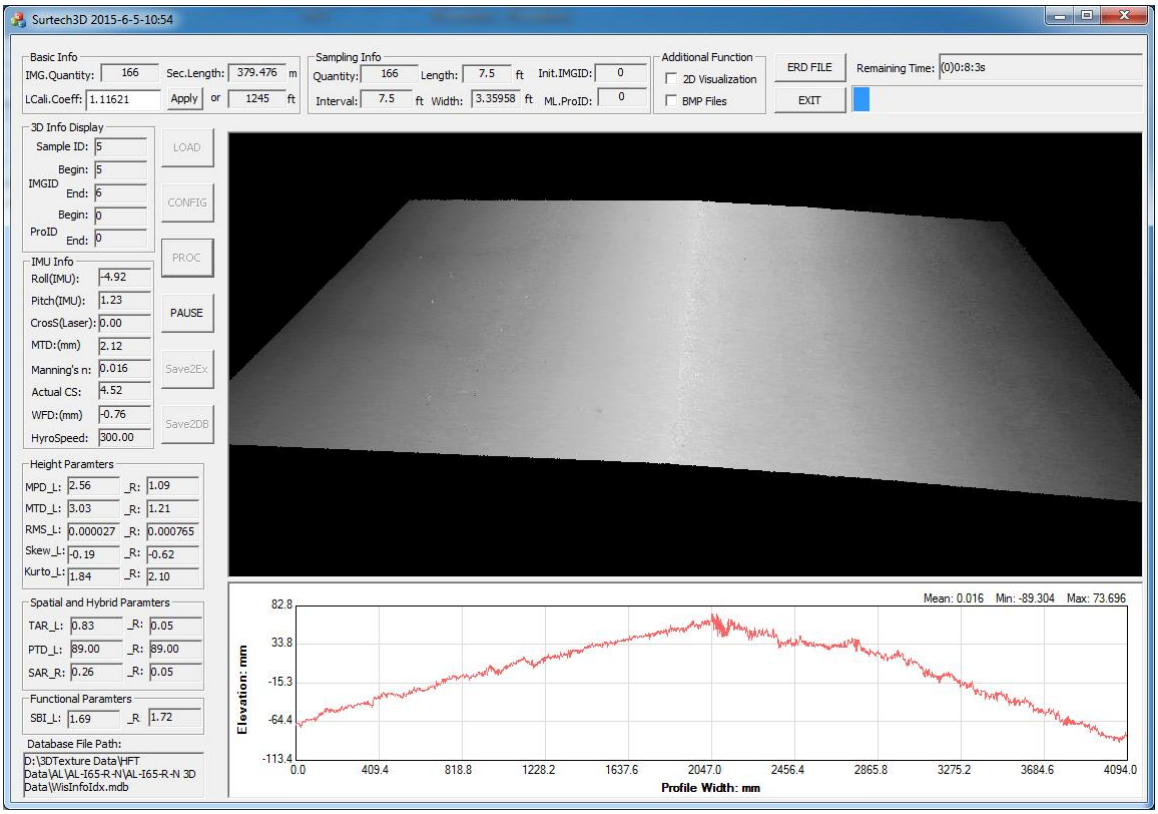

APPENDIX B: PAVEMENT FRICTION PREDICTIN SOFTWARE

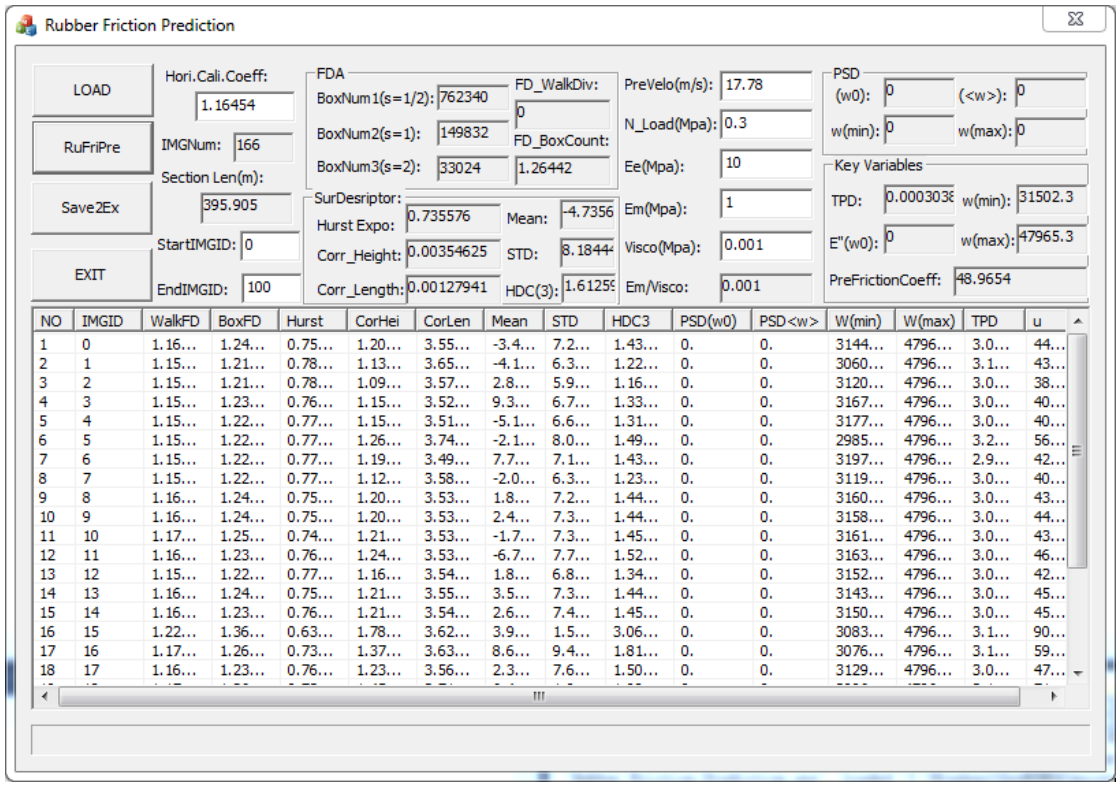

APPENDIX C: GROOVE MEAUREMENT AND EVALUATION SOFTWARE

VITA

LIN LI

Candidate for the Degree of

Doctor of Philosophy

Thesis: PAVEMENT SAFETY EVALUATION WITH 1MM 3D LASER TEXTURE DATA

Major Field: Civil (Transportation) Engineering

Biographical:

Education:

Completed the requirements for the Doctor of Philosophy in Civil Engineering at Oklahoma State University, Stillwater, Oklahoma in July, 2015.
Completed the requirements for the Master of Science in Logistics Engineering at University of Science and Technology Beijing, Beijing, China in 2009.
Completed the requirements for the Bachelor of Science in Transportation Engineering at China Agriculture University, Beijing, China in 2006.

Experience:

Jan 2010- Dec 2011: Research Assistant, Department of Civil Engineering, University of Arkansas
Jan 2012- Present: Research Assistant, Department of Civil and Environmental Engineering, Oklahoma State University